FINAL
IN-44-CR
30661
P-95

Heat Transfer Measurements for Stirling Machine Cylinders

A.A. Kornhauser, B.C. Kafka, D.L. Finkbeiner, and F.C. Cantelmi
Virginia Polytechnic Institute and State University
Blacksburg, VA 24061

August, 1994

Abstract

The primary purpose of this study was to measure the effects of inflow-produced heat turbulence on heat transfer in Stirling machine cylinders. A secondary purpose was to provide new experimental information on heat transfer in gas springs without inflow.

The apparatus for the experiment consisted of a varying-volume piston-cylinder space connected to a fixed volume space by an orifice. The orifice size could be varied to adjust the level of inflow-produced turbulence, or the orifice plate could be removed completely so as to merge the two spaces into a single gas spring space. Speed, cycle mean pressure, overall volume ratio, and varying volume space clearance ratio could also be adjusted. Volume, pressure in both spaces, and local heat flux at two locations were measured. The pressure and volume measurements were used to calculate area averaged heat flux, heat transfer hysteresis loss, and other heat transfer-related effects.

Experiments in the one space arrangement extended the range of previous gas spring tests to lower volume ratio and higher nondimensional speed. The tests corroborated previous results and showed that analytic models for heat transfer and loss based on volume ratio approaching 1 were valid for volume ratios ranging from 1 to 2, a range covering most gas springs in Stirling machines.

Data from experiments in the two space arrangement were first analyzed based on lumping the two spaces together and examining total loss and averaged heat transfer as a function of overall nondimensional parameters. Heat transfer and loss were found to be significantly increased by inflow-produced turbulence. These increases could be modeled by appropriate adjustment of empirical coefficients in an existing semi-analytic model.

An attempt was made to use an inverse, parameter optimization procedure to find the heat transfer in each of the two spaces. This procedure was successful in retrieving this information from simulated pressure-volume data with artificially generated noise, but it failed with the actual experimental data. This is evidence that the models used in the parameter optimization procedure (and to generate the simulated data) were not correct. Data from the surface heat flux sensors indicated that the primary shortcoming of these models was that they assumed turbulence levels to be constant over the cycle. Sensor data in the varying volume space showed a large increase in heat flux, probably due to turbulence, during the expansion stroke.

Table of Contents

1. Introduction

Heat transfer in cylinder spaces is important to the performance of many reciprocating energy-conversion machines. It affects the performance of gas compressors, internal combustion engines, and closed reciprocating machines such as Stirling engines and refrigerators. An understanding of in-cylinder heat transfer can improve machine design and speed development.

Heat transfer in cylinder spaces has been studied since the work of Nusselt in the 1920's. Until recently, models of in-cylinder heat transfer have ignored the effects of transient conditions; they have been extensions of steady-state models. Most of them have been of the same form as correlations for turbulent pipe flow: $Nu = aRe^b$.

Work done over the past fifteen years has shown that quasi-steady models are inadequate for predicting in-cylinder heat transfer. Heat transfer driven by an oscillating pressure differs from steady-state heat transfer not only in magnitude, but in phase: in-cylinder heat transfer can be out of phase with gas-wall temperature difference. Quasi-steady convective heat transfer modeling, in which heat transfer is proportional to temperature difference, cannot predict such behavior.

For studies with closed piston-cylinder gas springs, this heat transfer phase shift has been successfully predicted by use of a complex heat transfer coefficient. Since a complex number has both magnitude and phase, a complex coefficient can adequately describe the phase shift phenomenon. Its use may be thought of as analogous to the use of complex impedance in AC circuit theory.

The complex heat transfer coefficient in closed gas springs can be predicted fairly well by a theory which neglects turbulence. There is doubt as to whether this theory will be effective in actual engine cylinders, where high velocity inflow generates considerable turbulence.

1.1 Importance of In-Cylinder Heat Transfer for Stirling Machine Design

Experimentation and modeling indicate that in-cylinder heat transfer has an important effect on the performance of Stirling engines. The *PV* work from a Stirling machine is a result of heat transfer occurring at different times in the volume cycle: the magnitude and direction of heat transfer in each part of the cycle determine whether the machine will be an engine or a refrigerator and, to a large extent, how efficient an engine or refrigerator it will be.

The importance of in-cylinder heat transfer was clearly demonstrated in the Valved Hot Gas Engine (VHGE) project carried out at M.I.T. in the late 1970's. The VHGE was a closed, reciprocating, regenerative Brayton cycle engine, in many ways similar to a Stirling or Ericsson machine. Its performance was far below expectations. Extensive investigation showed that the difference between design and measured performance could be entirely attributed to the effects of in-cylinder heat transfer (Lee, 1978).

Experiments with gas springs show heat transfer-related losses as high as 14% of the stored

compression work (Kornhauser, 1989). These very high losses occurred at nondimensional speeds below those typically found in Stirling engine cylinders, but losses in the 2% range were found at typical Stirling cylinder conditions. A model developed by Gedeon (1989) predicts that these losses will be greatly increased by inflow and outflow.

Examination of Stirling engine performance models makes it clear that the effects of in-cylinder heat transfer are still very poorly understood. Geng (1991) compared the predictions of two of the most sophisticated codes, HFAST and GLIMPS, for the Component Test Power Converter (CTPC), a proposed Stirling engine. GLIMPS predicted a that 3.1% of the available work would be lost to cylinder heat transfer, while HFAST predicted 0.44%. The difference in this loss prediction was compensated for by differences in other loss predictions, and the net predicted power from the two models was almost the same. It was clear, however, that the basic nature of all the losses was poorly understood.

Better understanding of in-cylinder heat transfer is necessary for better prediction of Stirling engine performance and thus for better Stirling engine designs.

1.2 Models of In-Cylinder Heat Transfer

The first models of in-cylinder heat transfer were quasi-steady, based on extrapolation of steady state results. As research progressed, it became evident that the unsteady nature of in-cylinder heat transfer made these models invalid, and other models were developed. Recently, a model using a complex heat transfer coefficient, modeling both magnitude and phase of the heat transfer, has showed promise.

Quasi-Steady Models

Annand (1963) proposed that in-cylinder heat transfer in i.c. engines be modeled by an expression in the form

$$\mathrm{Nu} = a\mathrm{Re}^b. \tag{1.1}$$

Annand proposed that experimental data be fit using values
$\quad a = 0.76$
$\quad b = 0.64 \pm 0.10$
for two-stroke engines, and
$\quad a = 0.26$
$\quad b = 0.75 \pm 0.15$
for four-stroke-engines.

Annand based his Nusselt and Reynolds numbers on instantaneous gas properties, cylinder diameter, and mean piston speed.

Woschni (1967) proposed
$\quad a = 0.035$ and

$b= 0.8$,

but modified the speed used in the Reynolds number in an effort to reflect actual gas velocities. In the Reynolds number, he used

$v = 6.18 \times v_p$ during the scavenging period

$v = 2.28 \times v_p$ during the compression stroke, and

$v = 2.28 \times v_p$ + term for combustion-induced turbulence during the expansion stroke.

Most zero-dimensional i.c. engine codes use modifications of Woschni's model. Most Stirling machine codes which model in-cylinder heat transfer use an expression similar to equation (1.1).

Early Unsteady Models

Some i.c. engine and gas spring experimenters (Overbye et al (1961), Wendland (1986), Chong (1971), Annand and Pinfold (1980)) measured heat transfer out of phase with bulk gas-wall temperature difference. Since it was clear that an ordinary heat transfer coefficient could not model such behavior, various alternatives were proposed.

Overbye et al. (1961) developed an empirical model for in-cylinder heat transfer in i.c. engines that predicted heat flux based upon the change of in-cylinder pressure rather than on gas-wall temperature difference. The model predicted heat transfer for the compression stroke of the engine on which it was developed. Since it had little theoretical basis the model could not be more generally applied.

Wendland (1968) numerically solved a one-dimensional energy equation in order to model his experimental results. The model predicted gas spring heat transfer better than ordinary heat transfer coefficients did, but was impractical for insertion into more comprehensive engine models.

Breckenridge, Heuchling, and Moore (1971) presented a model for the temperature field in a gas subjected to sinusoidal pressure fluctuations. They used the solution to predict gas spring hysteresis loss, but did not extend it to prediction of heat transfer.

Keck (1981) developed models for the temperature field in a gas subjected to a sudden change in temperature far from the wall and for a gas subjected to a sudden change in pressure. Both these models were based on solutions to the one-dimensional energy equation. They were not tested experimentally, but were used to make heat transfer corrections to combustion bomb data. Keck did not present any way of applying his models to actual engine simulations.

Annand and Pinfold (1980) proposed that heat transfer phase shift be predicted by making the heat transfer coefficient a function of rate of change of temperature. They produced a semi-empirical expression

$$\text{Nu} = 0.3 \, \text{Re}^{0.7}(1+0.27\frac{D}{v\Delta T}\frac{dT}{dt}). \tag{1.2}$$

In this result v was the local instantaneous velocity and Re was based on v. Kornhauser (1989) showed that Annand and Pinfold's expression was essentially equivalent to one using a complex

Nusselt number.

Complex Nusselt Number Models

The complex Nusselt number extends the concept of Newton's law of cooling to conditions where the heat transfer is out of phase with the bulk temperature difference. In the expression $q''=h(T-T_w)dt$, the real heat transfer coefficient h is replace by a complex h_c.

The use of a complex Nusselt number was first proposed by Pfriem (1943). Pfriem solved the one-dimensional energy equation for a gas exposed to small sinusoidal pressure variations. He modeled turbulence by assuming that a thin layer near the wall would be stationary while the gas outside this layer would be so highly turbulent as to be isothermal. He used a the method of complex temperature to solve the resulting equations, and obtained a complex heat transfer coefficient by dividing the complex heat flux by the complex temperature difference. His result, in terms of the variables used in this work, was

$$\mathrm{Nu}_c = z \frac{1 - e^{-2\frac{\delta}{D}z} + z(\frac{1}{4} - \frac{\delta}{D})(1 + e^{-2\frac{\delta}{D}z})}{(1 - e^{-\frac{\delta}{D}z})^2 + z(\frac{1}{4} - \frac{\delta}{D})(1 - e^{-2\frac{\delta}{D}z})},$$

(1.3)

$$\text{where } z = (1+i)\sqrt{2\mathrm{Pe}_\omega}$$

Here Pe_ω is $\omega D_h^2/4\alpha$ and δ is the wall layer thickness. Pfriem did not propose any model for the prediction of δ.

Lee (1983) developed an expression for complex Nusselt number similar to Pfriem's. Instead of dividing the space into a fully turbulent and fully non-turbulent portions, he used a uniformly enhanced thermal diffusivity over the entire space. His result for Nu_c was

$$\mathrm{Nu}_c = \sqrt{2\mathrm{Pe}_\omega} \frac{(1+i)\tanh z}{1 - \tanh z/z}, \quad \text{where}$$

$$z = (1+i)\sqrt{\frac{\mathrm{Pe}_\omega}{8}}.$$

(1.4)

In addition to developing an expression for Nu_c, Lee used his solution to develop an expression for heat transfer hysteresis loss

$$\frac{\mathrm{Loss}}{P_0 V_0} = \frac{\pi}{2}\left(\frac{P_a}{P_0}\right)^2 \frac{\gamma - 1}{\gamma}\left(\frac{1}{y}\right)\frac{\cosh y \sinh y - \sin y \cos y}{\cosh^2 y - \sin^2 y},$$

(1.5)

$$\text{where } y = \sqrt{\frac{\mathrm{Pe}_\omega}{8}}.$$

Both Pfriem's and Lee's models predicted that at low nondimensional speeds (low Pe_ω) the real part of the complex Nusselt number would be much larger than the imaginary part, indicating heat transfer in phase with temperature difference. At higher speeds the real and imaginary parts were almost equal, indicating heat transfer leading temperature difference by 45°.

Kornhauser and Smith (1988,1993) compared Lee's model (with no turbulent enhancement of α) to experiment results from a piston-cylinder gas spring. They first compared the loss result to measured PV loss. At volume ratio 2.0 the model predicted loss fairly well over a range of gases, speeds, pressures, and geometries. At volume ratio 4.0 the model underpredicted; at 8.0 the underprediction was worse.

They compared their experiments to the Nu_c results by fitting Nu_c to their data using

$$\dot{q}'' = \frac{k}{D_h}\left[Nu_r(T-T_w) + \frac{Nu_i}{\omega}\frac{dT}{dt}\right], \tag{1.6}$$

where T was the instantaneous mixed mean gas temperature. They found that the model predicted results fairly well over a range of conditions at volume ratio 2.0, but underpredicted at volume ratios 4.0 and 8.0.

Kornhauser and Smith hypothesized that the models, developed for $r_v \rightarrow 1$, were valid over the range $1 < r_v < 2$. Their apparatus could not produce volume ratios significantly below 2.

Gedeon (1989) developed a model that was based, like Pfriem's and Lee's, on the one dimensional energy equation. The effect of turbulence was modeled by increasing the effective thermal diffusivity linearly from the molecular value at the wall to a much larger turbulent value at the space centerline. The turbulent value was selected based on pipe flow turbulence data. Gedeon's model showed much larger heat transfer magnitudes and much smaller heat transfer phase shifts than the non-turbulent version of Lee's model.

Kornhauser (1992) extended Pfriem's model by evaluating the boundary layer thickness δ based on cylinder wake heat transfer data. His result was

$$\frac{\delta}{D} = (16.5)Re_{in}^{-0.73}, \text{ or}$$
$$= \frac{1}{4}, \text{ whichever is smaller.} \tag{1.7}$$

Here Re_{in} was a Reynolds number based on cycle-mean cylinder conditions and maximum gas inlet velocity. Like Gedeon's model but to a somewhat smaller degree, the Pfriem-Kornhauser model predicted increased heat transfer magnitude and decreased heat transfer phase shift.

It should be noted that both the Gedeon and the Pfriem-Kornhauser models of in-cylinder heat transfer with inflow-produced turbulence assumed that turbulence levels were approximately constant over the cycle.

1.3 In-Cylinder Heat Transfer Measurement Techniques

Most Stirling engine experimental results have been in terms of overall engine performance. There have, however, been some measurements of in-cylinder phenomena. Some experiments have measured heat transfer, others have measured heat transfer hysteresis loss, and others have measured both. Since heat transfer models relate heat transfer to wall and gas temperatures, heat transfer experiments must measure both heat fluxes and gas temperatures to be useful.

Many experimenters have measured heat flux in cylinders using various surface heat flux gages (Borman and Nishiwaki, 1987). Most of these measurements have been in actual or simulated ic engine cylinders. The gages used have generally worked on the principal of measuring wall surface temperature and calculating transient heat flux by treating the wall as a semi-infinite solid. Both thermocouple and resistance-type gages have been used. This technique has two main disadvantages in producing data useful in Stirling engine analysis. One is that each heat flux gage measures heat transfer over only a very small area, so a great number of gages is needed to calculate overall cylinder space heat transfer. The other is that the method does not measure gas temperature. Some experimenters have made gas thermocouple and cold-wire measurements of temperatures in cylinder spaces, but these have been local measurements only. Even if a great number of sensors were installed, they would still be unable to measure temperatures within the piston's swept volume, which makes up most of the cylinder space.

Other experimenters have used pressure and volume measurements to calculate hysteresis loss, space-averaged heat flux, and mass-averaged gas temperature in gas springs. These measurements form the basis of many existing Stirling cylinder heat transfer models. The pressure-volume method of heat transfer measurement has the advantage of relating area-averaged heat transfer to mass-averaged temperature, precisely the relationship needed for input to Stirling codes. It also has the advantage of directly measuring hysteresis loss. So far, though, the method has been used only in closed gas springs. Attempts to extend it to cylinders with inflow and outflow were abandoned in the face of the difficulty of measuring mass and enthalpy flow in and out of the cylinder.

1.4 Experiment Concept

This experiment uses an alternate approach. As shown in Figure 2.2, the apparatus consists of two spaces connected by an orifice. One space is of fixed volume, while the volume of the other space varies. The spaces are instrumented so that pressure and volume of each space is known at all times throughout the cycle.

As done in previous experiments, pressure and volume data can be used to calculate total heat transfer in both space 1 and space 2. The heat transfer in each space cannot, however, be calculated from this data alone since the temperature and mass in each space is not known. This information can, however, be calculated from pressure and volume data using an inverse (parameter optimization) method if a basic form for the heat transfer and orifice flow models is selected. The coefficients in the heat transfer and flow models can be optimized to give a best fit to the measured pressure data. If a unique, excellent fit can be found it is safe to assume that the models used are adequate. If fits are poor or non-unique, an improved model must be found.

The experiment plan was to start by running experiments with no orifice plate in place, to confirm and extend previous results. Further data would then be collected with various orifices. The data would initially be analyzed by looking at the lumped effects on the two spaces, pending development of the full two space model.

The two space calculation technique would be tested on simulated data before application to actual data. Effects of noise and instrument error could be investigated using simulated data sets. When the technique was operating acceptably with simulated data, it would be applied to real data.

With two open spaces, the experiment can be used to investigate the effects on the complex Nusselt number of inflow-produced turbulence. A planned future application is to add regenerator-like packing material to the fixed volume space, so that the effects of inflow at temperatures different from the cylinder mean temperature can be studied.

2. Experiment Design

This section will give basic information on the experiment design: the design operating range, mechanical design, instrumentation, as-built operating range, and design operating procedure. Data analysis techniques will be discussed in sections 3 and 4.

2.1 Design Operating Range

In order for the experimental data to be applicable to Stirling machine design without extrapolation, the experiment was designed for operating conditions covering the range found in actual Stirling machines. No single apparatus could hope to duplicate the pressures, speeds, bores, strokes, etc. of all actual machines. A wide range of appropriate non-dimensional parameters, however, could be matched in a single apparatus.

In order to cover the non-dimensional parameters found in actual machines:

- Appropriate non-dimensional parameters were determined.
- The ranges of these parameters for actual machines were determined.
- A preliminary design was selected to cover the range as fully as practical.

Appropriate Non-Dimensional Parameters

Based on the work described in Section 1.2, the parameters listed in Table 2.1 were significant.

Table 2.1. Stirling Cylinder Nondimensional Parameters.

	Name	Definition
Pe_ω	Oscillation Peclet Number	$Re_\omega Pr = \omega D^2/4\alpha$ at cycle mean conditions
Re_{in}	Inlet Reynolds Number	Reynolds no. based on cylinder D_h, mean gas properties, and maximum inlet velocity
Re_{in}/Pe_ω	Ratio of parameters	A function of geometry only $\sim 3 \times$ Cylinder XS area / Inlet XS area
D/L_s	Bore-Stroke Ratio	Bore/Stroke
C/L_s	Clearance Ratio	Clearance/Stroke
r_v	Volume Ratio	V_{max}/V_{min}
γ	Specific Heat Ratio	c_p/c_v

Existing heat transfer models of Pfriem, Lee, Gedeon, and Kornhauser indicated that the most important of these parameters were Re_{in}, Pe_ω, and Re_{in}/Pe_ω. Only two of the three were independent; for design purposes Pe_ω and Re_{in}/Pe_ω were used.

Range of Parameters for Actual Machines

Several compilations of typical Stirling machine parameters were available in the literature. Martini (1983) presented design and test data from several Stirling machines. He presented very complete data for two engines: the General Motors GPU-3 and the Ford 4L23. Simon and Seume (1986) surveyed heat exchangers from a wide range of Stirling engines. The data they compiled was useful for determining cylinder inflow conditions. Gedeon (1989) listed non-dimensional parameters for expansion and compression spaces of many Stirling machines. The non-dimensional parameters he used can be converted to the ones used in this work. Sullivan (1989) compared simulations with tests for the RE-1000, GPU-3, and P-40 Stirling engines. He tabulated various design and performance data for these engines. NASA-Lewis personnel (Geng, 1991) provided data on current Stirling design trends.

Table 2.2 shows values of Pe_ω, Re_{in} and Re_{in}/Pe_ω for various Stirling machines. Most machines fall in the range $500 < Pe_\omega < 50,000$, $20,000 < Re_{in} < 2,000,000$, and $10 < Re_{in}/Pe_\omega < 100$. There are a few outliers to this range, and there would probably be additional outliers on the low end of Re_{in} and Pe_ω if more cryocoolers were included.

Bore-stroke ratio varies roughly from 2 to 7 for free piston machines and is usually around 1 for kinematic machines. A range of ratios from 1 to 7 would cover all cases.

Clearance ratio for free piston machines at maximum stroke typically varies from 0.1 to 0.2. There is, however, interest in performance at reduced stroke (down to $C/L_s \sim 0.5$) for fixed heat source applications. Clearance ratios for kinematic machines are considerably smaller, typically in the 0.01 to 0.05 range. A range from 0.05 to 0.5 would cover all cases.

Pressure ratio, rather than volume ratio, is typically the measured variable for Stirling engines. For experiment design, however, it is necessary to select a volume ratio. P_{max}/P_{min} for free piston machines typically varies from 1.1 to 1.3. This corresponds to $1.1 < r_v < 1.3$ for near-isothermal conditions and $1.06 < r_v < 1.17$ for near-adiabatic conditions with a monatomic gas. P_{max}/P_{min} for kinematic engines typically varied from 1.5 to 2.0. This corresponded to $1.5 < r_v < 2.0$ for near-isothermal conditions and $1.3 < r_v < 1.5$ for near-adiabatic conditions. A range of volume ratio from 1.1 to 2.0 would cover all cases.

Stirling machines are almost always run with monatomic gases ($\gamma = 1.67$) or diatomic gases ($\gamma = 1.4$). Most free piston space power applications use monatomic helium instead of diatomic hydrogen because of reduced leakage problems.

Preliminary Experiment Design

In addition to the parameter matching needed to model actual Stirling machines, the experiment design was determined by various practical limitations:

- The apparatus had to be adequately large for easy instrumentation.
- The operating speed had to be low enough that instrument frequency response was adequate.

Table 2.2. Pe_ω, Re_{in}, and Re_{in}/Pe_ω for various machines.

Machine	CComp/Exp Space	Pe_ω	Re_{in}	Re_{in}/Pe_ω	Symbol (Fig 2.1)	Notes
RE1000	C	6.84E3	1.42E5	20.7	A	1, 4
	E	2.07E3	1.17E5	56.4	a	
SPRE	C	3.08E4	3.74E5	12.1	B	1, 4
	E	5.51E3	1.49E5	27.1	b	
SDSE	C	3.12E3	6.76E4	21.7	C	1, 4
	E	8.32E2	2.05E4	24.6	c	
MOD1	C	5.25E4	7.63E5	14.5	D	2, 4
	E	6.96E3	5.51E5	79.1	d	
STC250PT	C	2.37E3	2.89E5	122.1	E	1, 4
	E	2.51E3	2.50E5	99.6	e	
GPU3	C	7.08E3	2.35E5	33.3	F	2, 4
	E	1.28E3	7.44E4	58.4	f	
ARMY	C	5.51E5	7.20E5	1.3	G	1, 4
	E	9.07E4	5.10E5	5.6	g	
STC300	C	2.41E3	1.18E5	49.1	H	3, 4
	E	1.46E4	3.29E5	22.5	h	
OXFORD	C	2.40E0	2.25E3	922.1		3, 4
	E	5.38E2	3.61E4	67.2	i	
FORD 4215	C	1.09E5	2.70E6	24.8	J	2, 5
	E	1.55E4	1.13E6	73.2	j	
GM 4L23	C	2.84E4	1.34E6	47.0	K	2, 5
	E	4.32E3	2.32E5	53.7	k	

Notes:
1. Free-Piston Engine   2. Kinematic Engine
3. Cryocooler   4. From Gedeon data
5. From Simon and Seume data

- Pressures had to be kept reasonably low to reduce sealing problems and piston loading.

In many cases it was not possible to cover the full range of a design parameter with a single apparatus. In these cases, the most important part of the range was selected. In cases where the parameters for kinematic and free piston engines were different, the free piston parameters were given preference.

The preliminary design goal was the following parameter ranges:

- $500 < Pe_\omega < 50,000$.

- $10 < Re_{in}/Pe_\omega < 100$ (for the varying volume space).

- $D/L_s = 2.0$. This was the high end of the free piston bore/stroke range. Lower values were difficult to obtain in a kinematic apparatus, as were variations in bore/stroke.

- $0.1 < C/L_s < 0.5$.

- $1.1 < r_v < 1.2$. Volume ratios up to 1.5 could be run over a reduced range of Pe_ω.

- $\gamma = 1.67$ (monatomic gases, helium and argon). Diatomic gases could be run as well, but no difference in heat transfer phenomena would be expected.
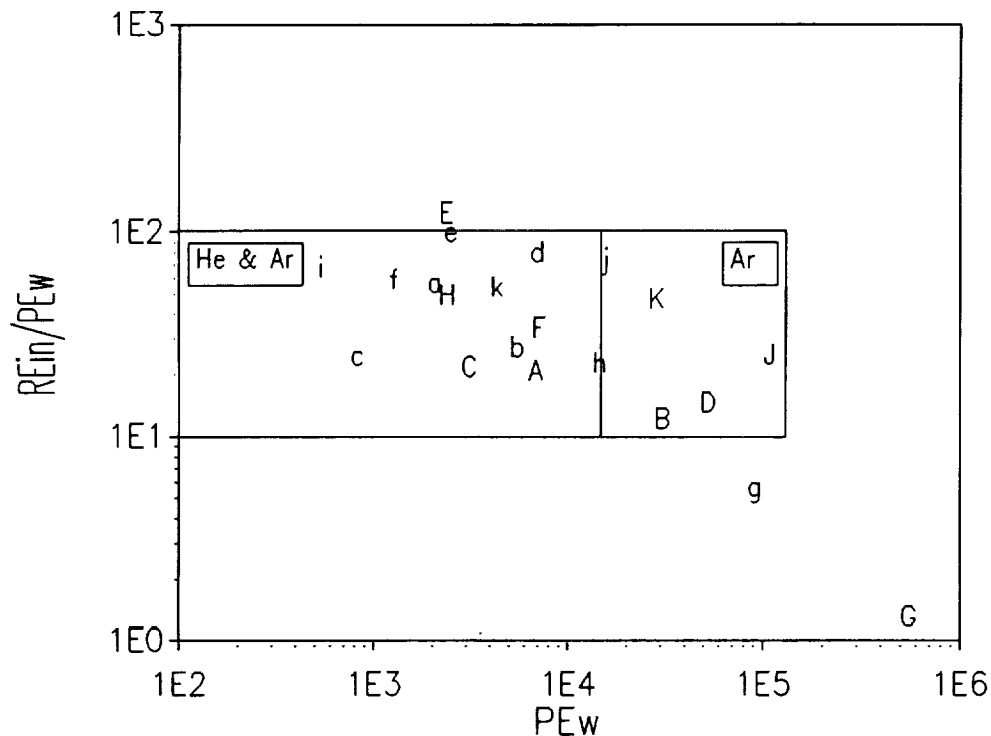

Figure 2.1. Experiment coverage design goal relative to range of Stirling machines. See Table 2.2 for symbols.

Figure 2.1 compares the planned range of Pe_ω and Re_{in}/Pe_ω for the experiment with that for the

Stirling machines listed in Table 2.2. Most of the range of these parameters is covered.

Because the validity of these non-dimensional groups had not yet been experimentally demonstrated for in-cylinder heat transfer with inflow and outflow, it was desirable to check their validity by varying some of the dimensional values within the parameters while keeping the non-dimensional whole constant.

Some of the reasoning that went into the parameter range selections shown above is made more clear in Sections 2.2 and 2.3.

2.2 Mechanical Design

The basic mechanical design concept is described, follow by more detailed description of the initial design of various components. Problems that occurred in during operation are then described, together with the solutions implemented.

Basic Design Decisions

A schematic of the apparatus is shown in Figure 2.2.

The design was based on the concept of a test section driven by an existing crank base. This design concept gave considerable cost and time savings in drive construction, but selection of the crank base dictated many of the design test section operating conditions.

A used Curtis two-stage air compressor was used as a crank base. The compressor low stage was 6-1/4" bore × 3-3/4" stroke, while the high stage was 3-3/8" bore × 3-3/4" stroke. The compressor was designed for a maximum operating speed of 680 rpm (11.3 Hz) and a maximum discharge pressure of 265 psia (1830 kPa).

The first parameter to be selected was bore/stroke ratio. Since a variable bore/stroke cannot be obtained with a mechanism of this type, a single value of 2.0 was chosen, at the low end of the free piston range. This sets test section bore at 19.05 cm (7.5 in) and stroke at 9.53 cm (3.75 in).

Because the test-section bore was much larger than the high-stage bore of the original compressor, test-section pressure would have been limited to 450 kPa (65 psia) if the crank base had supported the entire test section pressure. This would have result in an unacceptably low limit on Pe_ω.

In order to increase test section operating pressure a large bounce volume was included in the design to provide balancing pressure (equal to mean cycle pressure) on the rear face of the test section piston. For $P_{max}/P_{min} = 1.1$ this arrangement gave a maximum mean pressure of 6900 kPa (1000 psia), while for $P_{max}/P_{min} = 1.3$ it gave a maximum mean pressure of 2300 kPa (330 psia). These mean pressures allowed an adequate range of Pe_ω.

2-5

TIE ROD

ADJUSTABLE HEAD

PRESSURE AND HEAT
FLUX TRANSDUCERS

FIXED
VOLUME

VARYING VOLUME

PRESSURE AND HEAT
FLUX TRANSDUCERS

DIVIDING WALL
W ORIFICE(S)

GAS
THERMOCOUPLE

TEST SECTION PISTON

PISTON SEAL

BACKING
PRESSURE

LINE TO BACKING
PRESSURE TANK

POSITION
TRANSDUCER

BACKING PRESSURE SEAL

SELF-ALIGNING LINKAGE

TIE ROD

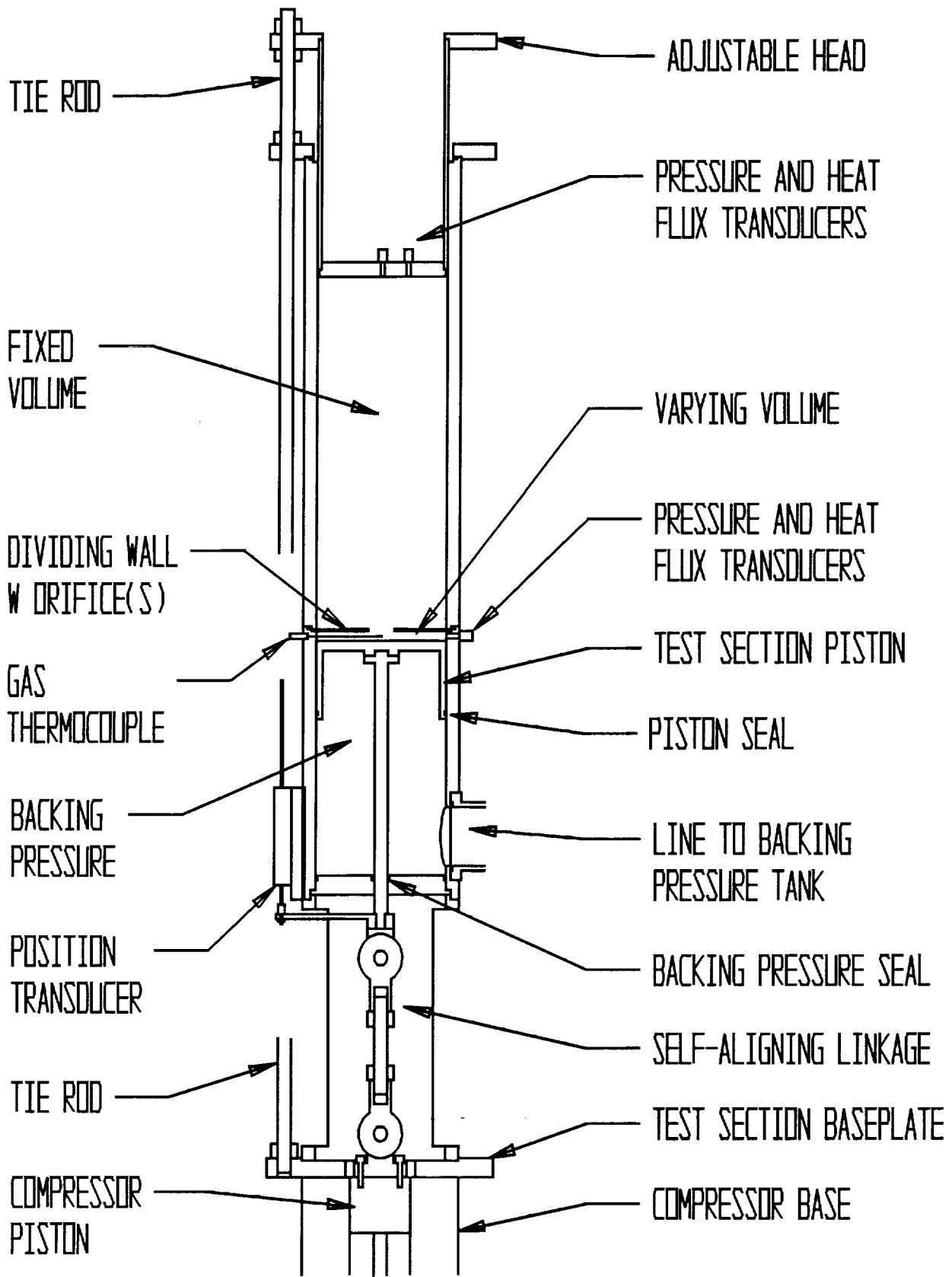TEST SECTION BASEPLATE

COMPRESSOR
PISTON

COMPRESSOR BASE

Figure 2.2. Schematic of experimental apparatus.

Since bearing life was not an important consideration for the test apparatus, the compressor was to be operated at up to 20 Hz (1200 rpm), 75% above its design operating speed. Provisions were made for reducing speed to as little as 0.5 Hz (30 rpm). The apparatus was mounted on a heavy cast iron engine test base to reduce vibration.

Volume ratios were variable from 1.1 to 1.2 over the full range of operating pressures. Volume ratios as high as 1.5 were possible, but only at lower pressures. Clearance ratios were adjustable from 0.1 to 0.5. Lower clearance ratios were not possible due to the necessity for installing instruments in the clearance volume.

Since Re_{in}/Pe_{ω} was basically a function of orifice diameter/cylinder diameter, a wide range was possible simply by making the orifices interchangeable.

Helium was the primary working fluid for the experiments. Argon was used for reaching higher Pe_{ω}. There was overlap between the helium and argon ranges.

As part of the design process, a preliminary experimental grid was specified. Additional data points could be added in response to experimental results.

Bore:	19.05 cm (7.50 in)
Stroke:	9.53 cm (3.75 in)
Volume ratio:	1.1 and 1.2
Clearance ratio:	0.1 and 0.2
Cylinder xs area / Inflow area:	3 and 30 for varying volume space, (corresponds to $Re_{in}/Pe_{\omega}=10$ and 100)
Speed:	0.5,1,2,5,10,20 Hz (30,60,120,300,600,1200 rpm)
Mean pressure:	1,2,5,10,17 bar (15,30,75,150,250 psia)
Working fluid:	He, Ar

Design Details: Piston Drive Mechanism

The apparatus was driven by a 4.1 kW (5.5 hp) shunt-wound direct current motor with a maximum nameplate speed of 30 Hz (1800 rpm). In order to set the apparatus speed, the motor armature voltage was varied through the use of a variable autotransformer and rectifier. The motor was connected to the compressor via a two-stage belt speed reducer, with sheaves that could be interchanged to alter the speed reduction. Based on an minimum motor speed of 15% maximum, this gave two design apparatus frequency ranges:

Range	Speed Reduction	Maximum Frequency	Minimum Frequency
High	1.4:1	21 Hz (1290 rpm)	3.2 Hz (193 rpm)
Low	9.0:1	3.3 Hz (200 rpm)	0.5 Hz (30 rpm)

The compressor base had a splash lubrication system which was not designed to operate below 5.8 Hz (350 rpm). To compensate for this, a force feed oil spray system was added.

The test section piston was driven off the high pressure compressor piston. In order to compensate for possible misalignment between the test section bore and the compressor piston, the drive was through a self-aligning linkage. The length of the linkage could be adjusted in steps of 0.53 cm (0.021 in) in order to set the mean piston position.

Design Details: Test Section

The test section was constructed from several sections of 19.1 cm (7.5 in) id honed steel tubing with a 1.91 cm (0.75 in) wall. The honed id was selected to provide a mating surface for the piston and head seals, while the heavy wall allowed easy mounting of transducers.

The first (lowest) section of tubing supported and aligned the rest of the test section. Sections of this tubing were cut out to allow adjustment of the self-aligning linkage and access for the volume measurement instrumentation.

The second section of tubing held the piston; the portion above the piston comprised the varying volume space. The portion below the piston formed a small part of the bounce volume, meant to reduce load on the compressor base. This space was closed of on the lower end by a plate through which the piston rod passed. A 50 cm (2 in) tube connected to the side wall linked it to the main bounce volume, a 60,000 cm^3 (3600 in^3) welded steel tank.

The orifice plate separating the fixed and variable volume spaces was clamped between the second and third sections of tubing. Two plates were made, with orifice diameters of 34.5 cm (1.36 in) and 10.46 cm (4.12 in). These gave orifice areas corresponding to 3.3% and 30% of the cylinder cross-sectional area, corresponding roughly to Re_{in}/Pe_ω = 100 and 10 for the varying volume space.

The third and fourth sections of tubing comprised the fixed volume space. For higher volume ratios (~ 1.2 and above) only the third section was used. For lower volume ratios (~ 1.1) both sections were used. The end of the fixed volume space was closed by a head which slid within the tubing so as to allow fine adjustment to the volume ratio.

The entire test section was held in compression by three threaded steel tie rods.

Test section static seals were all buna-n o-rings. There were two dynamic seals: the piston seal separating the test section working volume from the bounce volume, and the rod seal separating the bounce volume from atmosphere. These dynamic seals were Parker T-Seals™, essentially similar to an o-ring plus backing rings in a single unit. The dynamic seals were made from a lubricant impregnated nitrile material. The piston seal was located more than a stroke length from the piston face so that test section walls would not be frictionally heated.

The test section fill line was a small bore capillary, so that fill line volume would be negligible relative to test section volume. Clearance between the piston and the test section bore was kept small so that gas volume in the piston-wall-seal crevice would be small.
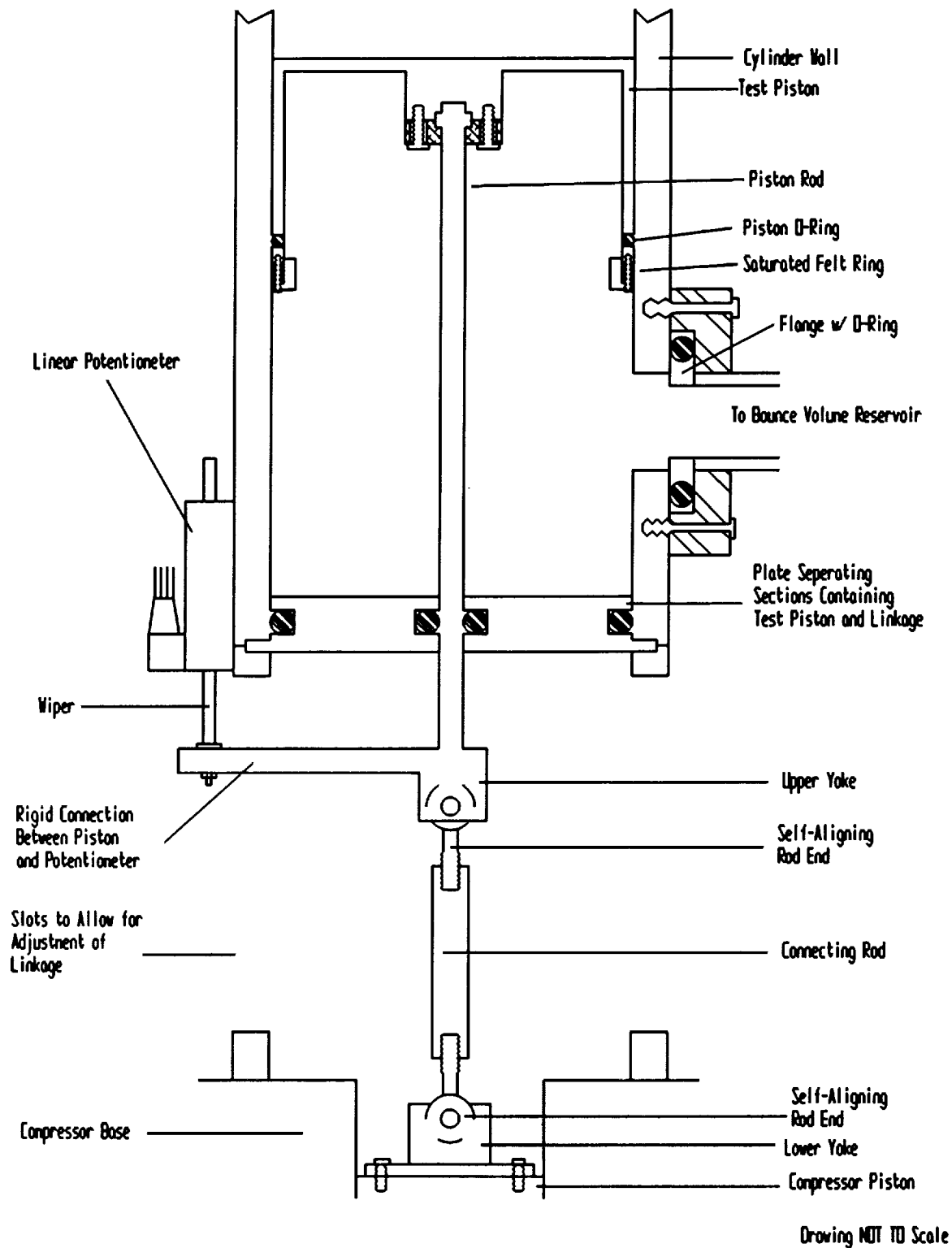
Figure 2.3 Test Section Piston and Linkage

2-9

Mechanical Design Problems and Modifications

During shakedown runs, the piston and piston rod seals (Parker T-seals™) showed evidence of excessive wear. The manufacturer had claimed the lubricant-impregnated nitrile material of the seals could be run without additional lubrication, but this was not the case. Provisions were made to lubricate both seals. A lubricating felt was installed in the piston wall below the piston seal. This felt was saturated with vacuum pump oil (selected for low vapor pressure) prior to reassembly. Since the piston rod outside of the rod seal was accessible, it was regularly lubricated by hand.

In order to reduce seal wear, maximum operating speed was reduced from 20 Hz (1200 rpm) to 10 Hz (60 rpm). This also helped reduce vibration, which was large at the higher speed.

The linkage between the piston and the compressor crankshaft had many bearing surfaces: crank bearings, wrist pin bearings, and self-aligning linkage bearings. This entire linkage was, in the original design, exposed to alternating tension and compression. The slack would thus alter the piston motion from that predicted by the ideal crank-connecting rod relationship. This was not felt to be a problems, since the linear potentiometer for measuring volume was rigidly connected to the piston and not affected by the slack. The slack turned out to be a problem, however, for two reasons:

- The total slack was considerable, causing stroke length to vary by +0.15/-0.23 cm (+0.06/-0.09 in) from the ideal stroke. The variation was caused by the differing pressure and inertial forces at different operating conditions. The slack added a small component, approximately a square wave, to the volume variation. This component contained high frequencies which caused difficulties with the data analysis.
- The high frequency parts of the square wave component caused ringing in the arm connecting piston rod to the volume potentiometer wiper. The arm (when reinforce, see Section 2.3) was adequately rigid for normal accelerations, but not for those introduced by the slack.

Although it might have been possible to numerically deal with the abnormal volume variation caused by the slack and to redesign the connecting arm to avoid ringing, it was more expedient to change the operating procedure so as to keep the entire linkage always in tension. Since this procedure increased the maximum load on the compressor base for a given cycle mean pressure, it the reduced maximum cycle mean pressure from 1725 kPa (250 psia) to 690 kPa (100 psia).

Some difficulty was encountered in starting the apparatus in cases with high mean pressure and low motor speed (low armature voltage). This problem was solved by starting the apparatus at high armature voltage and reducing the voltage after the apparatus began turning.

2.3 Instrumentation

The initial design for pressure, temperature, volume, and heat flux instrumentation is described below. The data acquisition system is then described. Finally, problems encountered during experimentation are discussed and resulting modifications are described.

Pressure

As in an actual Stirling engine, the pressure fluctuations in the apparatus were small relative to the mean cycle pressure. Since accuracy is more important in measuring the pressure fluctuations than in measuring the mean pressure, the pressure was measured using transducers in series. Each space (fixed volume and varying volume) was fitted with a fast response, low range differential pressure transducer. The back side of each transducer was connected to a small volume kept at near cycle mean pressure. This backing pressure was measured with a slower responding high range gage pressure transducer.

The differential pressure transducers were Kulite model XT-140 full bridge semiconductor strain gage transducers. The silicon pressure measuring diaphragm was flush mounted into the working volume and coated with a thin layer of RTV™ silicone rubber to eliminate false signals from thermal transients. The backing pressure was connected through tubing, but as this pressure was essentially constant ringing and delay were not a problem. The transducer diaphragms had a natural frequency of 150 kHz, so response time on the flush-mounted face was good.

The differential transducers were rated for ±345 kPa (±50 psid), with a maximum backing pressure of 1725 kPa (250 psig). The maximum pressure swing expected in the apparatus was ±260 kPa (±38 psi). With 10 volt excitation, the transducers had a nominal output of 0.3 mV/kPa (2 mV/psi). The signals were amplified (gain ~ 60) by two Measurements Systems model 2120A amplifiers with 15 kHz bandwidths. When processed through a 12 bit a/d converter with a ±5 V input range, the least significant bit was 0.14 kPa (0.02 psi). Calibration showed both transducers to be linear to within ±0.5% full scale.

The backing pressure transducer was a Teledyne model 176 wire strain gage pressure transducer with a 0-2070 kPa (0-300 psig) range. With 12 volt excitation, the transducer had a nominal output of 0.018 mV/kPa (0.13 mV/psi). The signal was amplified (gain ~ 130) by a Measurements Systems model 2120A amplifier with 15 kHz bandwidth. When processed through a 12 bit a/d converter with a ±5 V input range, the least significant bit was 1.0 kPa (0.15 psi). Calibration showed the transducer to be somewhat nonlinear, but was accurate to within ±0.3% full scale of a best-fit quadratic.

Volume

Volume was measured using a linear potentiometer, Novotechnic model TS100A502, to sense piston position. The potentiometer was mounted to the cylinder outside wall and sensed the movement of an arm rigidly connected to the piston, as shown in Figure 2.3. In this way any slack in crankshaft bearings, connecting rod bearings, or self-aligning linkage would not produce error in the volume signal. Head position and piston top center position were set using micrometer depth gages.

The linear potentiometer was excited with regulated ±5 V dc. The wiper had a stroke of 10 cm (3.94 in) and the signal was processed through a 12 bit a/d converter with a ±5 V range. The result was a least significant bit of 0.024 cm (0.0096 in), corresponding to 0.26% of the

piston stroke. When calibrated against a micrometer depth gage, the potentiometer output was found to be linear within $\pm 0.2\%$ of piston stroke.

Temperature

In order to check the temperature of the gas flowing between the spaces, a fast-response type E thermocouple (Paul Beckman model 320) was installed just below the orifice plate near the centerline of the orifice opening. The probe was 0.008 cm (0.003 in) diameter, with 0.002 cm (0.0007 in) diameter lead wires and a flat disk junction 0.003 cm (0.001 in) thick. It could thus be expected to have a short response time and cause minimal flow disturbance.

A thermistor cold junction compensator (Hades Corp. Series 143) was used to compensate for the fact that the cold junction was at ambient temperature. The signal was amplified (gain=1608) by a Measurements Systems model 2120A amplifier with a 15 kHz bandwidth. When processed through a 12 bit a/d converter with a ± 5 V input range, the least significant bit was $0.026°$ C ($0.014°$ F).

The flowing gas temperature measured by the gas thermocouple was somewhat inaccurate, mainly because of time lag, because of radiation effects, and because the temperature measured by the thermocouple was not necessarily representative of the average flowing gas temperature. The thermocouple temperature measurement was, however, intended mainly as a check on the basic pressure-volume measurement of temperature.

Local Heat Flux

Two surface heat flux sensors were installed in the apparatus: one in the side wall of the varying volume space (immediately below the orifice plate) and one in the end wall of the fixed volume space (in the head). Each of these sensors was a Medtherm model PTF-100-20404 platinum RTD heat flux sensor, consisting of a thin platinum film deposited on a Pyrex™ 7704 substrate.

Each sensor had a nominal resistance of 100 Ω and a sensitivity of 0.0023 $\Omega/\Omega°C$. Each was mounted in a Wheatstone bridge and excited at 0.266 V, resulting in a nominal bridge output of 0.61 mV/°C. The signal was amplified (gain=2100) by a Measurements Systems model 2120A amplifier with a 15 kHz bandwidth. When processed through a 12 bit a/d converter with a ± 5 V input range, the least significant bit was $0.004°$ C ($0.007°$ F). Since the RTD was used to calculate heat flux, only change in temperature and not absolute temperature was important. The Wheatstone bridge was therefore balanced at the beginning of each run.

In order to calculate surface heat flux, the surface temperature data was first Fourier decomposed into a series of sine and cosine components. The heat flux corresponding to each of these components was then calculated based on the solution for conduction in a semi-infinite wall with sinusoidal surface temperature variation (Carslaw and Jaeger, 1959). The calculation was based on the room temperature value of $(\rho c_p k)^{1/2}$ for Pyrex 7740, 15 17 $Ws^{1/2}/m^2K$ (0.0743 $Btu/Rft^2s^{1/2}$) (Skinner, 1961). The Fourier components of heat flux were then recombined to

produce the net heat flux.

The heat flux measured from these sensors represented only the local flux at the sensor, not the average flux over the volume. It was subject to inaccuracy, mainly because the material properties of the gage backing material did not match those of the surrounding metal walls. The heat flux gage temperature measurement was, however, intended mainly as a check on the basic pressure-volume measurement of heat flux.

Data Acquisition

Data was collected with an Analog Devices model RTI-860 analog/digital converter board installed in an IBM compatible computer with an Intel 80386-25 processor. The board had the capability of sampling 16 channels in a 12 bit ±5 V (used here) or ±10 V range. Up to four channels could be sampled simultaneously to within 50 picoseconds.

The board was controlled by a Basic language computer program. The program determined whether or not steady state had been reached and then sampled all of the transducer output channels for 3 cycles.

Steady state was determined from pressure and volume data. Based on an approximated piston frequency, calculated from a voltage signal proportional to the motor armature voltage, the board was programmed to scan the output of one of the pressure transducers for a period of time equivalent to twice the piston period (two revolutions). In this way a complete cycle was assured to have been sampled. After the output voltage was converted to pressure, the trapezoid rule was used to obtain the time averaged pressure over the full cycle. The time from the beginning of the cycle to the end of the cycle was used to compute the actual piston frequency. After all of the data had been manipulated, the process was repeated. When the time averaged pressure and piston frequency measured from two successive scans of data were within 1% of each other, steady state was assumed to have been reached.

Once steady state was reached, all of the transducers were scanned (using simultaneous sample and hold) to collect the final data set. Since all of the channels could not be scanned simultaneously (there were seven transducers and the maximum number of channels in a scanned group was four) four instrument channels were simultaneously sampled followed by the other three. Since the phase difference between the pressure and volume was important, the first group of sampled channels contained the pressure and volume instrumentation. The second group of channels contained the instruments which measured the gas temperature and the wall heat flux. The time used for this final scan was the time determined from the steady state calculations, as opposed to the time from the approximated piston frequency. The scan was long enough to ensure that three complete cycles of data were obtained, so that any cycle to cycle variation could be detected.

The data from the final scan was written into a file and further processed at a later time.

Instrumentation Problems and Modifications

During shakedown runs strange behavior of the volume transducer was evident. This behavior was traced to two sources (see Figure 2.3):

- The coupling between the potentiometer wiper and the arm from the upper yoke was insufficiently stiff, and was flexing at high piston speeds. The coupling was modified to correct this problems.
- The arm from the upper yoke to the wiper was being excited by some of the frequencies of the piston motion. This problem was corrected by stiffening the arm.

The differential transducers had some hysteresis at the zero crossing point. When mean cycle pressure was reduced in order to keep the drive train in tension (see Section 2.2), it became possible to adjust the transducer backing pressure so as to keep the transducers in a unidirectional mode. This was done on subsequent runs.

One of the surface heat flux sensors began to malfunction during the shakedown runs. As budgetary constraints did not allow purchase of a replacement, some runs were made with the transducer installed in the fixed volume space while others were made with it installed in the varying volume space.

Leakage from the apparatus was not significant during a single cycle, but over the entire startup period it was large enough to introduce some error into the temperature calculated from the pressure and volume signals. From the standpoint of the collected data, this appeared as a steady offset error. It was discovered part way through the experimental program.

To allow approximate compensation for the leakage, a thermocouple was installed near the center of the varying volume space. This type E thermocouple probe was only 0.159 cm (0.063 in) diameter, but since the junction was not exposed its time response was slow. The thermocouple was not, however, required to respond to the temperature variations over the cycle, only to the variations over the much longer startup period. The temperature measured from pressure-volume data was offset using the assumption that the cycle average temperatures from pressure-volume data and the center thermocouple would be equal.

2.4 Actual Operating Range

The operating range was smaller than that proposed in the original design due to the problems described in Sections 2.2 and 2.3 and because of time constraints. Table 2.3 compares the original design goals, the capability of the apparatus as built, and the range of experiments conducted to date. Figure 2.4 compares Pe_ω and Re_{in}/Pe_ω for various machines with the capabilities of the apparatus (based on the varying volume space) and the data collected to date.

Table 2.3 Actual Data Collection Range and Future Operating Range Capability

Parameter	Original Design Goal	Capability of Actual Apparatus	Range of Data Collection to Date	Remarks
Bore/Stroke Ratio	2.0	2.0	2.0	
Volume Ratio	1.1-1.5	1.1-1.5	1.1 One Space 1.2 Two Space	Volume ratios above 1.2 at reduced mean pressure
Clearance Ratio	0.1-0.5	0.1-0.5	0.11	
Cylinder Area/ Inflow Area	3-30	30-∞	30	Large inflow area gives low orifice ΔP, noisy results
Speed	0.2-20 Hz	0.5-10 Hz	0.5-10 Hz	
Mean Cycle Pressure	100-1720 kPa	100-690 kPa	100-1720 kPa	1720 kPa possible with reversing load on piston drive
Working Fluid	He, Ar	He, Ar, H_2, N_2	He	Use of gases other than He requires non-ideal equation of state for data analysis
Pe_ω (varying volume space)	10-125,000	20-28,000	20-3300	Capability based on no reversing load
Re_{in}/Pe_ω (varying volume space)	10-100	10-∞	109	Low Re_{in} gives low orifice ΔP, noisy results

2.5 Experiment Procedure

The procedure for a data run was as follows:

1) Atmospheric pressure was recorded from a barometer located in the test area.
2) The compressor flywheel was pinned in place at the geometric mean volume. This was done because static pressure at geometric mean volume is close to time-averaged pressure when operating.
3) While the backing pressure was equal to working volume pressure, the differential pressure transducers and heat flux sensor were balanced to correct for zero drift.
4) The bounce volume space, backing pressure space, and working spaces were filled to the
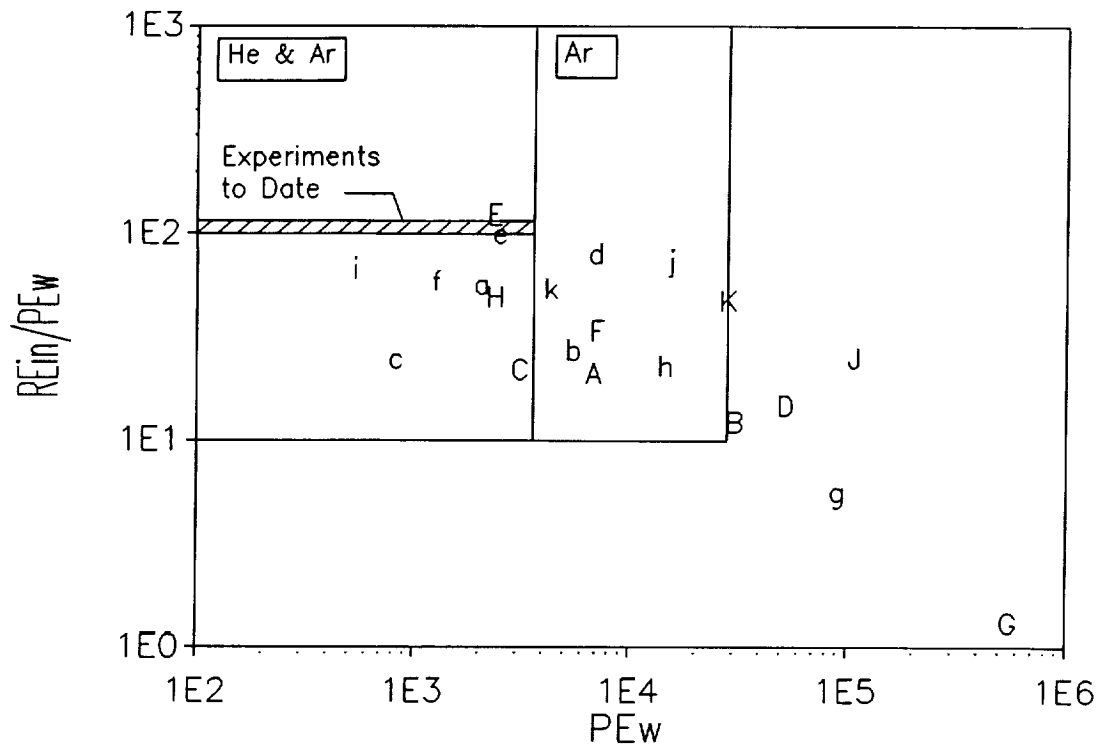
2-15

Figure 2.4 As-built experiment coverage relative to range of Stirling machines. See Table 2.2 for symbols.

proper pressures. In cases where reversing load on the piston drive mechanism was allowed, all three of these pressures were equal. In cases where the drive mechanism was kept in tension, the bounce volume pressure and backing pressure were larger than the working space pressure.

5)   The data acquisition program was started.

6)   The computer sampled the initial pressure, volume, and gas temperature in the apparatus. The mass in the cylinder was calculated from these initial values. For some data runs the mass was later corrected according to the measurements of the center gas thermocouple.

7)   The motor armature voltage was set to obtain (approximately) the desired test frequency.

8)   The pin at the compressor flywheel was then pulled and the motor was started.

10)   The computer took bursts of data to check for steady state. When the cycle-averaged pressure and piston frequency from one burst were within 1% that measured of the previous burst, steady state was assumed to have been reached.

11)   The computer took a set of data from the pressure transducers, the linear potentiometer, the gas thermocouple(s), and the heat flux sensor. The data collection time was 4 times the measured piston period to ensure that 3 complete cycles of data would be taken. Approximately 400 measurements were taken by each transducer during each cycle.

12)   After each experimental run was complete the apparatus was allowed to sit for 20 to 30 minutes to allow the dynamic seals to cool down.

If the apparatus was ever disassembled (to change orifice plates, to change the clearance ratio, to change the volume ratio, etc.), it was evacuated to near full vacuum after reassembly and leak tested.

3. Single Space and Lumped Two-Space Data Analysis

When the orifice plate was not in place, the data could be analyzed using the single space data analysis techniques used by previous experimenters. With the orifice plate in place, some of these techniques, slightly altered, could still be applied to the two spaces lumped together.

3.1 Single Space Data Analysis

The most important results from the single space experiments were pressure magnitude, pressure phase shift, non-dimensional cyclic lost work and complex Nusselt number. In order to calculate Nu_c, mixed mean gas temperature and surface averaged heat flux had to be calculated. Local heat flux at the surface heat flux sensor was also calculated.

Nondimensional Pressure Magnitude

The nondimensional pressure magnitude, P^*, gives an indication of the magnitude of the measured pressure swing in comparison to the corresponding adiabatic and isothermal pressure swings. This quantity was first proposed by Chafe (1988) and then used by Kornhauser (1989). P^* is given by

$$P^* = \frac{P_a - P_{a,is}}{P_{a,ad} - P_{a,is}}, \tag{3.1}$$

where P_a is the amplitude of the first harmonic of the measured pressure variation, $P_{a,is}$ is the amplitude of the first harmonic of the isothermal pressure variation corresponding to the measured volume variation, and $P_{a,ad}$ is the amplitude of the first harmonic of the adiabatic pressure variation corresponding to the measured volume variation.

When P^* equals 1 the processes within the working volume are essentially adiabatic, while when P^* equals 0 the processes are essentially isothermal.

Pressure Phase Lead

The pressure phase lead, Φ_p, was defined as the amount of phase shift between the measured pressure and the corresponding adiabatic or isothermal pressure:

$$\Phi_P = \Phi_{measured} - \Phi_{ad} = \Phi_{measured} - \Phi_{is} . \tag{3.2}$$

Here $\Phi_{measured}$ is the phase of the first harmonic of the measured pressure, Φ_{is} is the phase of the first harmonic of the isothermal pressure fluctuation corresponding to the measure volume, and Φ_{ad} is the phase of the first harmonic of the adiabatic pressure fluctuation corresponding to the measured volume. $\Phi_{is} = \Phi_{ad}$.

Non-Dimensional Lost Work

The work lost due to heat transfer hysteresis is a good global measure of the accuracy of a heat transfer prediction method. It can also be used as a correction to Stirling machine performance models that do not include modeling of in-cylinder heat transfer.

Kornhauser and Smith (1993) defined a non-dimensional cyclic lost work based on Lee's (1983) analysis of in-cylinder heat transfer:

$$Loss_{nd} = \frac{-\oint PdV}{P_o V_o (\frac{P_a}{P_o})^2 \frac{\gamma-1}{\gamma}} \tag{3.3}$$

where:

P_o = the mean pressure over the cycle,
V_o = the mean volume, and
P_a/P_o = a measure of the pressure variation, calculated as

$$\frac{P_a}{P_o} = \frac{P_{max} - P_{min}}{P_{max} + P_{min}} \tag{3.4}$$

The trapezoidal rule was used to evaluate the integral in equation 3.1.

Mixed Mean Temperature as a Function of Time

The mixed mean gas temperature was calculated on the assumption that the working fluid was an ideal gas with constant specific heat. This was a good assumption for helium at the conditions used, but would give some error for argon, nitrogen, or hydrogen (Kornhauser, 1989).

Mixed mean temperature was thus

$$T = \frac{PV}{mR} = T_{ref} \left(\frac{PV}{P_{ref} V_{ref}} \right). \tag{3.5}$$

In the work done here, the reference conditions were those measured immediately before the apparatus was started. The second equality of equation 3.5 was valid so long as the mass was constant over the entire run.

There was some small leakage during the experiment startup, so the above assumption was not strictly true. On some of the experimental runs the readings of a gas thermocouple installed in the center of the fixed volume space (see Section 2.3) were used to correct for this leakage; on runs prior to the installation of this thermocouple the one at the orifice centerline was used. The correction was made on the assumption that the cyclic mean temperature measured by the thermocouple was equal to cyclic and mass mixed mean temperature. Thus

$$\oint T_{tc} dt = \oint \frac{PV}{mR} dt, \qquad (3.6)$$

and the mass in the cylinder (assumed constant over one cycle) was

$$m = \frac{\oint PV dt}{R \oint T_{tc} dt}. \qquad (3.7)$$

This mass could be substituted into equation 3.5 to get a corrected mixed mean temperature:

$$T = \frac{PV \oint T_{tc} dt}{\oint PV dt}. \qquad (3.8)$$

The integrals in equation 3.8 were evaluated using the trapezoidal rule.

Surface-Average Heat Flux as a Function of Time

Surface average heat flux was calculated from pressure and volume data, once again using the assumption that the working fluid was an ideal gas with constant specific heat.

For a closed thermodynamic system, the first law states (with heat and work defined as positive out of the system):

$$\delta Q = -dU - PdV \qquad (3.9)$$

For an ideal gas with constant specific heat, the internal energy is given by:

$$U - U_{ref} = mc_v(T - T_{ref}) \qquad (3.10)$$

The ideal gas law can be used to replace the temperature in equation 3.10 with pressure and volume. After differentiating the internal energy, and using the relationship $c_v/R = 1/(\gamma-1)$, the following expression for δQ is obtained:

$$\delta Q = -(\frac{\gamma}{\gamma-1})PdV - (\frac{1}{\gamma-1})VdP \qquad (3.11)$$

Differentiating with time and dividing by total surface gives:

$$\dot{q}'' = \frac{1}{A} \frac{\delta Q}{dt} = -\frac{V}{A}(\frac{1}{\gamma-1})(\frac{dP}{dt}) - \frac{P}{A}(\frac{\gamma}{\gamma-1})(\frac{dV}{dt}). \qquad (3.12)$$

The time derivatives were calculated using Fourier transforms. The pressure and volume signals

3-3

were Fourier decomposed, the time derivative of each component was taken, high frequency components were discarded to reduce noise, and the components were recombined using Lanczos smoothing (Hamming, 1983). Twenty Fourier coefficients were retained in calculating the data presented here.

Local Heat Flux as a Function of Time

Local heat flux at a single location was measured using the surface heat flux sensor.

The sensor substrate was modeled as a 1-D, semi-infinite solid, with thermal properties independent of temperature. For a sinusoidal surface temperature variation

$$T = T_o + T_c\cos(\omega t) + T_s\sin(\omega t),$$ (3.13)

the heat flux, after initial transient disturbances have died away, was given by

$$\dot{q}'' = \beta\sqrt{\frac{\omega}{2}}[(T_s + T_c)\cos(\omega t) + (T_s - T_c)\sin(\omega t)]$$ (3.14)

(Carslaw and Jaeger, 1959). Here $\beta = (\rho c_p k)^{1/2}$ is a measure of the thermal properties of the wall.

The surface temperature measured by the heat flux sensor was Fourier decomposed into sine and cosine components, the heat flux due to each component was calculated using equation 3.14, high frequency components were discarded to reduce noise, and the components were recombined using Lanczos smoothing (Hamming, 1983). Twenty Fourier coefficients were retained in calculating the data presented here.

Complex Nusselt Number

The complex Nusselt number model for in-cylinder heat transfer, described in Section 1.2, gives gas-wall heat flux for a constant temperature wall as

$$\dot{q}'' = \frac{k}{D_h}[Nu_r(T - T_w) + \frac{Nu_i}{\omega}\frac{dT}{dt}].$$ (3.15)

where:
T = the mass mean temperature
T_w = wall temperature,
k = thermal conductivity of the gas,
D_h = hydraulic diameter,
Nu_r = the real portion of the complex Nusselt number, and
Nu_i = the imaginary portion of the complex Nusselt number.

Equation 3.15 has two coefficients: Nu_r and Nu_i. Thus at least two $q"$ - ΔT - $d\Delta T/dt$ were needed to calculate the complex Nusselt number. The cyclic mean complex Nusselt number was calculated to give an optimum least squares fit to all $q"$ - ΔT - $d\Delta T/dt$ data points. This fit gave:

$$Nu_r = (\frac{D_h}{k}) \frac{\sum (\dot{q}"_n \Delta T_n)\sum \Delta T_n^2 - \sum (\dot{q}"_n \Delta T'_n)\sum \Delta T_n \Delta T'_n}{\sum \Delta T_n^2 \sum \Delta T'_n{}^2 - (\sum \Delta T_n \Delta T'_n)^2}$$ (3.16)

and

$$Nu_i = (\frac{\omega D_h}{k}) \frac{\sum \dot{q}"_n \Delta T'_n \sum \Delta T_n^2 - \sum \dot{q}"_n \Delta T_n \sum \Delta T_n \Delta T'_n}{\sum \Delta T_n^2 \sum \Delta T'_n{}^2 - (\sum \Delta T_n \Delta T'_n)^2}.$$ (3.17)

In equations 3.16 and 3.17

$$\sum = \sum_{n=0}^{360} \quad \text{and} \quad \Delta T' = \frac{d(T-T_w)}{dt}.$$ (3.18)

3.2 Lumped Two Space Data Analysis

Non-Dimensional Lost Work

This work was directed toward studying in-cylinder heat transfer and related phenomena, so the lost work of interest was that due to heat transfer "hysteresis." In the two space experiment, the lost work represented by $\oint PdV$ was a combination of loss due to heat transfer and viscous loss due to flow through the orifice. In order to separately calculate the heat transfer loss, it was necessary to know the orifice flow loss. This could not be exactly calculated without a full two space data analysis, but it could be approximated for the purposes of the lumped two space analysis.

The total non-dimensional loss was the same as that for the single space case, but since $dV=0$ for the fixed volume space, the PdV integral was calculated for the varying volume space only:

$$Loss_{tot,nd} = \frac{-\oint P_v dV_v}{P_o V_o (\frac{P_a}{P_o})^2 \frac{\gamma-1}{\gamma}}$$ (3.19)

Here the subscript v refers to the varying volume space.

The pressure drop loss was calculated from an entropy balance across the orifice. In the calculation the density in the two spaces was assumed to be equal.

For an ideal gas with constant specific heat, the specific entropy change for flow through an adiabatic orifice ($T_{out}=T_{in}$) is given by

$$s_{out} - s_{in} = R \ln \frac{P_{in}}{P_{out}}. \tag{3.20}$$

The entropy generated each cycle was

$$S_{gen} = \int_{f-v} R \ln \frac{P_f}{P_v} dm_v \tag{3.21}$$

for flow from the fixed volume space to the varying volume space, and

$$S_{gen} = \int_{v-f} R \ln \frac{P_v}{P_f} dm_f \tag{3.22}$$

for flow from the fixed volume space to the varying volume space.

By combining equations 3.21 and 3.22 using the relationship $dm_v=-dm_f$

$$S_{gen} = \oint R \ln \frac{P_f}{P_v} dm_v . \tag{3.23}$$

The loss due to the flow was then

$$\text{Loss}_{\Delta P} = T_w S_{gen} = RT_w \oint \ln \frac{P_f}{P_v} dm_v. \tag{3.24}$$

By assuming that the density was constant in space, m_f was approximated as

$$m_v = m_{tot}(\frac{V_v}{V_{tot}}) = \frac{P_{ref}V_{ref}}{RT_{ref}}[\frac{V_v}{V_v + V_f}], \tag{3.25}$$

and dm_f as

$$dm_v = \frac{P_{ref}V_{ref}}{RT_{ref}} \frac{V_f}{(V_v + V_f)^2} dV_v. \tag{3.26}$$

By substituting equation 3.26 into 3.24 and combining terms with $T_w=T_0$ (wall temperature varies little from startup) the loss due to the pressure drop is approximated as

$$\text{Loss}_{\Delta P} \approx V_f V_{ref} P_{ref} \oint \frac{\ln(P_f/P_v)}{(V_f + V_v)^2} dV_v , \tag{3.27}$$

where the reference conditions are the startup conditions.

Non-dimensional heat transfer loss is then calculated by combining equations 3.19 and 3.27 to get

$$
\text{Loss}_{\Delta T, nd} \approx \frac{-\oint P_v dV_v - V_f P_o V_o \oint \dfrac{\ln(P_f / P_v)}{(V_v + V_f)^2} dV_v}{P_o V_o \left(\dfrac{P_a}{P_o}\right)^2 \dfrac{\gamma - 1}{\gamma}}
\tag{3.28}
$$

where:

v : conditions in the varying volume space,
f : conditions in the fixed volume space, and
o : initial conditions.

Mixed Mean Temperature as a Function of Time

In order to treat the two spaces as a lumped thermal mass, the overall mixed mean temperature had to be calculated. The mixed mean temperature was defined as

$$
T_m = \frac{T_v m_v + T_f m_f}{m_v + m_f}.
\tag{3.29}
$$

With

$$
T_v = \frac{P_v V_v}{m_v R} \quad \text{and} \quad T_f = \frac{P_f V_f}{m_f R},
\tag{3.30}
$$

the total mixed mean temperature became

$$
T_m = \frac{P_v V_v + P_f V_f}{mR}.
\tag{3.31}
$$

where:

m : total mass in the test apparatus measured from initial conditions,
v : conditions within the varying volume space, and
f : conditions within the fixed volume space.

This mixed mean temperature could be corrected for leakage during the startup period as described in Section 3.1.

Space Averaged Heat Flux

The heat flux measured from the pressure and volume data followed essentially the same calculation technique as was used for the single space case, but a few changes were necessary. Once again, the first law of thermodynamics was used to measure the heat flux, with

$$\delta Q = -dU - (P_v dV_v + P_f dV_f), \quad (3.32)$$

$$U - U_{ref} = mc_v(T - T_{ref}). \quad (3.33)$$

Here the temperature is the lumped two space mixed mean temperature given in equation 3.31. Substituting this temperature into equation 3.33 and differentiating gives

$$dU = \frac{c_v}{R} P_v dV_v + \frac{c_v}{R} V_v dP_v + \frac{c_v}{R} V_f dP_f, \quad (3.34)$$

where $dV_f = 0$. Combining this result with equation 3.32, using $c_v/R = 1/(\gamma-1)$, and differentiating over time then gives the lumped two space average heat flux as

$$\dot{q}'' = \frac{1}{A}\frac{\delta Q}{dt} = -(\frac{\gamma}{\gamma-1})\frac{P_v}{A}\frac{dV_v}{dt} - (\frac{1}{\gamma-1})[\frac{V_v}{A}\frac{dP_v}{dt} + \frac{V_f}{A}\frac{dP_f}{dt}]. \quad (3.35)$$

4. Two-Space Data Analysis

4.1 Methodology

Goal

The goal of this analysis was to determine the heat transfer in each of the two connected spaces from pressure and volume measurements. Two methods were investigated; both were based on proposing a form for the heat transfer model and then evaluating the coefficients within that form that gave a pressure-volume-time relationship that best matched the experimental data. The first method, the "no model" approach, attempted to calculate the heat transfer without the use of any model for flow through the orifice. The second method, the "unsteady orifice model" approach, added a model of orifice flow, also with undetermined coefficients, to the heat transfer model.

The models are described briefly below and in more detail later. The development and use of a simulated data set for testing the models is also described.

Method 1: No Model of the Fluid Mechanics

This method was based on writing the energy equation for each of the two spaces with the heat transfer term expressed using a complex Nusselt number (equation 1.6). The complex heat transfer coefficients in each space, the mass in each space, and the mass flow rate were all unknowns. It was assumed that the heat transfer coefficients were constant over a short range of data points and the energy equations for this range of points were written in finite difference form. Enough equations could thus be written to solve, in theory, for all the unknowns. This procedure could be repeated for each short range of data points.

While a solution appeared to be possible, no technique for finding it could be developed. There was also some doubt as to whether a unique solution existed without any restrictions on the fluid mechanics. This method was therefore abandoned in favor of the second method.

The no model method will be described in more detail in Section 4.2.

Method 2: Unsteady Orifice Flow Model

The second method added an additional equation by formulating relationship between the flow through the orifice and the pressure difference between the two spaces. This relationship added another two coefficients to the list of unknowns, but removed the masses from that list.

Besides this change, another important difference between this approach and the first was that all coefficients, both complex heat transfer and orifice flow, were assumed to be constant over the cycle. This assumption was not, perhaps, necessary. It may have been possible, with the

addition of an orifice equation, to solve over a short range of data points as planned for the no model method. The assumption was used in an effort to make the problem simpler and get results more quickly. If the assumption were incorrect, this should be evident: the method would not be able to match the pressure-volume-time data accurately.

Since the method assumed that coefficients were constant over the cycle, the coefficients were found by minimizing the least-squares error between a full cycle simulation and the measured data.

4.2 No Fluid Mechanics Model Approach

This section describes the development of the thermodynamic energy equation, the complex Nu expression for heat transfer, their combination into an overall energy balance, the finite difference implementation, and solution attempts.

Even though this method was eventually abandoned, the energy equations developed in this section were later used in the unsteady orifice model approach and are thus of interest.

Governing Equations: Thermodynamic Expression for Heat Transfer

In order to write overall energy balances for each space, expressions had to be developed for heat transfer in terms of pressure, volume, mass, and mass flow. The derivation of these expressions was based on several assumptions:
- the working fluid is an ideal gas with constant c_p and c_v,
- the gas flowing through the orifice has the properties of the upstream space,
- the cylinder wall remains at constant temperature, and
- there are no pressure gradients within either of the spaces, only between them.

The expression for the varying volume space will be developed first; the expression for the fixed volume space will be very similar.

The first law of thermodynamics for a system with inflow/outflow is
$$\delta Q_v = -dU_v - \delta W_v + h_t \, dm_v. \tag{4.1}$$

Here the heat transfer Q and work W are both considered positive leaving the space. The subscript v refers to the varying space, while the subscript t refers to the flowing fluid and thus to the upstream space.

U_v can be written as the product of an intrinsic property and mass, and the derivative of the product can be expanded. W can be written as pressure-volume work.

$$dU_v = d(u_v m_v) = u_v dm_v + m_v du_v \tag{4.2}$$

$$\delta W_v = P_v dV_v \tag{4.3}$$

These expressions can then be substituted into (4.1) to give

$$\delta Q_v = -u_v dm_v - m_v du_v - P_v dV_v + h_t dm_v. \tag{4.4}$$

Specific energy and enthalpy can be written in terms of specific heat and reference conditions:

$$u_v = u_{ref} + c_v(T_v - T_{ref}) \tag{4.5}$$

$$h_t = u_{ref} + c_v(T_t - T_{ref}) + P_t v_t \tag{4.6}$$

and the results can be substituted into (4.4):

$$\delta Q_v = -[(u_{ref} dm_v + c_v T_v dm_v - c_v T_{ref} dm_v) + (m_v du_{ref} + m_v c_v dT_v - m_v c_v dT_{ref})] - P_v dV_v \tag{4.7}$$

$$+ (u_{ref} dm_v + c_v T_t dm_v - c_v T_{ref} dm_v + P_t v_t dm_v)$$

The reference terms all cancel, giving:

$$\delta Q_v = -[c_v T_v dm_v + m_v c_v dT_v] - P_v dV_v + [c_v T_t dm_v + P_t v_t dm_v] \tag{4.8}$$

Temperature is now the only remaining variable that can be removed analytically. Using $R = c_p - c_v$, (4.8) becomes

$$\delta Q_v = -[c_v T_v dm_v + m_v c_v dT_v] - P_v dV_v + [c_p T_t dm_v] \tag{4.9}$$

The temperature in the varying volume space can be expressed by using the ideal gas law, and derivatives of products can be expanded:

$$T_v = \frac{P_v V_v}{m_v R}; \tag{4.10}$$

$$dT_v = \frac{1}{R}[\frac{P_v}{m_v}dV_v + \frac{V_v}{m_v}dP_v - \frac{P_v V_v}{m_v^2}dm_v] \tag{4.11}$$

Equivalent expressions can be written for T_t, and both these and those for T_v can be substituted into (4.9), resulting in

$$\delta Q_v = -\left[c_v \frac{P_v V_v}{m_v R}dm_v + m_v c_v \frac{1}{R}[\frac{P_v}{m_v}dV_v + \frac{V_v}{m_v}dP_v - \frac{P_v V_v}{m_v^2}dm_v]\right] \tag{4.12}$$

$$-P_v dV_v + \left[c_p \frac{P_t V_t}{m_t R}dm_v\right]$$

To eliminate c_p, c_v, and R, invoke the definition of γ:

$$\gamma = \frac{c_p}{c_v} \qquad \frac{c_v}{R} = \frac{1}{\gamma - 1} \qquad \frac{c_p}{R} = \frac{\gamma}{\gamma - 1} \qquad (4.13)$$

and substitute into (4.12). After some algebra, the final result is

$$\delta Q_v = -\frac{1}{\gamma - 1} V_v dP_v - \frac{\gamma}{\gamma - 1} P_v dV_v + \frac{\gamma}{\gamma - 1} \frac{P_t V_t}{m_t} dm_v . \qquad (4.14)$$

This expression is quite compact, but no physical meaning for the individual terms is evident. It gives heat transfer as a function of measured pressures and volumes and unknown masses.

The expression for the fixed volume space is the same except that "f" subscripts are substituted for the "v"s and the second term on the right hand side is eliminated, since $dV_f = 0$.

Governing Equations: Heat Transfer Using Complex Heat Transfer Coefficients

An expression must now be written to express δQ in (4.14) in terms of a heat transfer model. Writing the complex heat transfer equation for the varying volume space gives

$$\delta Q_v = A_v dt \left[h_{rv}(T_v - T_w) + \frac{h_{iv}}{\omega} \frac{d}{dt}(T_v) \right] \qquad (4.15)$$

Multiplying through by dt and using (4.10) and (4.11) to replace T_v and dT_v results in

$$\delta Q_v = A_v h_{rv} \left(\frac{P_v V_v}{m_v R} - T_w \right) dt + \frac{A_v h_{iv}}{\omega R} \left(\frac{P_v}{m_v} dV_v + \frac{V_v}{m_v} dP_v - \frac{P_v V_v}{m_v^2} dm_v \right) \qquad (4.16)$$

Once again, the expression for the fixed volume space is almost the same. The "f" subscripts are substituted for the "v"s and the term containing dV_f is eliminated.

Governing Equations: Energy Balance

The thermodynamic expression for heat transfer in the varying volume space may now be equated to that based on the complex Nusselt number model, giving

$$-\frac{1}{\gamma - 1} V_v dP_v - \frac{\gamma}{\gamma - 1} P_v dV_v + \frac{\gamma}{\gamma - 1} \frac{P_t V_t}{m_t} dm_v \qquad (4.17)$$

$$= A_v h_{rv} \left(\frac{P_v V_v}{m_v R} - T_w \right) dt + \frac{A_v h_{iv}}{\omega R} \left(\frac{P_v}{m_v} dV_v + \frac{V_v}{m_v} dP_v - \frac{P_v V_v}{m_v^2} dm_v \right)$$

This is the final expression relating the energy transfer within the varying volume space. A similar expression may be written for the fixed volume space:

$$-\frac{1}{\gamma - 1} V_f dP_f + \frac{\gamma}{\gamma - 1} \frac{P_t V_t}{m_t} dm_f \qquad (4.18)$$

Some additional equations, relating the two spaces through conservation of mass, are needed:

$$=A_f\ h_{rf}(\frac{P_fV_f}{m_f\ R}-T_w)dt+\frac{A_f\ h_{if}}{\omega R}(\frac{V_f}{m_f}dP_f-\frac{P_fV_f}{m_f^2}dm_f)$$

$$m_v=m_{tot}-m_f\ ,\ \text{and} \tag{4.19}$$

$$dm_f=-dm_v\ . \tag{4.20}$$

Summarizing, the knowns in (4.17) to (4.20) are: $P_v(t)$, $P_f(t)$, $V_v(t)$, V_f, m_{tot}, $A_v(t)$, A_f, dt, T_w, ω, γ, and R. The unknowns are m_v, m_f, h_{rv}, h_{iv}, h_{rf}, and h_{if}, all functions of t.

Implementation through a Finite Difference Representation

The final forms of the energy equations for each space were rewritten using finite differences for the derivatives. This allowed the equations to be written in terms of discrete values. Many of these values were known from the experimentally measured data. For illustrative purposes, an example of the method will be given here assuming a forward differencing of the derivatives. After discretizing El 4.17 at time t_i, the result is:

$$\frac{1}{\gamma-1}V_{v,i}[P_{v,i+1}-P_{v,i}]+\frac{\gamma}{\gamma-1}P_{v,i}[V_{v,i+1}-V_{v,i}]-\frac{\gamma}{\gamma-1}\frac{P_{v,i}V_{v,i}}{m_{v,i}}[m_{v,i+1}-m_{v,i}] \tag{4.21}$$

$$=A_{v,i}h_{rv}\left[T_w-\frac{P_{v,i}V_{v,i}}{m_{v,i}R}\right][t_{i+1}-t_i]$$

$$-\frac{A_{v,i}h_{iv}}{\omega R}\left[\frac{P_{v,i}}{m_{v,i}}[V_{v,i+1}-V_{v,i}]+\frac{V_{v,i}}{m_{v,i}}[P_{v,i+1}-P_{v,i}]-\frac{P_{v,i}V_{v,i}}{m_{v,i}^2}[m_{v,i+1}-m_{v,i}]\right]$$

All of the values in this equation are known except $m_{v,i}$, $m_{v,i+1}$, and the two h's. A similar equation can be written for the fixed space. Since the total mass in the system is known, the masses in the two spaces are related; they are not additional unknowns. The only additional unknowns are the two h's for the fixed space.

Based on a forward difference at point i there are thus two equations in 6 unknowns: 2 m's and 4 h's. Adding an additional pair of equations written at point $i+1$, however, adds only one more unknown: m_{i+2}. (Assuming that the heat transfer coefficients do not vary over this small time range.) If equations are written for n sequential points, the number of equations is $2n$, while the number of unknowns is $5+n$. If the all the energy equations are independent, the system is determined when $n=5$. This is true for backward differencing also; for center differencing $n=6$ is required.

Thus for each set of 5 or 6 data points a set of masses and heat transfer coefficients can, in theory, be calculated. Since this span corresponds to only 4 or 5 degrees of crank angle, the assumption of constant h's seems reasonable. The values of h calculated can be assigned to a

point at the center of the window, and the window can then be moved to calculate h's at the next center point.

There are two problems to be faced in solving these equations:
- How are the solutions to be found? The equations are nonlinear, making this problem difficult.
- Is the solution unique? If it is not, can the physically realistic solution somehow be selected?

Solution Efforts

The standard method used for solving systems of non-linear equations is the Newton-Raphson method. This very simple method considers only the gradient for each of the unknown variables with respect to the solution. It linearizes the equations and calculates the step required for each of the variables to arrive at solution of the linear problem.

The solution method was tested against a simulated data set developed using the same set of equations used in the solution, plus an orifice flow equation. The plan was to add noise and error to this data set after convergence on the ideal simulated data had been demonstrated. The method, however, never converged even on the ideal data. If the known solutions were selected for the algorithm's initial guess, it would recognize the solution. If any other guess was made, now matter how close to the solution, the method would diverge.

Different attempts were made to determine the nature of the problem which inhibited steady progress of the independent variables toward some solution. Some of the issues examined were:

- The number of significant digits in the discrete math. Although the heat transfer terms in the energy balance were six to eight orders of magnitude less than the internal energy terms, the program was run in double precision, giving 15 significant digits. Numerical truncation error should thus not have been a problem.

- The algorithm used by the equation solver. In addition to the Newton-Raphson method, Levenberg-Marquardt and Gauss-Newton algorithms were tried. Neither showed any signs of convergence.

- The set of experimental data used. The method was tested on simulated data for different operating conditions and for different parts of the cycle at each operating condition. None of the cases showed improved convergence.

- The discretization method for the derivatives. Various finite differencing techniques were tried. No improvement was evident.

- The step size used for the discretization. Though the experiment was designed for ~400 points/cycle, the simulating could be run with any desired number of points. Decreasing the step size, however, did not aid convergence.

- The complexity of the problem. Some of the unknowns were set to the correct values, leaving fewer unknowns. When the number of unknowns was reduced, solutions were tried both with reduced equation sets and with overspecified equation sets and an optimizing, rather than solving, technique. Solutions could be found in this way, but only if six to eight of the ten variables were constrained. The investigation did not show any particular variable as the root of the problem.

It was this last set of tests that led to abandonment of the solution technique. The results with partly constrained data sets seemed to indicate that the basic problem was that there were multiple, closely spaced solutions or near-solutions. Based on this belief, it was felt that any further attempts to use the no model method were futile.

From a physical standpoint, it appears that without an orifice flow model there are many different sets of heat transfer coefficients that can produce a measured or simulated pressure variation. Some sort of orifice flow model is thus necessary.

4.3 Unsteady Orifice Model Approach

Based on the results of the attempts to calculate heat transfer without a model of flow through the orifice, it was decided to include such a model in the data analysis technique. Existing semi-empirical models for steady flow through orifices are quite accurate, but their accuracy is questionable in cases of oscillating flow. In order to incorporate oscillating flow effects, the existing models were extended to include unsteady acceleration effects, and model parameters were left as unknowns.

With the addition of the fluid mechanics models, it may be possible to solve for heat transfer by simply extending the no model approach: adding the flow equation to the two energy equations and applying them over a short range of data points. In order to speed algorithm development, however, an additional assumption was made: that complex Nusselt numbers and orifice coefficients were essentially constant over a cycle.

With this assumption, a given set of orifice and heat transfer coefficients could be used to predict the pressure-volume-time behavior of the experiment. The prediction was based on the measured volume data, and was then compared to the measured pressure data. The coefficients modified until the measured data was matched.

The method thus has two main parts: simulating the pressure variation for given coefficients and a given volume variation, and optimizing the coefficients based on such simulations. Before these procedures can be implemented, an unsteady orifice flow model must be developed.

Orifice Model for Unsteady Flow

The well known semi-empirical equation for steady incompressible flow through an orifice in a pipe is

$$\dot{V} = C_d A_0 \sqrt{\frac{2\, \Delta P/\rho}{1-\beta^4}}.$$ (4.22)

Here:

V	=the volume flowrate,
C_d	=the discharge coefficient,
A_0	=the cross sectional area of the orifice,
ΔP	=the differential pressure across the orifice,
ρ	=the density of the gas, and
β	=the vena contracta ratio.

Although the working fluid in this experiment is compressible, the density difference in the flow across the orifice is so small that the incompressible model introduces negligible error.

Tabulated data on C_d for pipeline orifices is readily available, but this data may be inapplicable to the experiment, both because of unsteady effects and because of the change in flow patterns caused by the proximity of the piston to the orifice. In order to avoid introducing errors by using steady pipe flow C_d's, the flow coefficient is left as an optimized variable. To simplify the orifice equation, the both C_d and β are combined into a single coefficient, $k_1 = C_d(1-\beta^4)^{-1/2}$. With the assumption that the density of the flowing fluid was the upstream density, the steady orifice equation in terms of mass flow becomes

$$\frac{dm_{v-f}}{dt} = \dot{m}_{v-f} = k_1 A_0 \sqrt{2\rho_t (P_v - P_f)} \;.$$ (4.23)

Solving for the pressure drop and modifying to generalize it for flow in either direction:

$$P_v - P_f = k_1 \frac{\dot{m}_{v-f} |\dot{m}_{v-f}|}{2\rho_t A_o^2}.$$ (4.24)

In simulating the pressure-volume-time data, k_1 is assumed constant over the cycle.

In order to include the inertial effect of periodic flow acceleration, it is assumed that a cylinder of fluid of area A_0 and length L is accelerated as flow through the orifice changes. The differential pressure is then related to the acceleration by

$$P_f - P_v = \left(\rho_t A_o L\right)\left(\frac{dv_{f-v}}{dt}\right)\frac{1}{A_o} = (\rho_t L)\frac{d}{dt} v_{f-v}.$$ (4.25)

Writing the velocity in terms of the mass flow gives

$$P_f - P_v = \rho_t L \frac{d}{dt}\left(\frac{\dot{m}_{f-v}}{\rho_t A_o}\right) = \frac{L}{A_o}\ddot{m}_{f-v}.$$ (4.26)

To non-dimensionalize the length, it was assumed that it is proportional to the square root of A_o. Picking the constant of proportionality to be k_2:

$$L = k_2\sqrt{A_o}.$$ (4.27)

Substituting this in gives the final expression for the pressure difference required to accelerate the flow:

$$P_f - P_v = \frac{k_2}{\sqrt{A_o}} \ddot{m}_{f-v}.$$

(4.28)

The coefficient k_2, like k_1 in the steady flow orifice equation, is assumed to be constant and optimized for best fit to the experimental data.

Combining (4.24) and (4.28) gives an expression for total pressure difference across the orifice as a function of mass flow:

$$P_f - P_v = k_1 \frac{\dot{m}_{f-v} |\dot{m}_{f-v}|}{2\rho_f A_o^2} + k_2 \frac{\ddot{m}_{f-v}}{\sqrt{A_o}}.$$

(4.29)

Simulation of Pressure Variations

The two energy equations and the orifice flow equation provide a means of simulating the pressure variation in both spaces for a given volume variation. The only additional information that is required is initial conditions and values for six coefficients: two h_r's, two h_i's, and two k's, The initial conditions will be determined by the requirement for cyclic steady state. The coefficients will be selected to give a best least-squares fit to the measured pressure.

In the first simulations done as part of this work, those done to provide simulated data for the "no fluid mechanics model" approach, a finite difference technique was used. It was found that very small step size was required for stability, making the technique very computation-intensive. Even with small step size, there were stability problems at top and bottom center (flow reversal) that could only be solved by limiting the orifice flow in any one time step to that which would equalize pressure in the two spaces.

The large computational requirements of the finite difference model were acceptable when developing a few sets of simulated data for the "no model" approach, but were much too long for the repeated simulations needed for the parameter optimization. It was found that a variable step size Runge-Kutta integration provided results much more quickly.

The tolerance parameters of the Runge-Kutta algorithm had to be set for very stringent values to keep integration inaccuracies from upsetting the parameter optimization procedures. Required step size depended on the parameter values, smaller steps being required for the more adiabatic, more reversible cases. Small values of k_2, the inertial orifice coefficient, also required small step sizes. In cases where the optimization drove values of k_2 very small, its minimum value was limited by overriding the optimizer. This introduced little error, as it was only invoked when the contribution of k_2 to ΔP was very small.

In order to use the variable step size Runge-Kutta approach on the experimental data, a method was needed for interpolating the volume data for steps smaller than the ~400/cycle measured by the instrumentation. This was done using Fourier transform techniques. The measured volume trace was decomposed into Fourier coefficients, high-order coefficients were discarded, and the

remaining coefficients were stored. For each step required by the Runge-Kutta algorithm the coefficients were then recombined using Lanczos smoothing (Hamming, 1983) to determine the volume. The number of coefficients kept was determined by examining the residual between measured volume traces and the recombined signal and determining, visually, if there was any non-noise content. It was found that 15-40 coefficients were required, depending on the data set used. Using too many coefficients increased integration time, since the evaluation of volume had to be made repeatedly.

The time required for a full simulation using a given parameter set was also influenced by the cycle closure criterion and the algorithm used to update the initial conditions before beginning a new integration.

Mid-stroke was chosen as the initial starting point and the updating point. It was selected because dissipation in the orifice was highest at mid-stroke, and dissipation adds stability. Top center or bottom center might also have been suitable points, since dissipation due to heat transfer is maximum at those positions.

At first, the updated initial conditions were found by straight substitution of the conditions at the end of the simulated cycle. This was unacceptable, as closure sometimes required hundreds of cycles. Newton-Raphson and Gauss-Newton algorithms were also tried for the updating. They gave faster closure than straight update, but suffered from instability problems. As with the Runge-Kutta technique itself, instability problems were worst under nearly reversible conditions. Finally, a Levenberg-Marquardt non-linear solver was used. It gave reasonably fast closure under all conditions without instability problems.

It was thus possible to simulate the apparatus cycle for any reasonable values of the six parameters to be optimized.

4.3 Results of Simulations

Although the purpose of the simulations was to determine the heat transfer and heat transfer coefficients for each space individually, it is of interest to examine the effects on the pressure trace of varying each of the coefficients. This not only helps in understanding the effect of these coefficients on the experimental apparatus, but may give some insight into their effects on Stirling engines.

Some typical simulated results are shown in Figures 4.1 and 4.2. Figure 4.1 shows volume and pressure traces, while 4.2 shows varying volume temperature and heat flux traces. Figure 4.1 shows that the pressure in the varying volume space (space 2) lags slightly behind that in the fixed volume space (space 1). The difference is slight. Figure 4.2 shows the simulated 45° phase difference between heat transfer and temperature difference. An interesting feature is the discontinuity in the temperature and heat flux traces near 270° (top center). The discontinuity occurs because of flow reversal and because the mass in the top center clearance volume is very small.
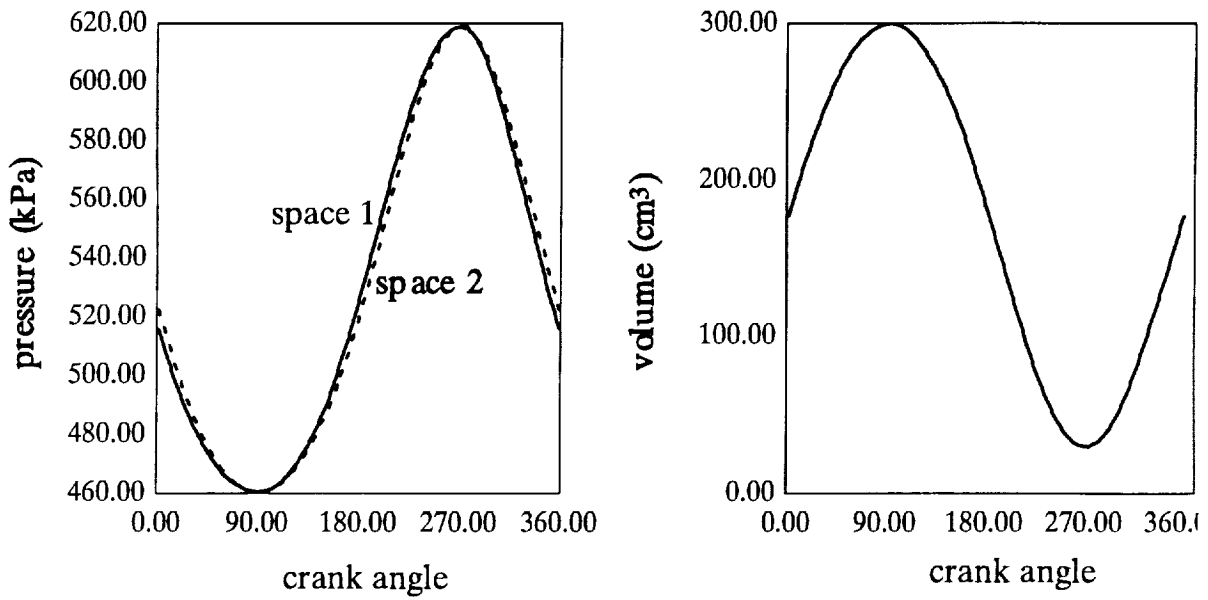
4-10

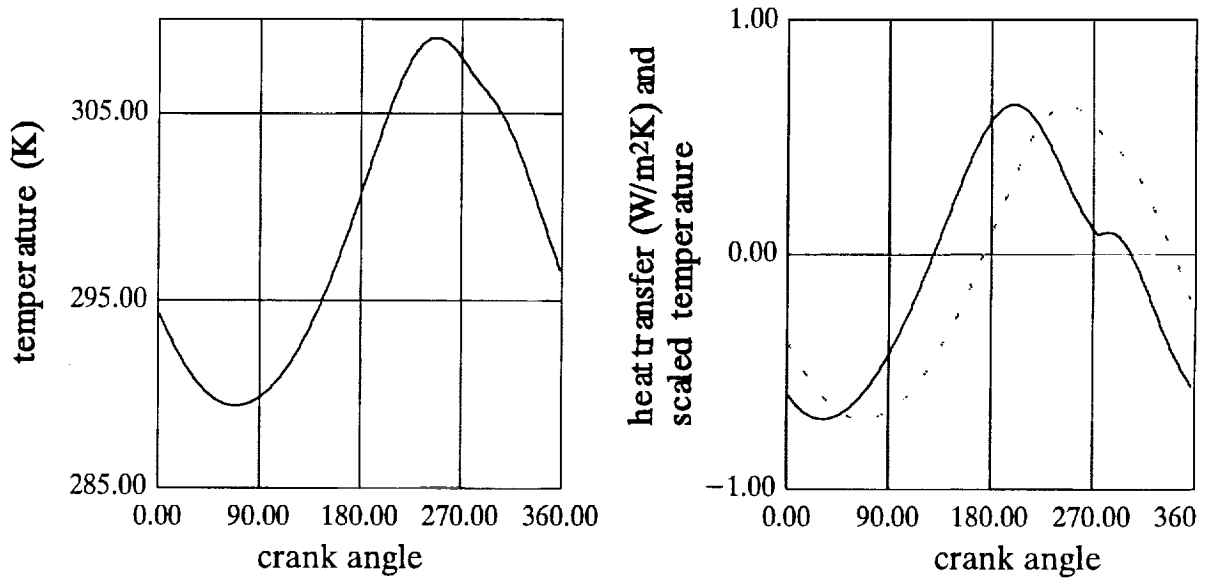Figure 4.1 Typical Transient Traces for Pressure and Volume (600 rpm, 5 atm).

Figure 4.2 Temperature and Heat Flux vs. Crank Angle from Mid-Expansion, Varying Volume Space (120 rpm, 5 atm, h's 5000 W/m^{2}K, k's 5)

Effect of Varying the Heat Transfer Coefficients

An effect that was noticeable when varying all the heat transfer coefficients was that once h's were made quite large or quite small, additional change had little effect on the pressure trace. The values of h's that did have an effect depended, of course, on the pressure and speed (Pe_ω) of a given run. Figure 4.3 shows the variation in simulated pressure trace over a range of h's.

Increasing the magnitude of the heat transfer coefficient decreases the amplitude of the pressure trace, with the change in pressure amplitude per change in h greatest at intermediate values of h. This effect is also seen in the P^* results from the single space experiments. The pressure trace at low and high values of h lags that at intermediate values of h. This effect is also seen in the Φ_P results from the single space experiments.

A comparison of the affects of real and complex heat transfer on the pressure trace are shown in Figure 4.4. The ~45° degree phase shift in heat transfer results in a much smaller phase shift in pressure.

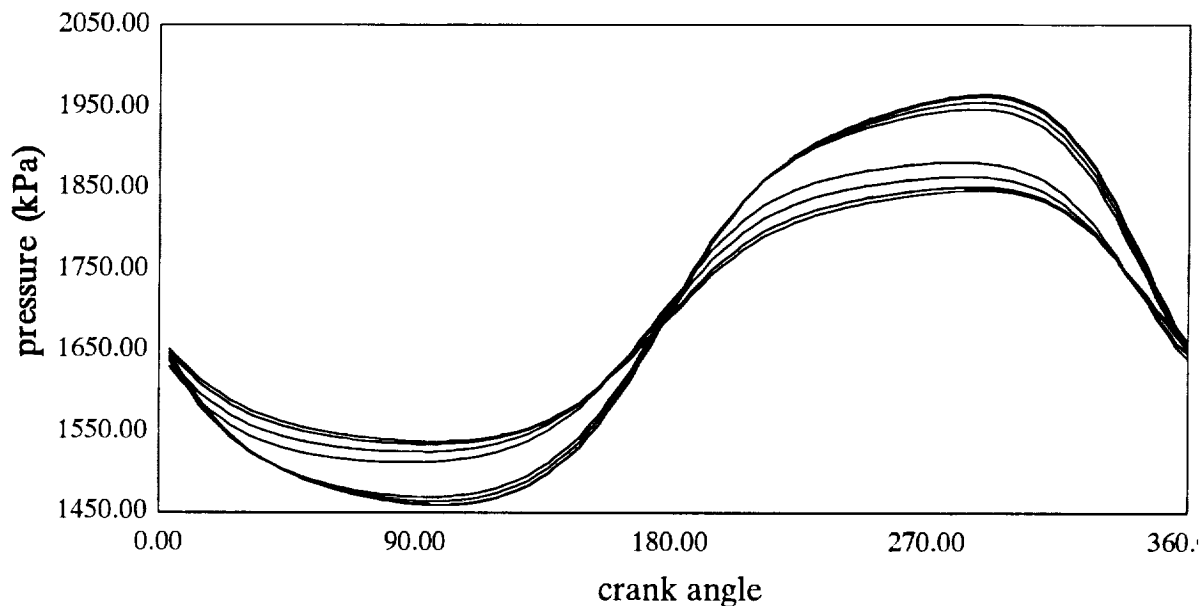Figure 4.3 Amplitude of Pressures for Different Magnitudes of Heat Transfer (30 rpm, 17.5 atm, 1 W/m²K < h's < 10,000 W/m²K)

Effect of Varying the Orifice Flow Coefficients

Based on an orifice C_d of 0.6-0.8 and the β ratio of the apparatus orifice, the expected value of k_1 is 1.2-1.6. The expected value of k_2 is more difficult to estimate, but it is expected to be of order of magnitude 1.
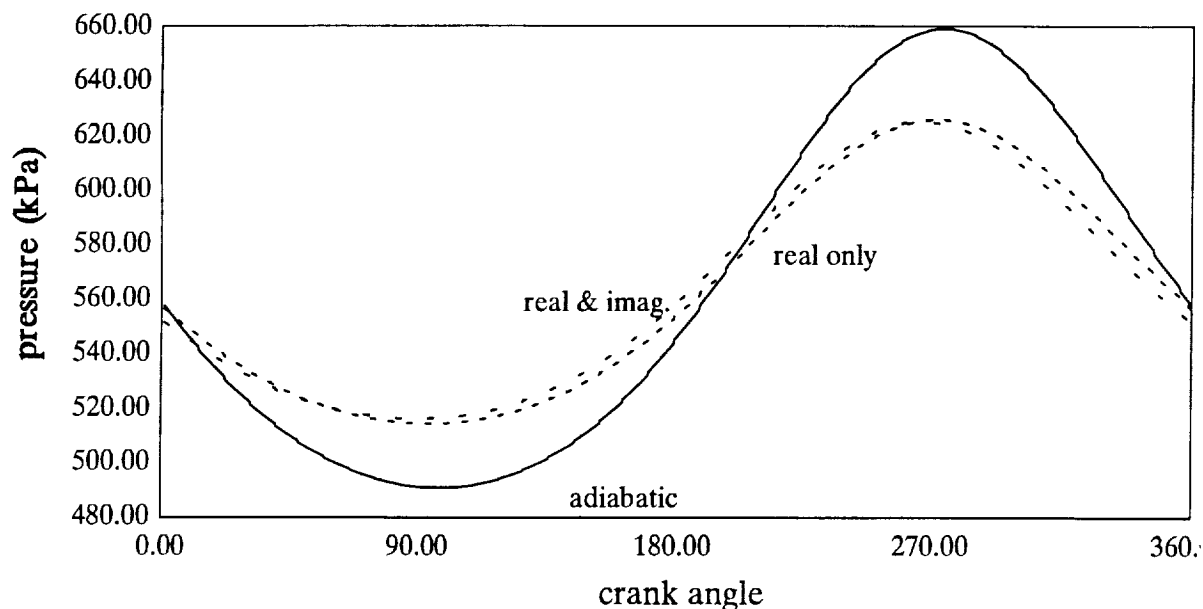
4-12

Figure 4.4 Pressure for Real and Complex Heat Transfer vs. Crank Angle from Mid-Expansion (120 rpm, 5 atm, h's 500 and 5000 W/m^{2}K, k's 5)

Figure 4.5 shows the effect on differential pressure of varying k_1. The magnitude of the differential pressure increases with increasing k_1, and there is no noticeable phase shift effect.

Figure 4.6 shows the effect on differential pressure of varying k_2. Increasing k_2 increases the magnitude of ΔP and causes a phase lead. For reasonable values of k_2, however, the effect is small.

4.4 Optimization of Heat Transfer and Flow Coefficients

The heat transfer and flow coefficients were optimized using a Leveberg-Marquardt algorithm with a mixed cubic/quadratic search technique. The algorithm used was the one provided with the Matlab (TM, Math Systems) software package. The criterion for optimization was the least squares difference between the actual pressure data and the simulated pressure data.

The progress of a typical optimization using Levenberg-Marquardt is shown in Figure 4.7. The way in which the coefficients tend toward their optimum values demonstrates something of how the optimizer works.

First, a series of iterations is made without changing the values of any of the coefficients. During these iterations each individual coefficient is perturbed slightly so as to determine the gradient in each of the six directions. When the gradients in each direction are determined, they are combined to decide which direction (in 6-space) leads most directly to the optimum.
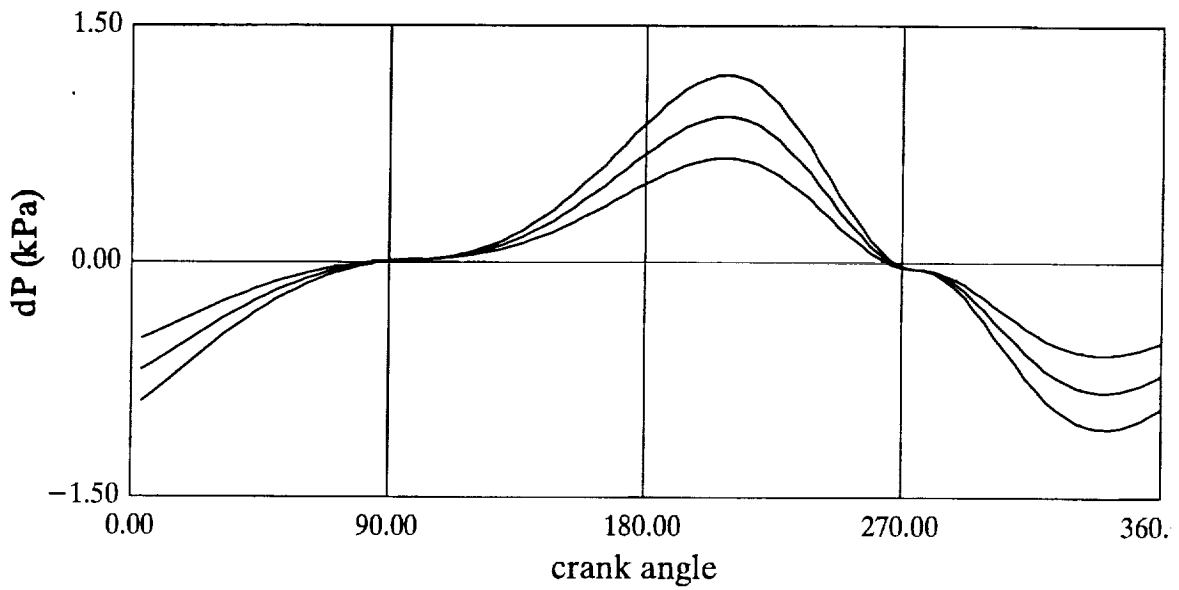
4-13

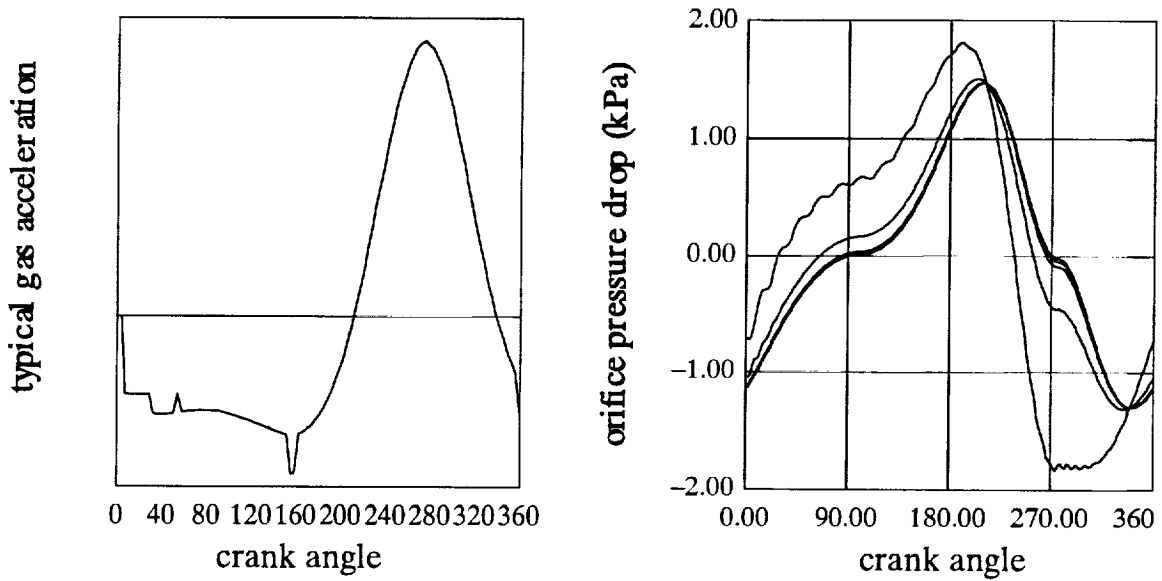Figure 4.5 Differential Pressure vs. Crank Angle from Mid-Expansion for $1<k_1<10$ (120 rpm, 5 atm, h's=100 W/m^{2}K, k_2=5)

Figure 4.6 Gas Acceleration and Differential Pressure vs. Crank Angle from Mid-Expansion, $0.1<k_2<500$ (120 rpm, 5 atm, h's=200 W/m^{2}K, k_1=11)

Then, the optimizer takes a large step in the appropriate direction, varying all the coefficients at once. Based on the results of this large step, which always overshoots, it selects a smaller step in the same direction. It continues to adjust step size, without changing direction, for 3 or 4 iterations. Then in begins another evaluation of the gradients.

The process was quite time consuming, since each of the "loops" shown in Figure 4.7 represents as many loop integrations of the Runge-Kutta integrator as were required to get cycle closure. Run times were longer for more nearly reversible cases; for many the time required on an IBM RISC workstation was over 12 hours. Almost all the time was spent in Runge-Kutta integration, which was Fortran coded. The Matlab code used for the Levenberg-Marquardt optimizer was slow, but it represented only a very small fraction of the total run time.
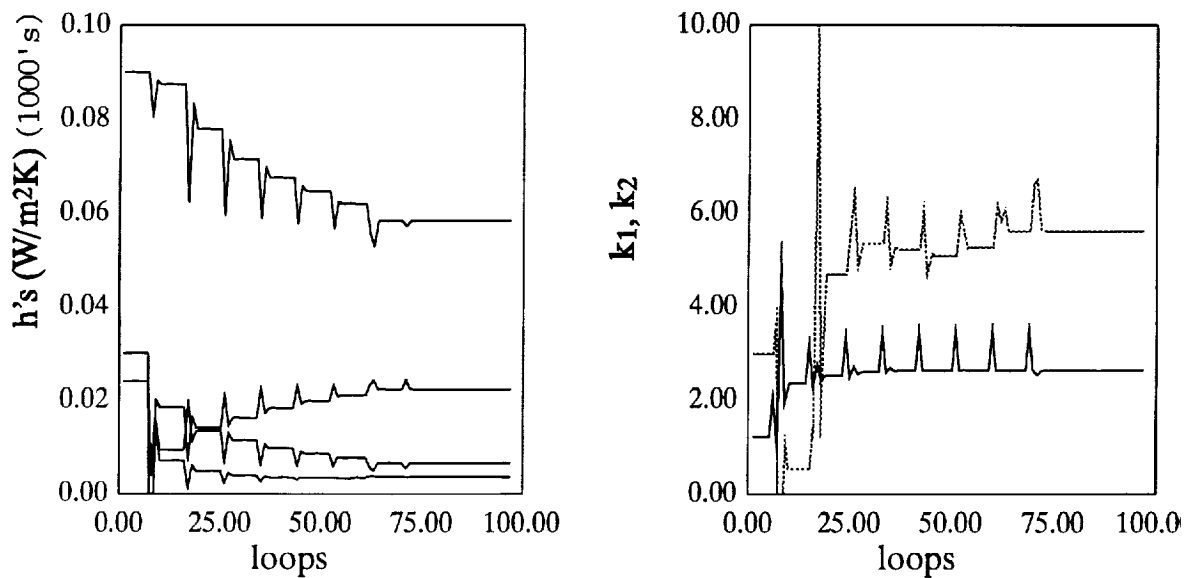

Figure 4.7 Typical Progress for Optimization of the Coefficients

4.5 Coefficient Optimization with Simulated Data

Before applying the two space data analysis technique to experimental data, it was tested on simulated pressure data. The data was all simulated using the same energy equations, flow models, and Runge-Kutta integrator used in the optimization routine, plus real volume-time data. Since the physical model for the simulation and optimization were the same, the procedure only tested the optimization procedure and would not find other errors.

After this test, a more demanding one was carried out: the optimizer was tested on simulated pressure data with added noise. The noise was produced by a random number algorithm, and its amplitude was selected to match the amplitude of the observed noise in the experimental pressure measurement.

The coefficient changes shown in Figure 4.7 are from an optimization with noise-free simulated data.

Optimization with Noise-Free Simulated Data

first simulated data set was based on operation at volume ratio 1.2, the orifice selected for $Re_{in}/Pe_{\omega}=100$, 5 atm mean pressure, and 2 Hz. The results of some optimization tests are shown in Table 4.1; the coefficients used in the simulation are shown in the first row of data.

Table 4.1 cases a through d were run to test whether different guesses for h would result in convergence to the same values. In these optimizations the values of or the k's were held and not optimized, in order to save computation time. The h's converged to the same values for all initial guesses. The difference between the converged values and those used in the simulation was due to the k's being locked to a value different from the simulated value. This force k error resulted in a mismatch to the pressure data, shown in the least squares residual error.

In Table 4.1 case e, the converged h's from a previous case were used as initial guesses and the k's were allowed to optimize as well. The values of all coefficients converged to within 0.01% of the values used in the simulation, and pressure residual errors were extremely low.

The optimization procedure was clearly successful with noise-free simulated data, a definite improvement over the "no model" approach.

Table 4.1 Converged Coefficients; No Noise Added; 2 Hz, 5 atm
(h's in kW/m²/K)

Case	h's guess	P Residual, %	hrv	hiv	hrf	hif	k1	k2
Simulation	n.a.	n.a.	0.20	0.18	0.01	0.15	9	9
a	.5	.026745	.11	.19	.037	.15	held @ 5	held @ 5
b	.4	same	same	same	same	same	same	same
c	.2	same	same	same	same	same	same	same
d	.1	same	same	same	same	same	same	same
e	prev. convg.	2.75e-6	.2	.18	.01	.15	9	9

Table 4.2 Converged Coefficients; Noise Added
(h's in kW/m²K)

Case	h's guess	Resid, %	hrv	hiv	hrf	hif	k1	k2
Simul.	n.a.	n.a.	0.20	0.18	0.01	0.15	9	9
e,1	.5	.045591	.11	.18	.037	.15	held @ 5	held @ 5
f,1	.3	same	same	same	same	same	same	same
g,1	.1	same	same	same	same	same	same	same
h,1	prev. convg.	not avail.	.199	.177	.0108	.150	8.80	10.5
e,2	.5	.039844	.24	.17	.00055	.15	held @ 11	held @ 11
f,2	.1	.039842	.24	.18	.000013	.15	same	same
g,2	prev. convg.	.037176	.19	.17	.013	.15	8.9	4.7
h,3	.1	.040602	.25	.21	.000099	.14	held @ 11	held @ 11
i,3	prev. convg.	.037798	.200	.176	.0106	.15	8.8	10.5
j,3	.1	not avail.	.202	.1834	.01094	.1497	9.2	7.4
k,3	.1	.045591	.111	.180	.0363	.153	(5)	(5)
l,3	prev. convg.	.037798	.200	.179	.000054	.15	8.9	6.7

Optimization with Noisy Simulated Data

Numerically-generated "random" noise was added to the simulated data to give an noise level that visually appeared equal to that in actual experimental data. Since the signal to noise level of the actual pressure measurements was so large as to make the noise almost invisible, the noise visible in the orifice ΔP measurement was used for comparison.

The results of some convergence tests are shown in Table 4.2. The simulated data was the same as that used in the noise-free simulated data except for the addition of noise. Three different sets of random noise were used, all of the same least-squares amplitude but of different random content. These are numbered 1, 2, and 3 on the table. For each of the noise sets different initial guesses were tried, some of them with the values of k kept from optimizing.

Table 4.2 shows that the noise introduced some error into the optimized coefficients. For a given set of random noise, the coefficients converged to almost the same value for any initial guess; there was, however, a small initial guess effect. The nature of the random noise, however, affected the converged values: each of the three random noise sets shown in the table resulted in different values of the optimized coefficients.

In order to further test the effects of noise, optimization was carried out with the same simulated data set and 14 additional sets of random noise. The resultant errors are summarized in Table 4.3. Some of the errors are quite high. The mean values of the various optimizations with noisy data are, however, very close to values used in the simulations.

The fact that noise effects canceled out when averaged over many different sets of noise is important. It indicates that by using data sets from multiple cycles, the error caused by noise could be reduced to acceptable levels. Collection of many-cycle data sets was put off, however, until the optimization procedure had been tested against real data from single cycles.

Table 4.3 Max % Error on Converged Coefficients w/Noise: 2 Hz, 5 atm

	hrv	hiv	hrf	hif	k1	k2
Simul.	0.20	0.18	0.01	0.15	9.0	9.0
Mean	0.1932	0.1970	0.0086	0.1472	9.170	9.030
Max % Err	14	25	64	4	7	92

Figure 4.8 gives an idea of the level of noise and of the pressure residual in the simulated data plus noise tests. The overall pressure swing of the simulated run was more than 650 kPa.
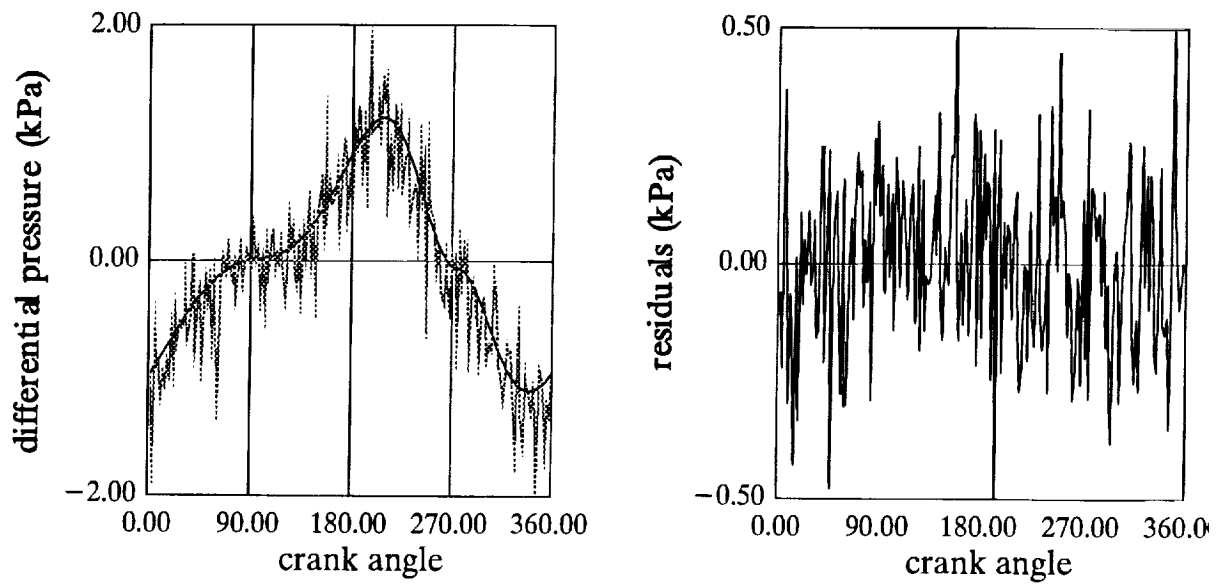
Figure 4.8 Differential Pressure and Pressure Residuals vs. Crank Angle from Mid-Expansion (120 rpm, 5 atm)

5. Single Space Results

5.1 Nondimensional Pressure Magnitude

The nondimensional pressure magnitude was found to be a function of oscillation Peclet number, increasing with increasing Pe_ω as shown in Figure 5.1. All the data collected were near the adiabatic end of the possible P^* range.

Kornhauser and Smith (1993) measured the pressure magnitude at different engine geometries and with different working fluids. They found that Lee's (1983) explained the variations in P^* with speed, mean pressure, gas specific heat ratio, and cylinder geometry. The model did not, however, explain the variation of P^* with volume ratio. Kornhauser and Smith's experimental results showed P^* at $r_v=2$ matching Lee's predictions, but P^* at $r_v=4$ and 8 considerably smaller than Lee's prediction. Since Lee's model was based on $r_v \to 1$, Kornhauser and Smith postulated that the Lee's model would be satisfactory over the range $1 \le r_v \le 2$.

Figure 5.2 shows that this postulate was correct. The figure plots the older results at volume ratios 2, 4, and 8 with the new results at volume ratio 1.1. The $r_v=1.1$ results closely match those at $r_v=2$.

5.2 Pressure Phase Lead

Pressure phase lead was found to be a function of oscillation Peclet number, decreasing in proportion to $Pe_\omega^{-1/2}$.

Kornhauser and Smith (1993) measured the pressure phase lead at different engine geometries and with different working fluids. They found that Lee's (1983) explained the variations in Φ_P with speed, mean pressure, gas specific heat ratio, and cylinder geometry. The model did not, however, explain the variation of Φ_P with volume ratio. Kornhauser and Smith's experimental results showed Φ_P at $r_v=2$ matching Lee's predictions, but Φ_P at $r_v=4$ and 8 considerably higher than Lee's prediction. Since Lee's model was based on $r_v \to 1$, Kornhauser and Smith postulated that the Lee's model would be satisfactory over the range $1 \le r_v \le 2$.

Figure 5.4 shows that this postulate was correct. The figure plots the older results at volume ratios 2, 4, and 8 with the new results at volume ratio 1.1. The $r_v=1.1$ results closely match those at $r_v=2$.
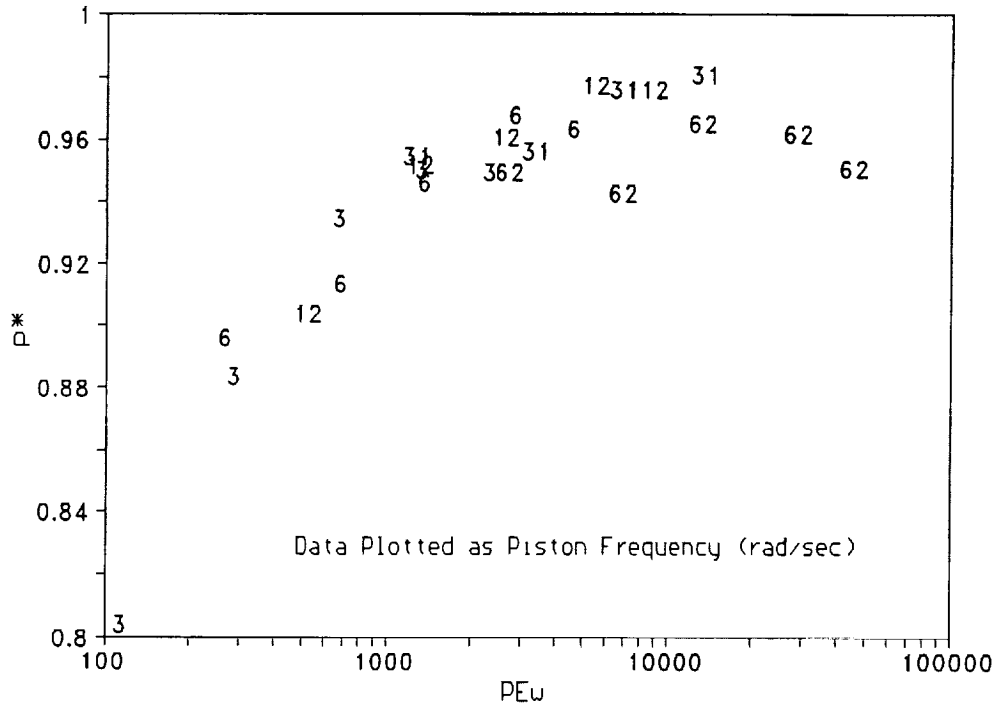
Figure 5.1 Nondimensional Pressure Magnitude vs. Oscillation Peclet Number, Single Space, various Frequencies, Volume Ratio 1.1.
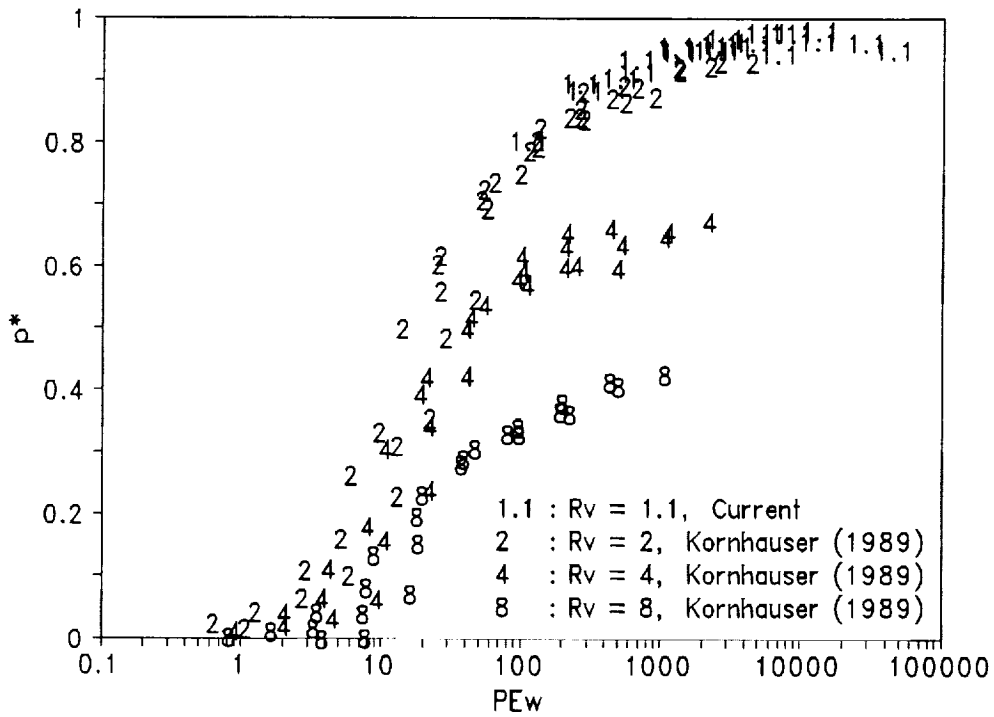

Figure 5.2. Nondimensional Pressure Magnitude vs. Oscillation Peclet Number, Volume Ratio 1.1 (Current Results), 2, 4, and 8 (Previous Results).
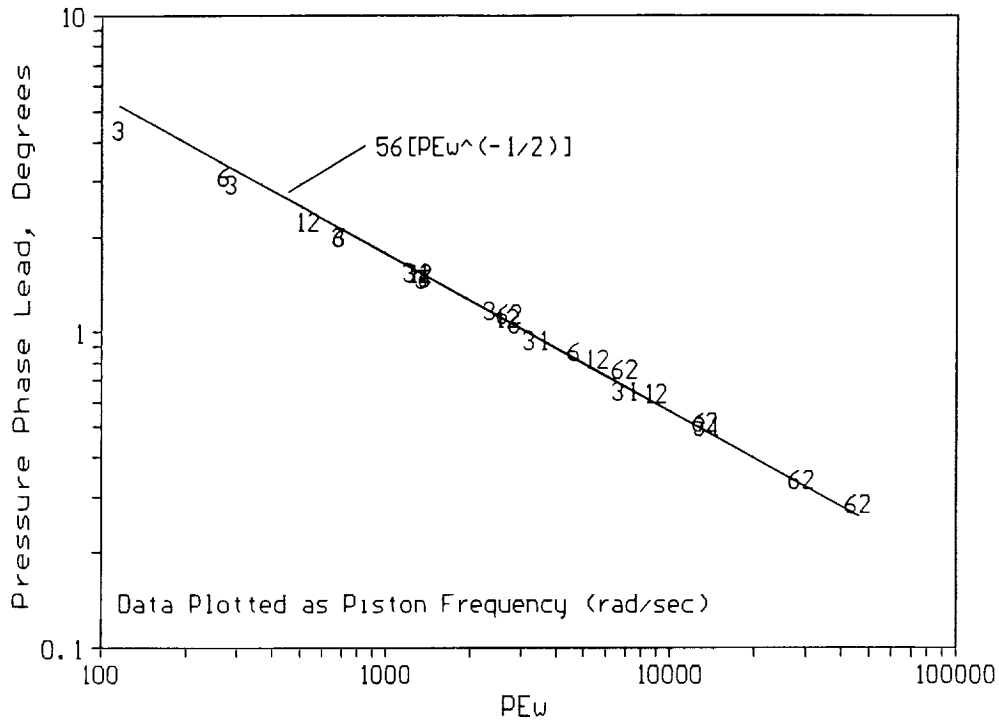
5-2

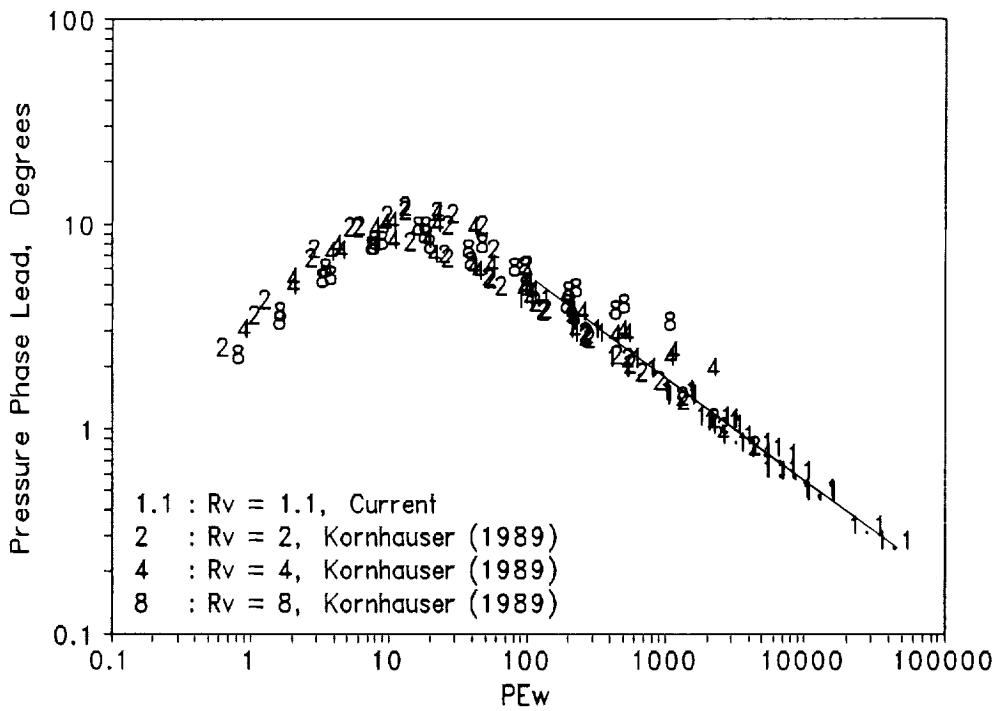Figure 5.3 Pressure Phase Lead vs. Oscillation Peclet Number, various Frequencies, Volume Ratio 1.1.

Figure 5.4. Pressure Phase Lead vs. Oscillation Peclet Number, Volume Ratio 1.1 (Current Results), 2, 4, and 8 (Previous Results).

5.3 Nondimensional Loss

Nondimensional loss was found to be a function of oscillation Peclet number, decreasing in proportion to $Pe_\omega^{-1/2}$. These results are shown in Figure 5.5.

Kornhauser and Smith (1993) measured the nondimensional loss at different engine geometries and with different working fluids. They found that Lee's (1983) explained the variations in $Loss_{nd}$ with speed, mean pressure, gas specific heat ratio, and cylinder geometry. The model did not, however, explain the variation of $Loss_{nd}$ with volume ratio. Kornhauser and Smith's experimental results showed $Loss_{nd}$ at $r_v=2$ matching Lee's predictions, but $Loss_{nd}$ at $r_v=4$ and 8 considerably higher than Lee's prediction. Since Lee's model was based on $r_v \rightarrow 1$, Kornhauser and Smith postulated that the Lee's model would be satisfactory over the range $1 \le r_v \le 2$.

Figure 5.6 shows that this postulate was correct. The figure plots the older results at volume ratios 2, 4, and 8 with the new results at volume ratio 1.1. The $r_v=1.1$ results closely match those at $r_v=2$.

5.4 Gas Thermocouple Temperature Measurements

The fast-response gas thermocouple was intended to measure the temperature of the gas flowing through the orifice. Even though there was no orifice in the single space experiments, the thermocouple was left in place and its output recorded. The results are of interest.

Figure 5.7 shows the gas thermocouple temperature measurement together with the uncorrected temperature measurement from pressure-volume data for a typical single space run. Three points are of interest:

1. The cycle-average mass mean temperature is offset from the thermocouple temperature by about 7 K (13 R). This is due to leakage into the working space during the time for the apparatus to reach steady state. (Since the bounce volume is at near working pressure mean volume, leakage in is as likely as leakage out.) A leakage adequate to offset the mean pressure by only 2.3 kPa (0.37 psia) would explain this temperature offset. A correction, explained in Section 3.1, was used to rectify this offset.

2. The thermocouple temperature signal slightly lags the mass mean temperature. This lag is thought to be due to thermocouple response time. The lag (in terms of degrees) was found to be larger at higher speeds, corroborating this theory.

3. The thermocouple signal shows a definite dip in the region of piston top center. This dip is thought to be due to the thermocouple entering the piston's wall boundary layer. The thermocouple is only about 0.64 cm (0.25 in) above the piston. At low Pe_ω, when thermal boundary layers were thick, the thermocouple was inside the boundary layer and the data showed the dip. At high Pe_ω, when the thermal boundary layer were thinner, no dip showed.

Figure 5.5 Nondimensional Loss vs. Oscillation Peclet Number, Single Space, various Frequencies, Volume Ratio 1.1.

Figure 5.6. Nondimensional Loss vs. Oscillation Peclet Number, Single Space, Volume Ratio 1.1 (Current Results), 2, 4, and 8 (Previous Results).

570

560

Temperature (R)

550

540

530

520

0   60   120   180   240   300   360

Degrees from Bottom Center

Mass Mean Temperature

Gas Thermocouple

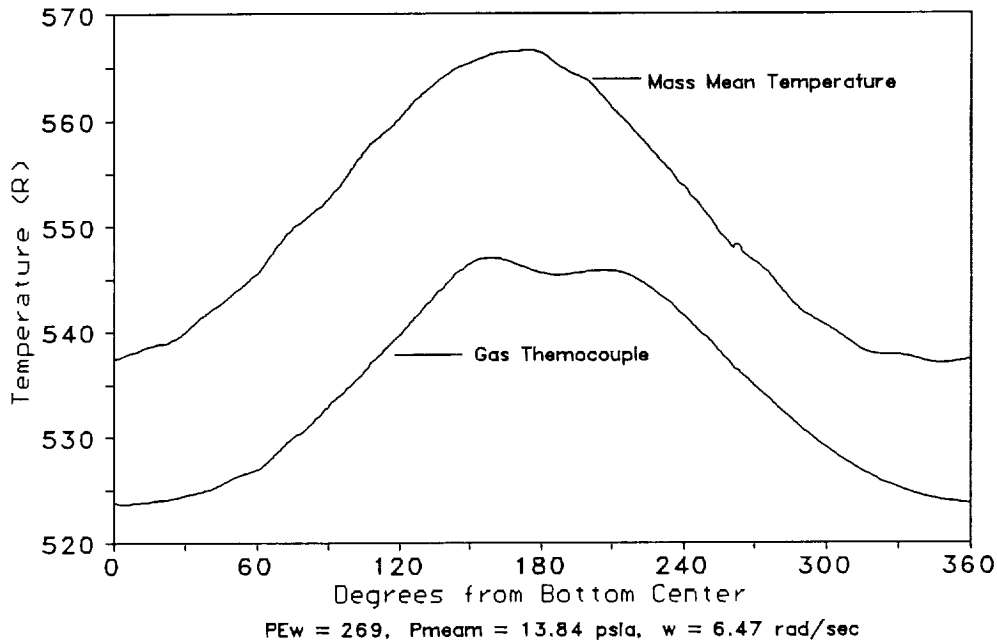PEw = 269, Pmeam = 13.84 psia, w = 6.47 rad/sec

Figure 5.7 Comparison of Uncorrected Mixed Mean Temperature and Gas Thermocouple Temperature Measurements, Typical Single Space Experiment.

5.5 Heat Flux Measurements

Heat flux measurements from both *PV* data (surface averaged) and the surface heat flux sensor (local, sensor mounted in head of fixed volume space) are shown in Figures 5.8-5.10.

Figure 5.8 shows heat flux traces for a typical low pressure, low frequency run. *PV* and sensor heat flux measurements match fairly well, but both show considerable noise.

Figure 5.9 shows heat flux traces for a typical high pressure, low speed run. *PV* and sensor heat flux measurements match fairly well, and noise levels are considerably than for the low pressure, low speed run.

Figure 5.10 shows heat flux traces for a typical high pressure, high speed run. It appears probable that the *PV* and sensor heat flux measurements are close, but the noise in the *PV* measurements is so large as to largely obscure the real heat flux.

The noise in the *PV* heat flux measurement is unacceptably high in the high speed case. In general, noise in *PV* heat flux measurement increases with
* decreasing pressure. This is because the signal to noise ratio of the pressure transducers becomes poorer. The increase in pressure signal noise is somewhat ameliorated by the increase in heat transfer relative to work as Pe_w becomes lower.
* increasing speed. High frequency transducer noise becomes more of a problem as speed

5-6

increases. Also, the magnitude of heat transfer relative to work becomes smaller as speed increases.

The extremely high noise levels shown in Figure 5.10, however, were attributed to the noise and non-sinusoidal components introduced to the volume signal by the slack in the piston driving linkage. This problem was corrected in subsequent runs, but the single space experiments were not repeated.

In runs where noise was not a problem, the similarity of the sensor and *PV* heat flux measurements show that the heat transfer to the head, where the sensor was located, differed little from the space averaged heat transfer.

The runs also showed the heat transfer phase shift typical of many previous experiments.
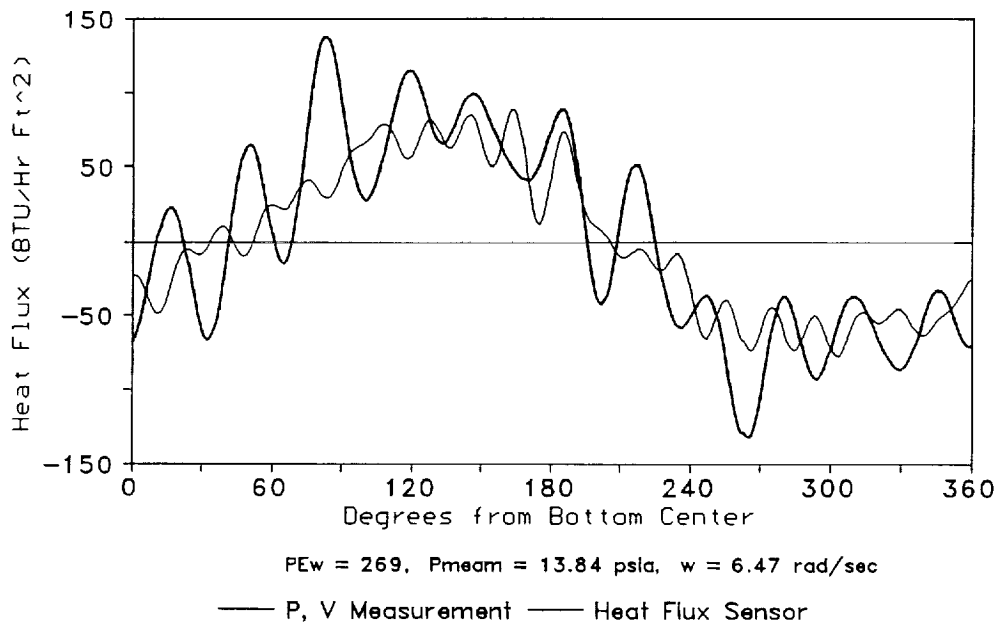

PEw = 269, Pmeam = 13.84 psla, w = 6.47 rad/sec

———— P, V Measurement ———— Heat Flux Sensor

Figure 5.8 Measured Heat Flux, Low Pressure and Low Frequency, Single Space.

5-7

PEw = 4677, Pmean = 237.74 psia, w = 6.49 rad/sec

——— P, V Measurement ——— Heat Flux Sensor
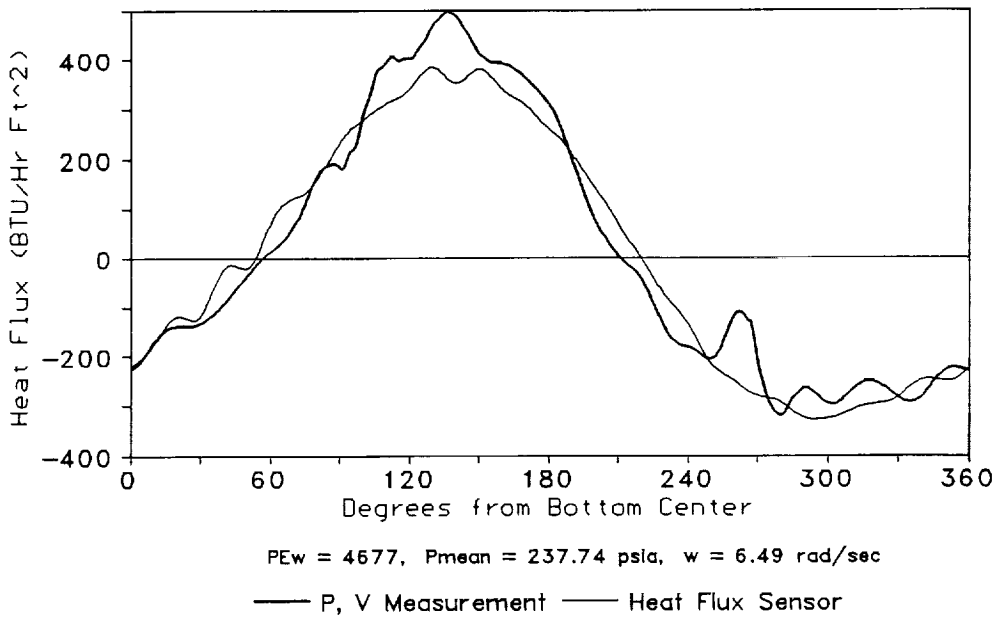
Figure 5.9 Measured Heat Flux, High Pressure and Low Frequency, Single Space.

PEw = 46098, Pmean = 242.37 psia, w = 62.63 rad/sec

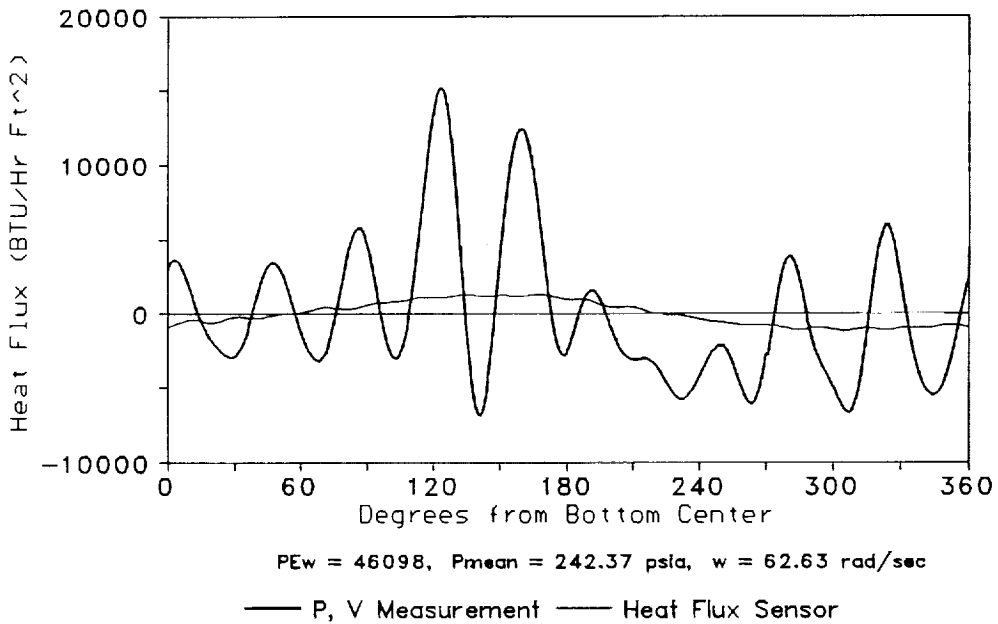——— P, V Measurement ——— Heat Flux Sensor

Figure 5.10   Measured Heat Flux, High Pressure and High Frequency, Single Space. Experiments.

5.6 Complex Nusselt Number

Heat flux and temperature data from the PV measurements were used to calculate complex Nusselt numbers which best predicted the heat flux data. Figure 5.11 shows the real and imaginary parts of the complex Nusselt number, while Figure 5.12 shows its magnitude. The noise in the calculated phase of Nu_c was too large to make a plot worthwhile.

The figures show the real and imaginary parts of Nu_c approximately equal. Those points (at high Pe_ω) for which the real-imaginary difference is large are the same points for which the heat transfer data shows high noise levels. The magnitude of Nu_c increases with Pe_ω, approximately in proportion to $Pe_\omega^{1/2}$.

Kornhauser and Smith (1988) measured heat flux and calculated the complex Nusselt number for different cylinder geometries and with different working fluids. They found that Lee's (1983) model explained the variations in Nu_c with speed, mean pressure, and cylinder geometry. The model did not, however, explain the variation of Nu_c with volume ratio. Kornhauser and Smith's experimental results showed Nu_c at $r_v=2$ matching Lee's predictions fairly well, but Nu_c at $r_v=4$ and 8 considerably higher than Lee's prediction. Since Lee's model was based on $r_v\to1$, Kornhauser and Smith postulated that the Lee's model would be satisfactory over the range $1\le r_v\le2$.

Figure 5.13 and 5.14 show that this postulate was correct. The figures plot the older results at volume ratios 2, 4, and 8 with the new results at volume ratio 1.1. The $r_v=1.1$ results closely match those at $r_v=2$.

Figure 5.15 compares the PV-measured heat flux for one run with that predicted using the measured temperature data and a constant complex Nusselt number.
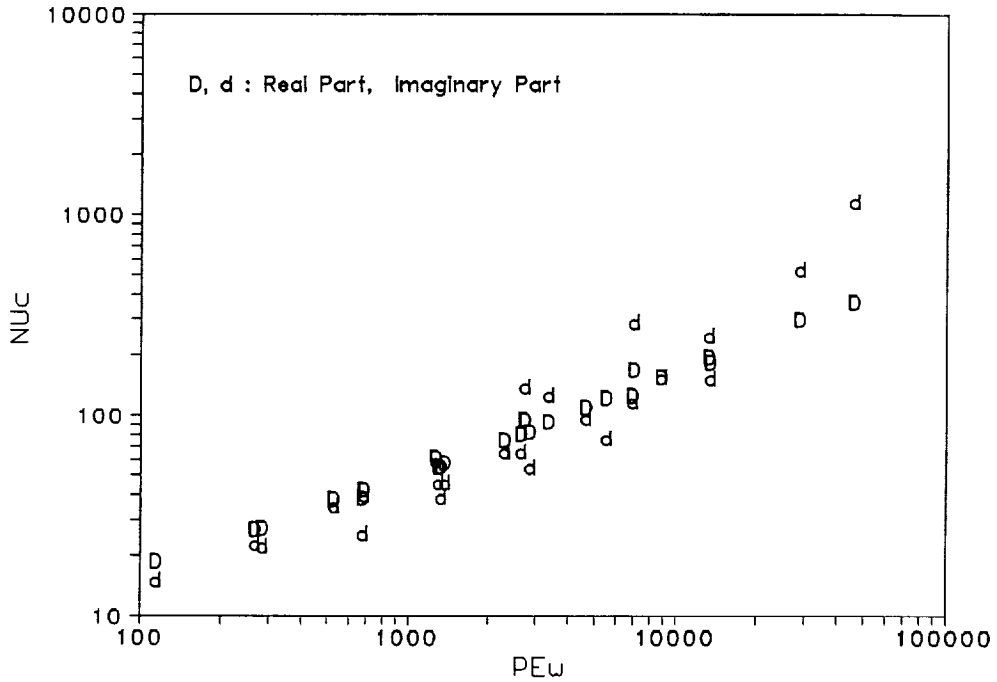
Figure 5.11 Real and Imaginary Parts Complex Nusselt Number vs. Oscillation Peclet Number, Single Space Experiments.

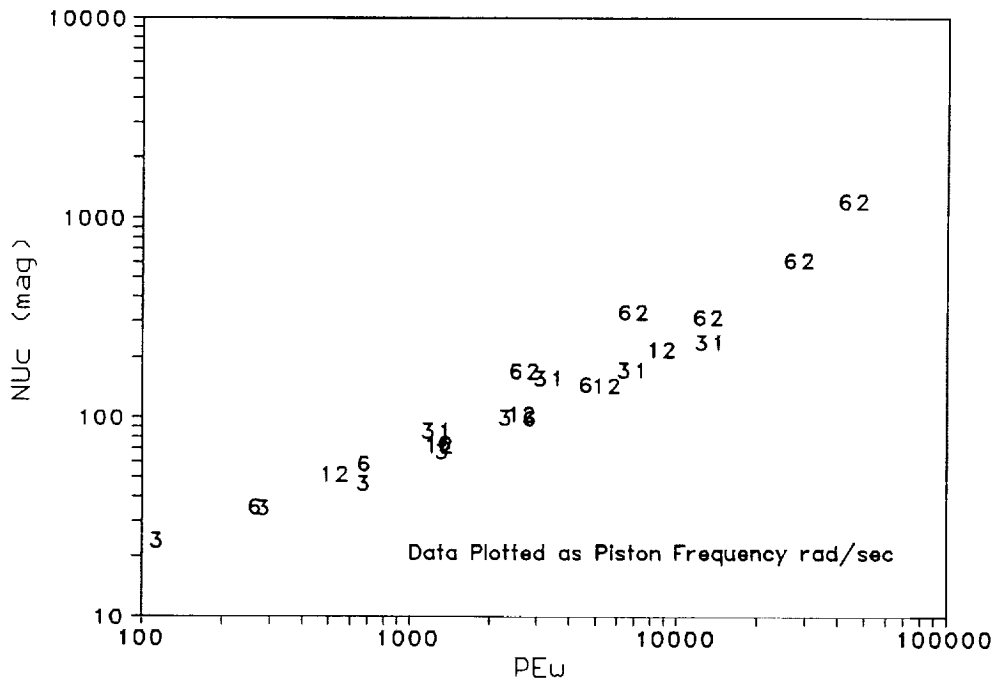Figure 5.12 Magnitude Complex Nusselt Number vs. Oscillation Peclet Number, Single Space Experiments.
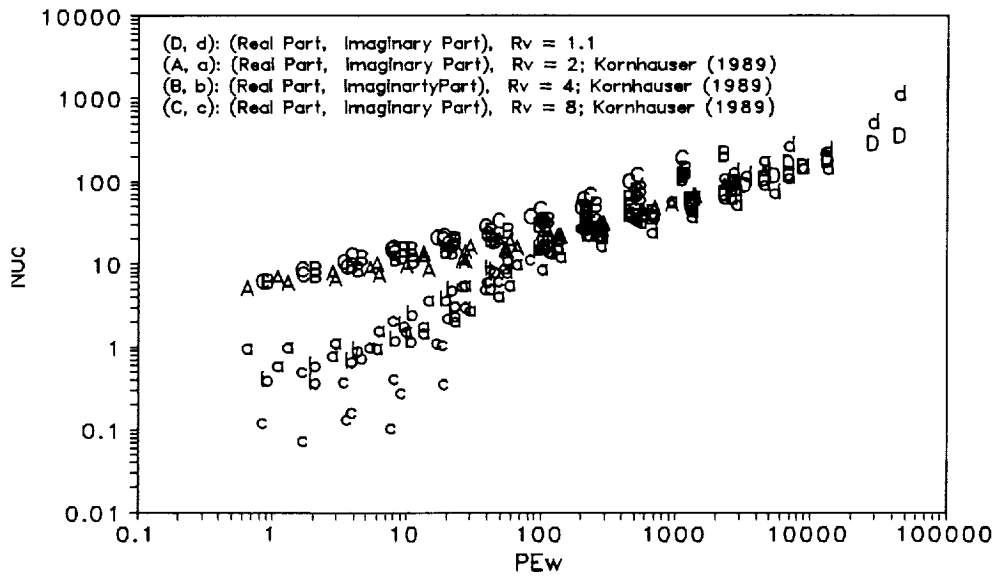
Figure 5.13 Real and Imaginary Parts Complex Nusselt Number vs. Oscillation Peclet Number, Single Space, Volume Ratio 1.1 (Current Results), 2, 4, and 8 (Previous Results).
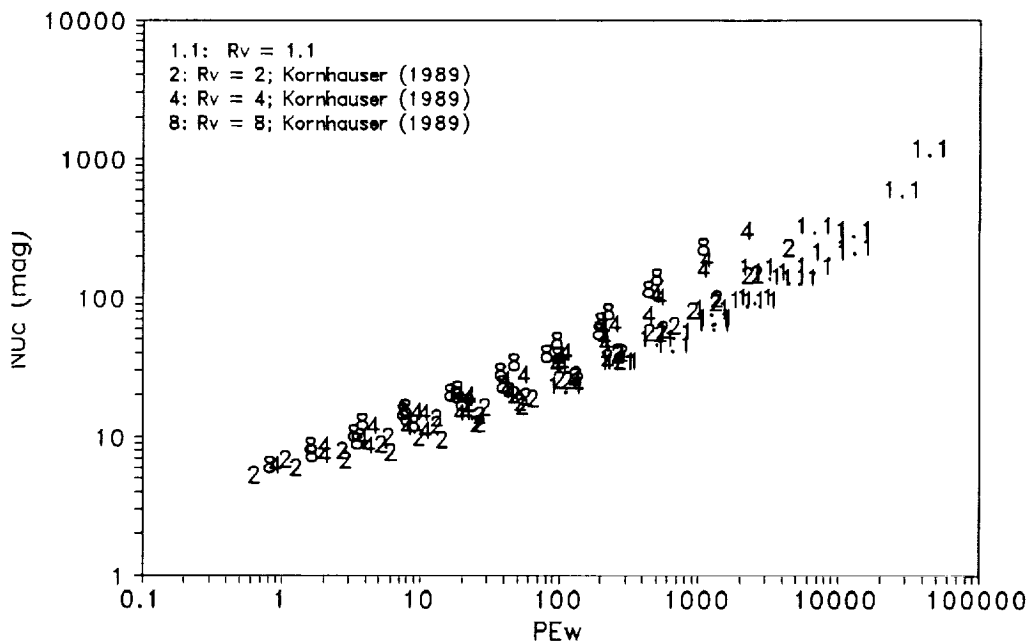
Figure 5.14 Magnitude Complex Nusselt Number vs. Oscillation Peclet Number, Single Space, Volume Ratio 1.1 (Current Results), 2, 4, and 8 (Previous Results).
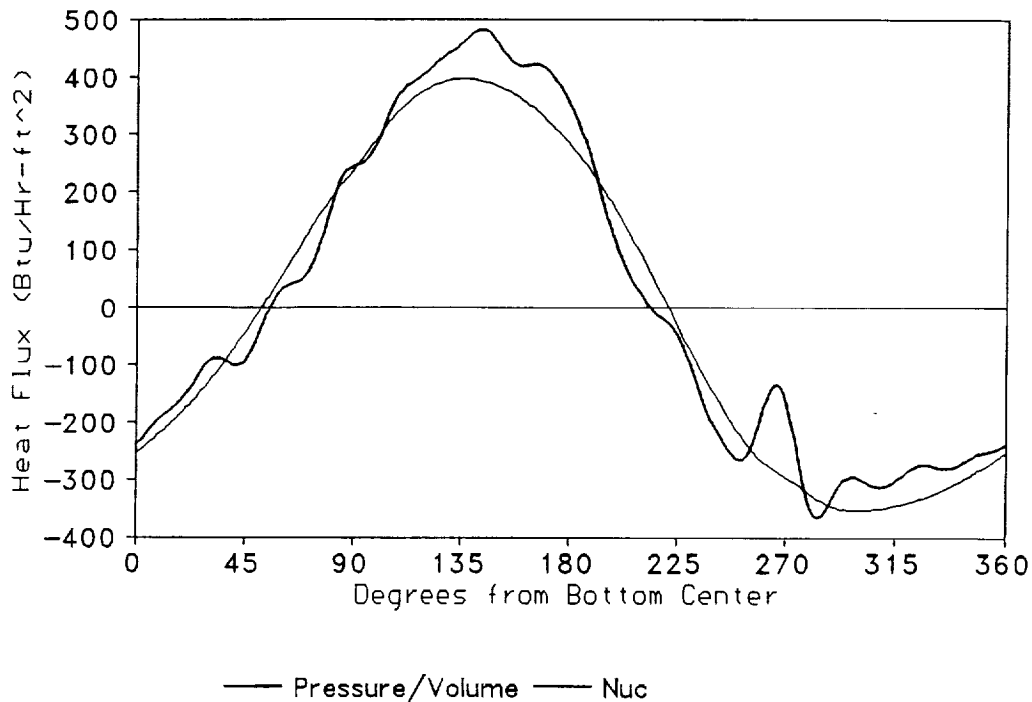
Figure 5.15 Measured and Predicted Heat Flux vs. Crank Angle, Single Space Experiment

5.7 Comparison to Model

Kornhauser and Smith (1992) showed that Lee's (1983) model predicted gas spring loss for volume ratio 2.0, but underpredicted loss for volume ratios 4.0 and 8.0. Figure 5.16 presents their loss results at $r_v = 2$, 4, and 8 together with the new single space loss results at $r_v = 1.1$ and the prediction of Lee's model. Lee's prediction matches both the $r_v = 1.1$ and 2 measurements, but underpredicts the $r_v = 4$ and 8 measurements.

It may thus be stated that Lee's model is accurate, without empirical correctio factors, over the range $1 < r_v < 2$, and may be accurate for r_v somewhat higher than 2. It is clearly inaccurate at $r_v = 4$, as well as in some lower Pe_ω ranges where the $Loss_{nd}$-Pe_ω correlation breaks down (Kornhauser and Smith, 1992).

Figure 5.16   Nondimensional Loss vs. Oscillation Peclet Number, One Space, $r_v = 1.1$; Kornhauser and Smith (1992) $r_v = 2$, 4, and 8; and Lee (1983) Model.

6 Lumped Two Space Results

6.1 Pressure Drop across the Orifice

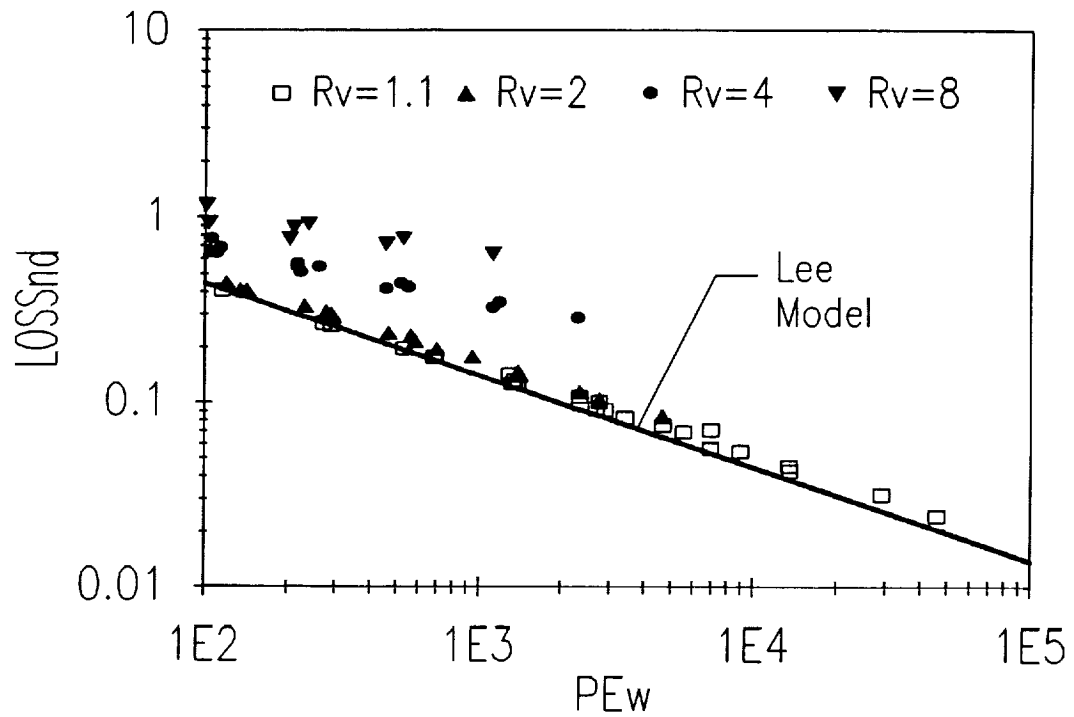The pressure drop across the orifice was measured by taking the difference between the signals of the two pressure transducers, one in the fixed volume space (in the head) and one in the varying volume space (in the side wall just below the orifice plate). The pressure difference was then smoothed by Fourier decomposing, discarding high frequency components, and recombining. The pressure drop was then defined as the maximum difference of this smoothed measurement.

Figure 6.1 shows measured maximum pressure drop for a number of two space experiments. At high speed, the pressure drop appears to be proportional to Pe_{ω}^2, while at low speed it appears to be nearly constant. Pressure drop increases with increasing cyclic mean pressure.

Based on steady, incompressible flow through an orifice, one expects pressure drop to be proportional to $v^2\rho$, which is in turn (for this experiment) proportional to $\omega^2 P_0$. It thus appears reasonable to nondimensionalize pressure drop as $\Delta P/P_0$. This nondimensional pressure drop data is plotted against frequency in Figure 6.2. At high frequencies, the nondimensionalization works and the nondimensional ΔP has the expected ω^2 proportionality. At low frequencies the nondimensionalization works for most of the data, but the nondimensional ΔP is almost constant in ω.

The orifice pressure drop at high frequencies is thus explained by simple fluid mechanics arguments. That at low frequencies, however, is not. At very low velocities, one would expect the pressure drop to be approximated by Stokes flow, i.e. $\Delta P \propto v$ and independent of ρ. That is obviously not the case here. Pressure transducer inaccuracy at low ΔP does not explain the results, either: it might explain why the data at $P_0 = 1$ bar and 2 bar does not correlate at low frequency, but it wouldn't explain why the other data does.

6.2 Nondimensional Loss

One and two space nondimensional loss results, uncorrected for ΔP loss, are shown in Figure 6.3. The two space losses do not match the one space losses and do not correlate with one another.

One and two space nondimensional loss results, with the two space losses corrected to eliminate ΔP losses, are shown in Figure 6.4. While the one and two space losses still do not match, the two space losses are now correlated with one another. The $Loss_{nd}$ based on Lee's (1983) in-cylinder heat transfer model is evidently useful even with inflow-produced turbulence.

One question that arises is whether the difference in non-dimensional loss between the one space and two space experiments might be due to the difference in volume ratio. (The one space experiments were at volume ratio 1.1, while the two space experiments were at 1.2.) Kornhauser and Smith (1992) showed that the $Loss_{nd}$ in a single space apparatus increased as
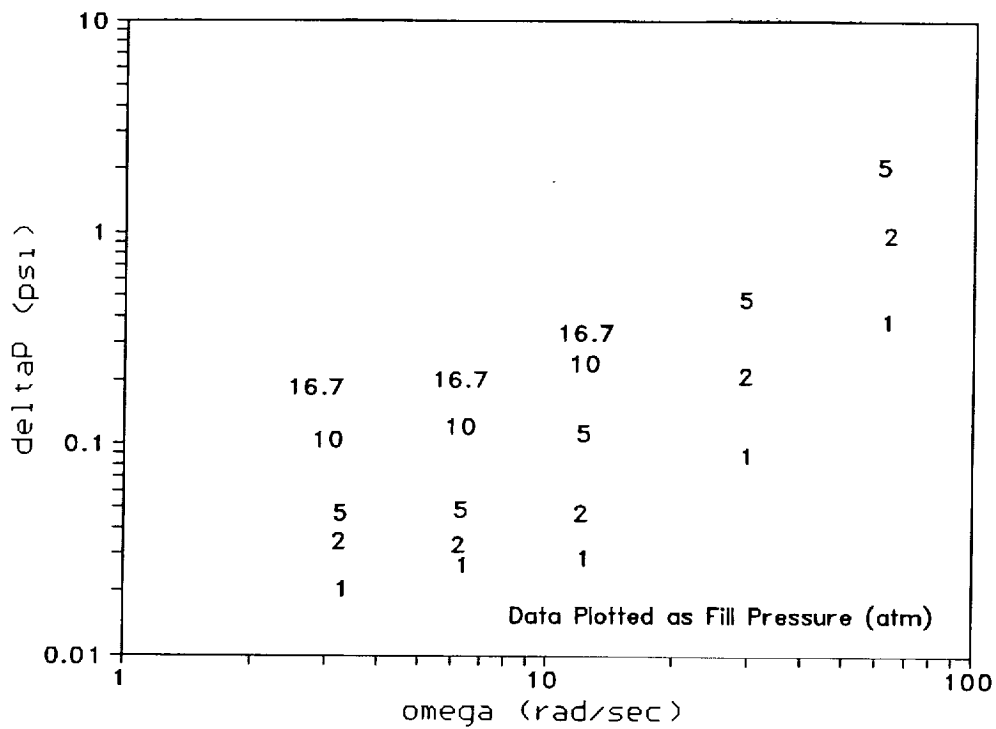
Figure 6.1 Maximum Pressure Drop vs. Angular Frequency, Two Space Experiments.
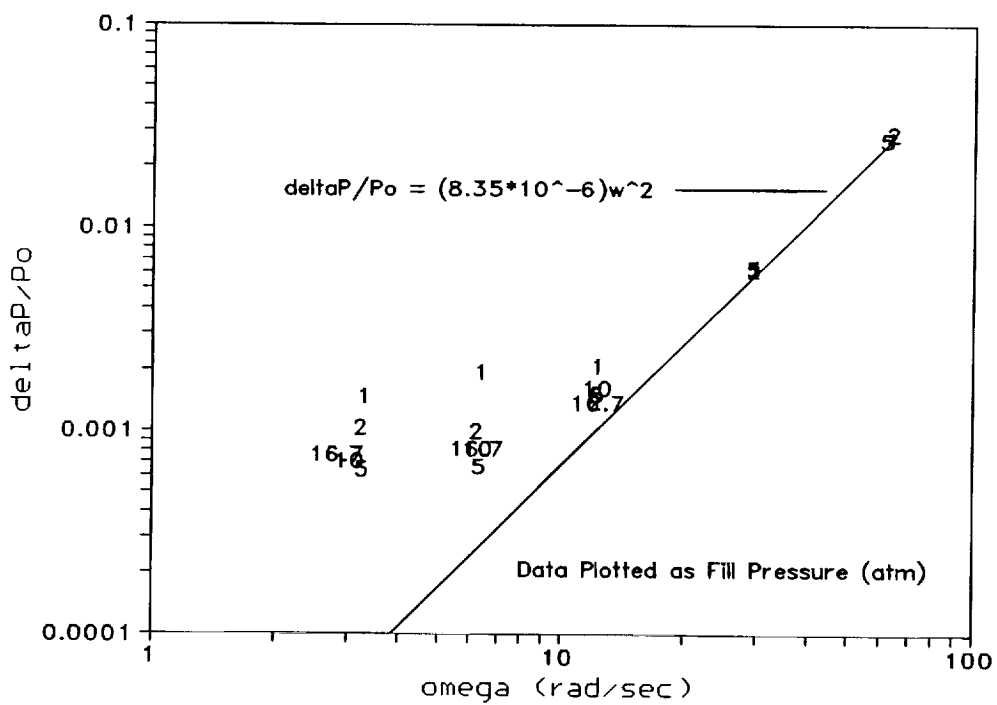

Figure 6.2   Nondimensional Maximum Pressure Drop vs. Angular Frequency, Two Space Experiment.
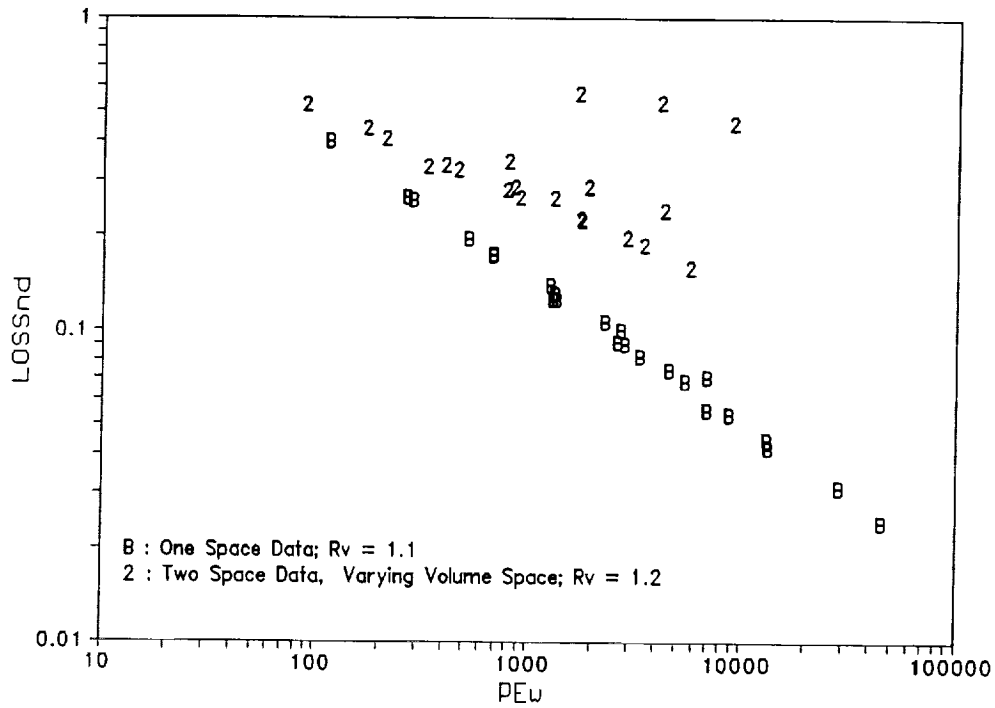
Figure 6.3 Total Nondimensional Loss (including ΔP Loss) vs. Oscillation Peclet Number, Single and Two Space Experiments.
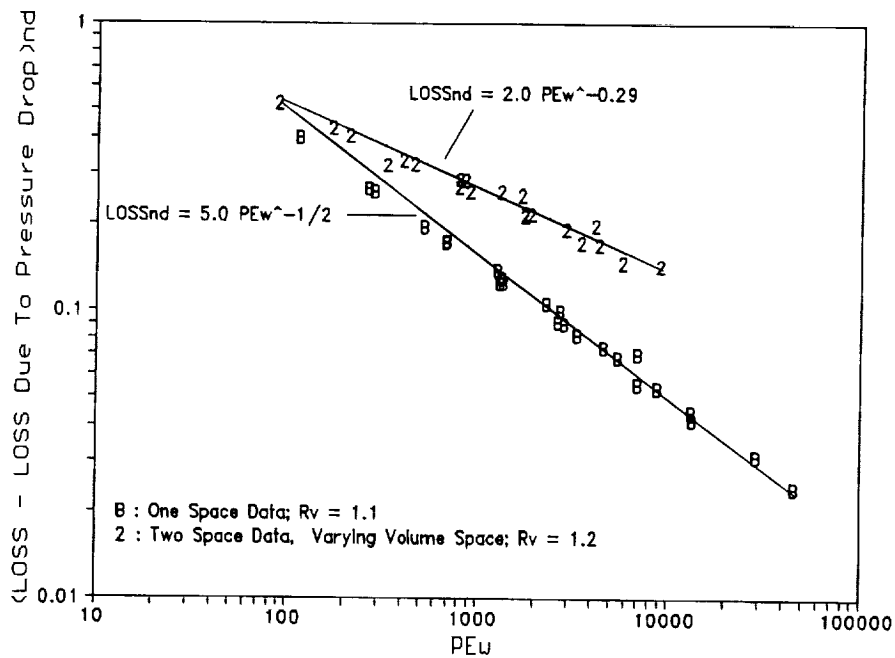

Figure 6.4 Corrected Nondimensional Loss (without ΔP Loss) vs. Oscillation Peclet Number, Single and Two Space Experiments.

volume ratio increased from 2 to 8; the comparison of their data with the one space data (Figure 5.6) shows that the single space data from $r_v = 1.1$ closely matches that from $r_v = 2$. It is thus clear that the effect shown in Figure 6.4 is not due to variation in volume ratio.

Since volume ratio is not the cause, it is evident that heat transfer-related loss is increased by the presence of the orifice. This shows that the predictions of the Gedeon (1989) and Pfriem-Kornhauser (Kornhauser, 1992) models may be correct. This topic is discussed more fully later in this section.

6.3 Heat Flux Measurements

Two sets of data were taken in the same two space geometry. The experiments differed in two ways:

- In the first data set, the slack in the piston drive linkage resulted in additional noise in the *PV* heat flux calculation; in the second set, this slack was eliminated by keeping the linkage in tension at all times.
- In the first data set, the heat flux sensor was located in the head of the fixed volume space; in the second set, it was located on the sidewall of the varying volume space. (The original plan was to have a sensor in each space, but the failure of one sensor required that a single sensor be moved from space to space.)

Both *PV*- and sensor-measured heat flux from both sets of data will be presented here.

Figures 6.5 and 6.6 present heat flux data from two low pressure, low speed runs at almost identical conditions. The heat flux measured from *PV* data is almost identical for the two runs, but the sensor-measured heat flux is considerably different: that measured in the fixed volume space is an order of magnitude larger than that measured in the varying volume space. This difference may stem from one or both of two possible sources:

- The heat flux in the fixed volume space may be much larger. Since Pe_ω in the fixed volume space is larger, the magnitude of Nu_c might be expected to be larger.
- The fixed volume space sensor is near the middle of the head, fully exposed to fluid flow. The varying volume space sensor is in the corner between the orifice plate and the wall, somewhat shielded from flow. Turbulent enhancement of heat transfer might therefore be larger for the sensor in the fixed volume space.

Another notable point is that the sensor in the fixed volume space shows large heat transfer fluctuations that do not follow the mixed mean pressure. These are very likely due to turbulence.

Figures 6.7 and 6.8 present heat flux data from two high pressure, low speed runs at almost identical conditions. As for the previous case, the heat flux measured from *PV* data is very similar for the two runs, but the sensor-measured heat flux is considerably larger in the varying volume space. All the heat fluxes are higher than they were at lower Pe_ω as would be expected.

Figures 6.9 and 6.10 present heat flux data from two high pressure, high speed runs at almost identical conditions. The trends noted in the previous four figures still hold. Two other interesting phenomena may be observed:

——— Pressure/Volume ——— Sensor

Figure 6.5 Two Space Heat Flux vs. Crank Angle. Lumped Pressure-Volume Flux and Sensor in Fixed Volume Space. $Pe_\omega = 166$, $P_{mean} = 13.89$ psia, $\omega = 6.43$ rad/s.

——— Pressure/Volume ——— Sensor

Figure 6.6 Two Space Heat Flux vs. Crank Angle. Lumped Pressure-Volume Flux and Sensor in Varying Volume Space. $Pe_\omega = 162$, $P_{mean} = 14.47$ psia, $\omega = 5.85$ rad/s.

Figure 6.7 Two Space Heat Flux vs. Crank Angle. Lumped Pressure-Volume Flux and Sensor in Fixed Volume Space. Pe_ω=899, P_{mean}=73.73 psia, ω=6.40 rad/s.

Figure 6.8 Two Space Heat Flux vs. Crank Angle. Lumped Pressure-Volume Flux and Sensor in Varying Volume Space. Pe_ω=955, P_{mean}=74.11 psia, ω=6.74 rad/s.
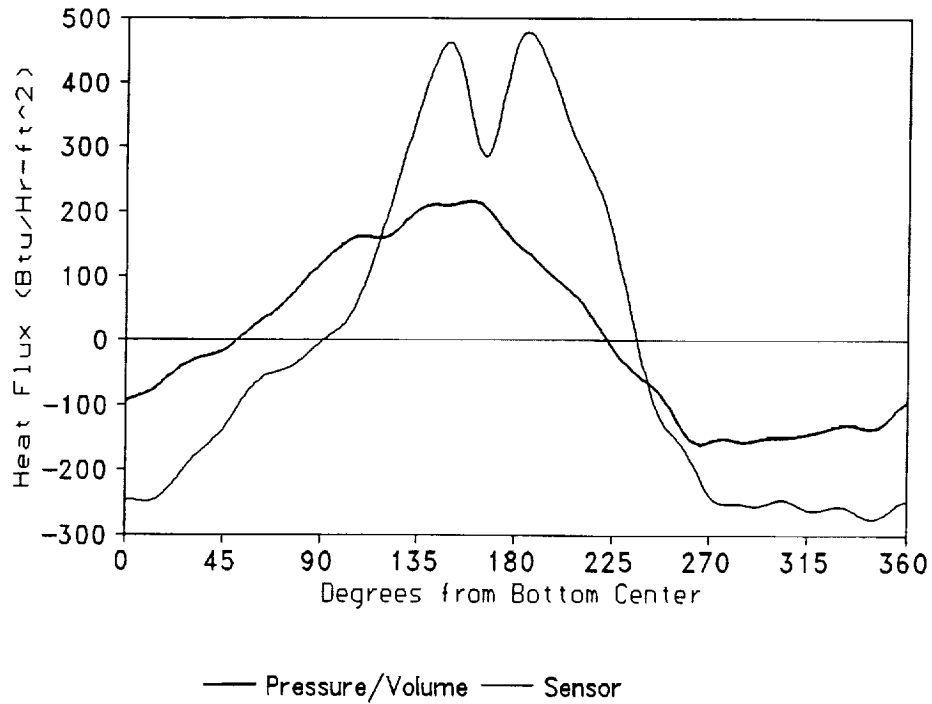
6-6

Figure 6.9 Two Space Heat Flux vs. Crank Angle. Lumped Pressure-Volume Flux and Sensor in Fixed Volume Space. $Pe_\omega=4540$, $P_{mean}=76.93$ psia, $\omega=29.89$ rad/s.
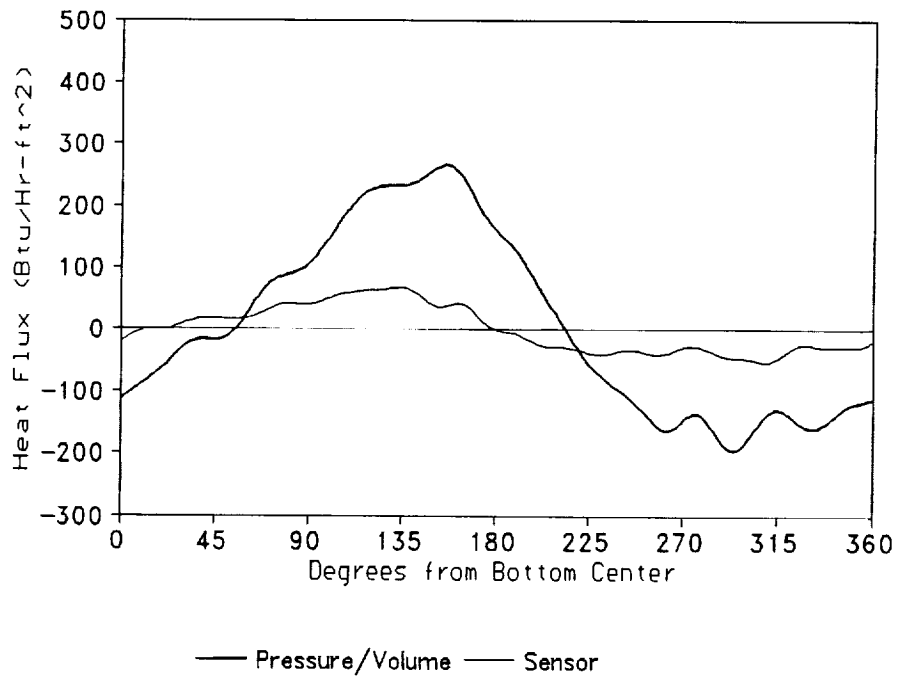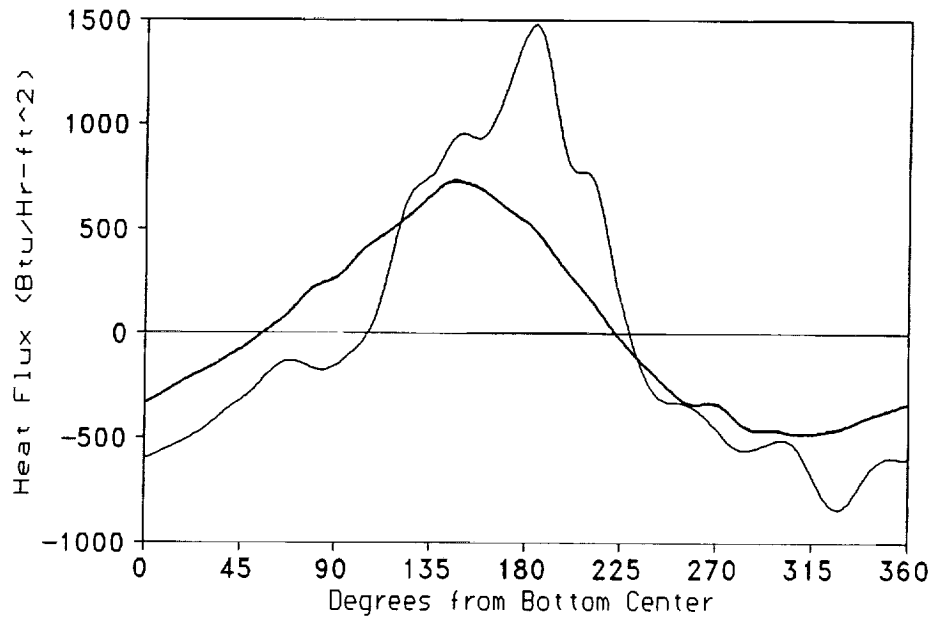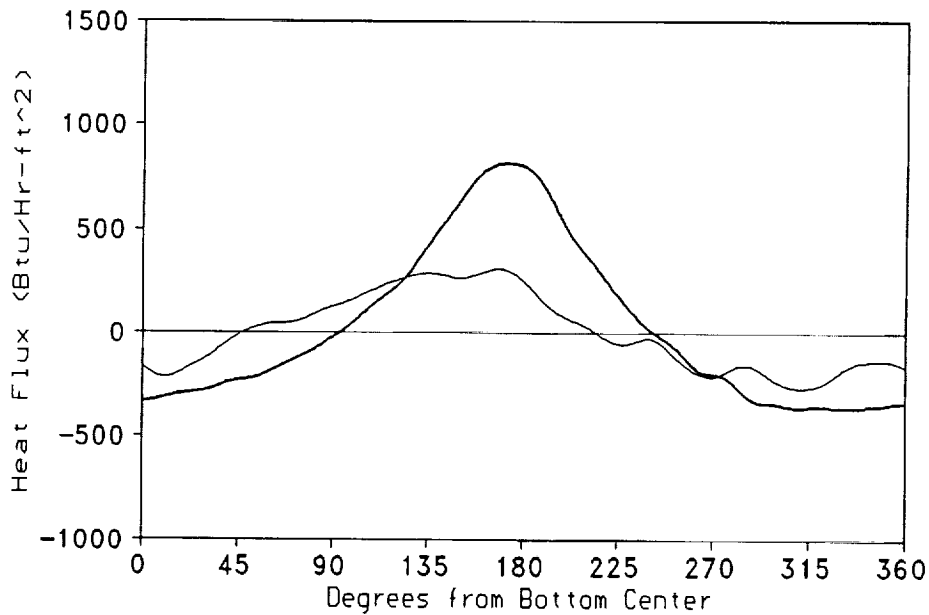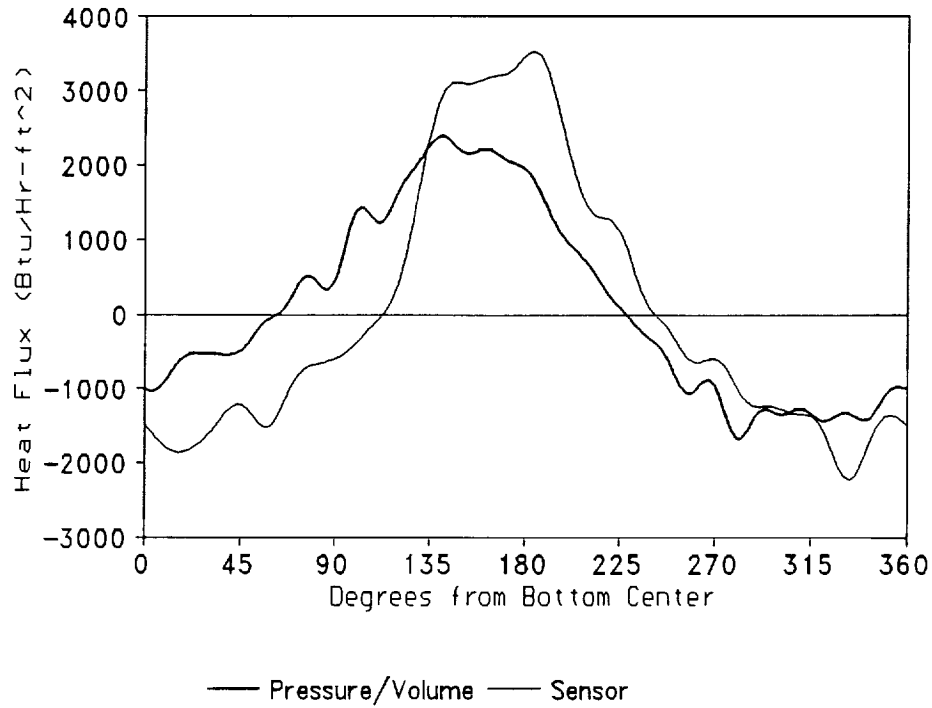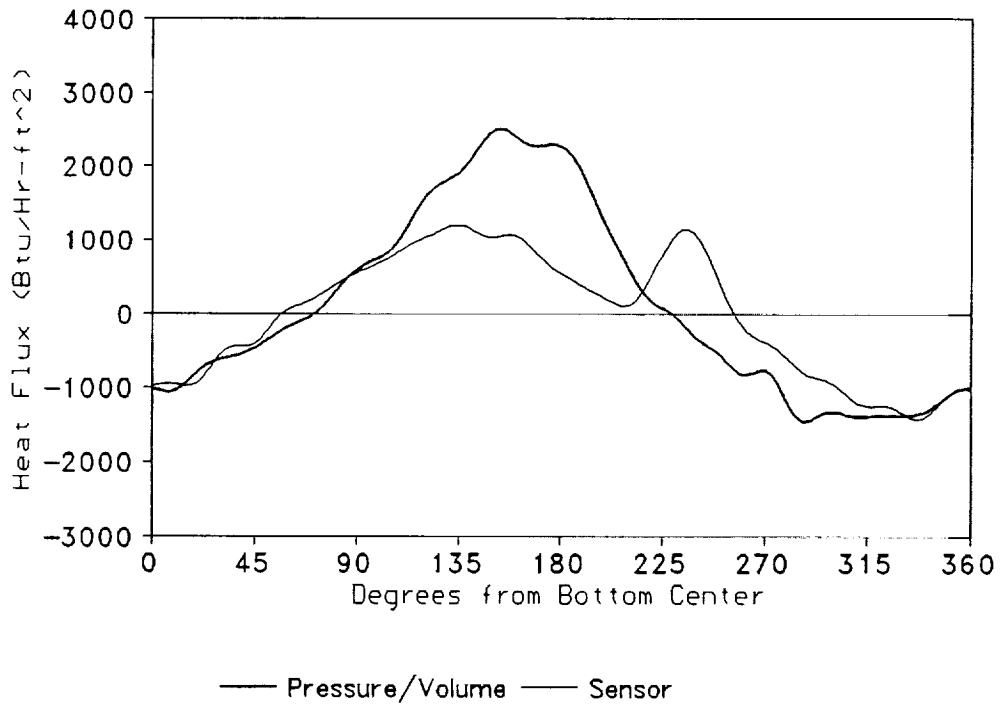

Figure 6.10 Two Space Heat Flux vs. Crank Angle, Lumped Pressure-Volume Flux and Sensor in Varying Volume Space. $Pe_\omega=4545$, $P_{mean}=75.55$ psia, $\omega=31.56$ rad/s.

- The *PV* measured heat flux on 6.10 is less noisy than that on 6.9 due to the smoother volume signal.
- The heat flux measured by the sensor in the varying volume space shows a large peak approximately 60° after top center. Other high-Pe_ω runs show similar peaks. This may be an indication that the heat transfer enhancement due to inflow-produced turbulence is not uniform over the cycle, but is much larger during the intake stroke.

All the heat flux plots except the sensor trace in Figure 6.10 lead the temperature difference (which is maximum near top and bottom center) by considerable amounts. The peak after top center in the 6.10 sensor trace lags the temperature difference.

6.4 Complex Nusselt Number

The real and imaginary parts of the complex Nusselt number for the lumped two space data are plotted in Figure 6.11. The magnitude of the complex Nusselt number is plotted in Figure 6.12. For comparison, the values from the single space experiments are included on both of these plots.

The results of the single and two space experiments are similar in that for each set of them the real and imaginary parts of Nu_c are approximately equal and they and the magnitude of Nu_c appear to have a power law relationship with Pe_ω. They differ in that the values of Nu_c are uniformly higher for the two space experiment, with the difference increasing as Pe_ω increases.

One question that arises is whether the difference in complex Nusselt number between the one space and two space experiments might be due to the difference in volume ratio. (The one space experiments were at volume ratio 1.1, while the two space experiments were at 1.2.) Kornhauser and Smith (1992) showed that Nu_c in a single space apparatus increased as volume ratio increased from 2 to 8; the comparison of their data with the one space data (Figures 5.13 and 5.14) shows that the single space data from $r_v = 1.1$ closely matches that from $r_v = 2$. It is thus clear that the effect shown in Figure 6.11 and 6.12 is not due to variation in volume ratio.

Since volume ratio is not the cause, it is evident that the magnitude of the complex Nusselt number is increased by the presence of the orifice. This shows that the predictions of the Gedeon (1989) and Pfriem-Kornhauser (Kornhauser, 1992) models may be correct. This topic is discussed more fully later in this section.

The *PV* measured heat flux for a two space run is compared with the prediction from the fitted complex Nusselt number in Figure 6.13.

6.5 Comparison to Model

The predictions of the Pfriem-Kornhauser (Kornhauser, 1992) model for in-cylinder heat transfer with inflow-produced turbulence will be examined here.
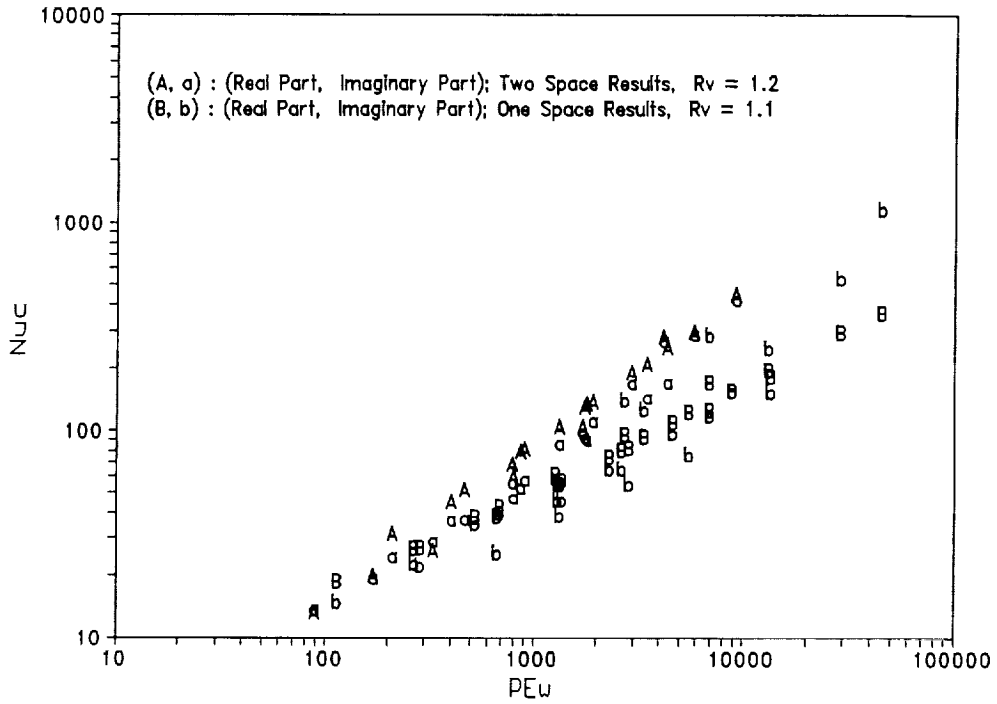
Figure 6.11 Real and Imaginary Parts of Complex Nusselt Number vs. Oscillation Peclet Number, Single and Two Space Experiments.
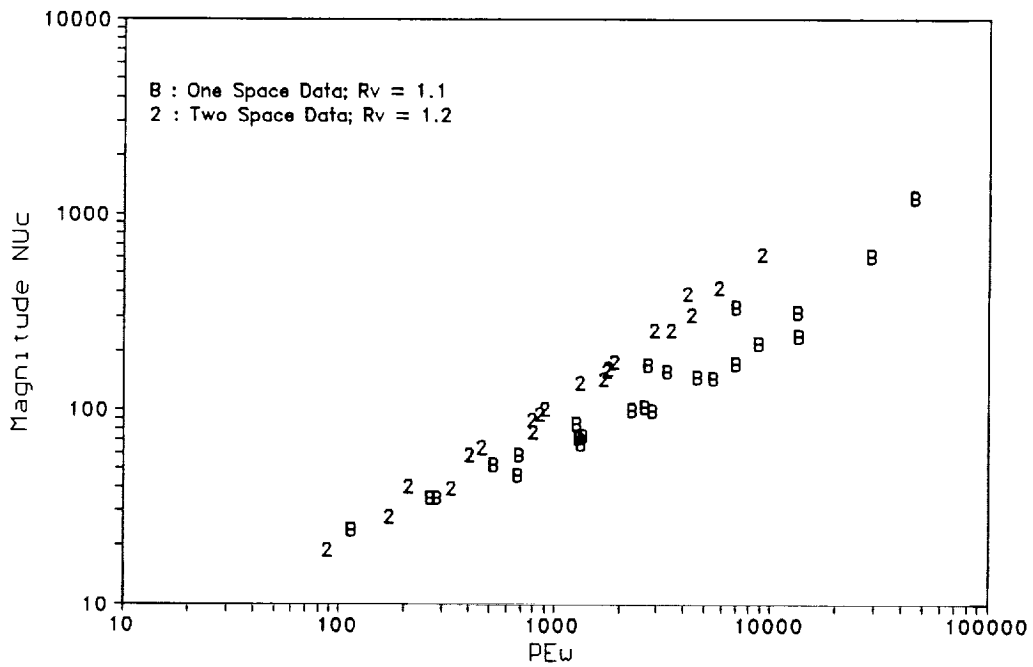
Figure 6.12 Magnitude of Complex Nusselt Number vs. Oscillation Peclet Number, Single and Two Space Experiments

The Pfriem-Kornhauser model attempted to predict the variation of complex Nusselt number with inflow-produced turbulence. The model was directed toward calculating Nu_c for a single space based on the Re_{in} and Pe_ω for that space only. In the lumped two-space data Nu_c based on the surface-average heat transfer and mass-average temperature for the two spaces is compared to the Re_{in} and Pe_ω based on the combined hydraulic diameter of the two spaces. Figure 6.14 compares the one- and two-space Nu_c magnitude results with the predictions of the Pfriem-Kornhauser model. It also presents the predictions of a version of the modified by changing the empirical parameters, which in the original model were based on steady flow turbulence.

The figure shows that for the one space experiments (laminar case, no inflow-produced turbulence) the model predictions match the data fairly well. Those data for which the match is least close are those for which the correlation shows the greatest scatter and for which the experimental heat flux plots show the greatest noise. The laminar case is equivalent to Pfriem's (1943) model without modification, and its Nu_c predictions are very close to those of Lee's (1983) model.

For the two space experiments the model overpredicts the complex Nusselt number. The constants in the model's expression relating δ/D_h to Re_{in} are, however, empirical: based on the heat transfer to the downstream surface of a cylinder in steady crossflow. By modifying these coefficients slightly, the model can be made to match the two space data.

It should be noted that the use of Pe_ω based on the total hydraulic diameter of the two spaces may not be appropriate. Just as the Nu_c is based on averaged heat transfer and temperature values for the two spaces, it may be appropriate to base Pe_ω on some average D_h. It is not clear, however, whether D_h should be averaged based on volume, on surface area, or on something else. The effect of a different averaging would be to offset the experimental data in the Pe_ω direction. This offset would probably require different constants in the δ/D_h expression of the model.

The phase data from the lumped two space experiment was too scattered to warrant comparison with the model. Besides this, it appears likely that there is less validity in averaging the phase of the heat transfer in the two spaces than in averaging its magnitude.

Because of the uncertainties involved in lumping the two spaces together, because of the lack of a phase comparison, and because data is available at only one Re_{in}/Pe_ω, no definitive statement can be made about the accuracy of the Pfriem-Kornhauser model. It appears, however, that the trends in the magnitude of Nu_c predicted by the model are qualitatively correct.
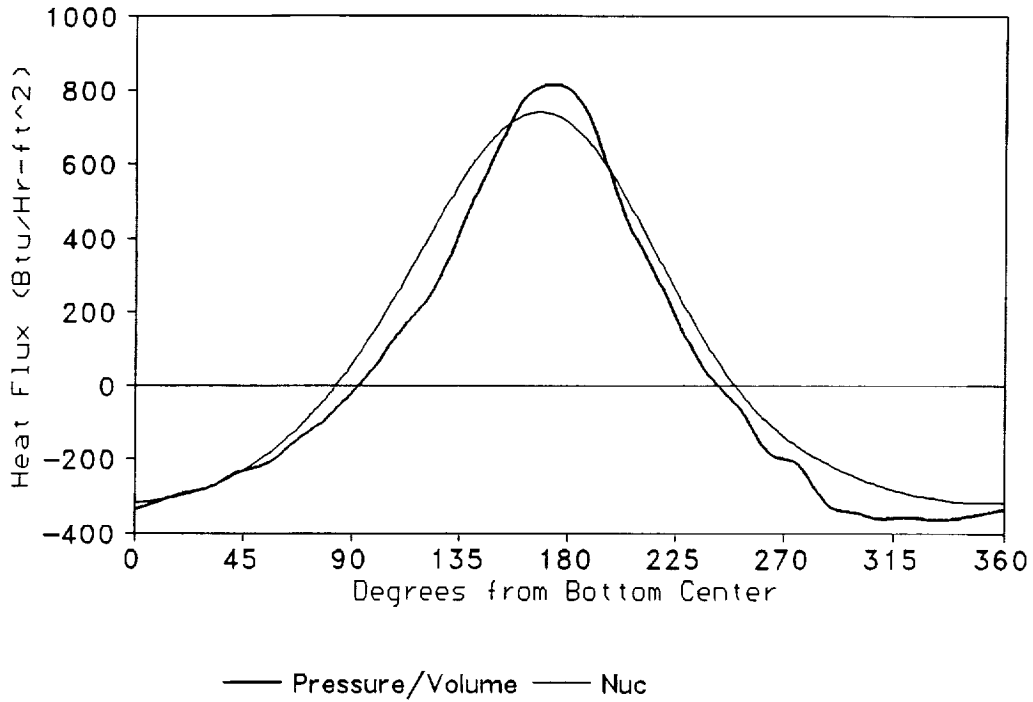
Figure 6.13 Measured and Predicted Heat Flux vs. Crank Angle, Two Space.
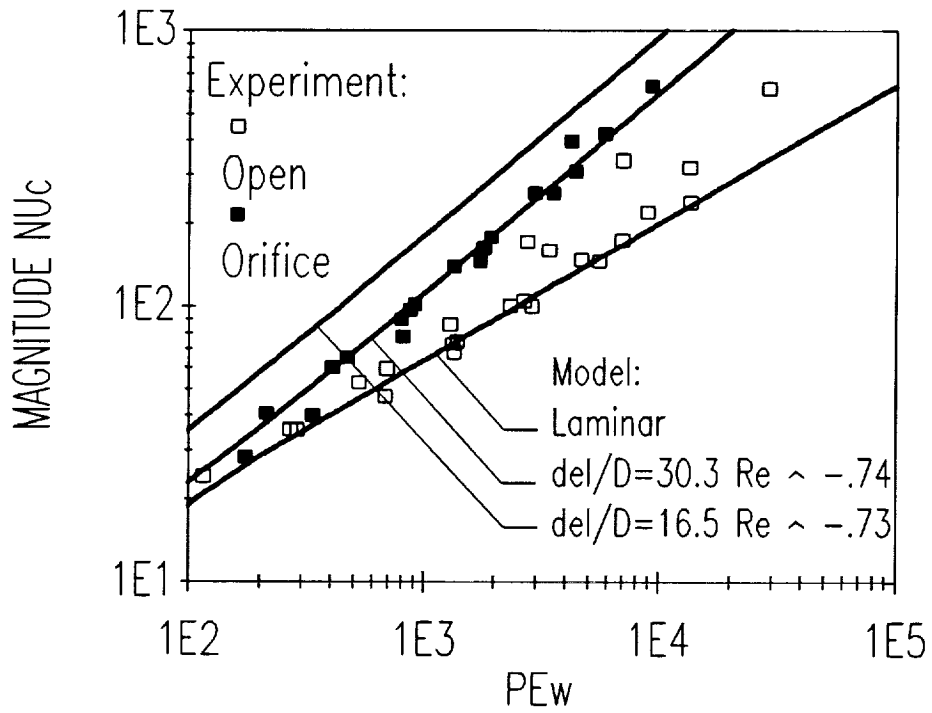
Figure 6.14 Magnitude Complex Nusselt Number vs. Oscillation Peclet Number, One Space and Lumped Two Space Experiment and Pfriem-Kornhauser Model.

7. Two Space Results

The two space data analysis technique, described in Section 4, was applied to a few of the two space experimental data sets. Because of the ambiguous results, the technique has not yet been applied to the entire experimental data base.

7.1 Optimization of Total Mass

As described in Section 3, there was some leakage in the apparatus. Although this leakage was negligible during the data collection period, it was not negligible over the time for the experiment to accelerate and reach cyclic steady state.

In the single space and lumped two space data analysis, the total mass in the cylinder was corrected by comparing the time- and mass- averaged temperature obtained by using the working fluid as a gas thermometer with the time-averaged temperature measured by a center gas thermocouple. While this procedure was adequately accurate for those analyses, it wasn't for the coefficient optimization technique. The error in the total mass put an offset on all the pressure measurements that was large relative to the residual pressure errors of the optimization.

In order to remedy this problem, total mass was added to the list of coefficients optimized. The mass optimization, like that for the heat transfer and orifice flow coefficients, was tested with simulated data. When an incorrect guess for total mass was used, the optimized total mass would always converge on the correct mass. The total mass convergence was very little effected by simulated noise.

7.2 Results of Optimization on Experimental Data

The coefficient optimization procedure was tested on many two space runs. The results of tests on three runs will be presented here:

Medium Speed, Medium Mean Pressure	(2 Hz, 5 atm)
High Speed, Medium Mean Pressure	(5 Hz, 5 atm)
High Speed, Low Mean Pressure	(10 Hz, 1 atm)

The results will be described briefly in this section and discussed more fully in Section 7.3.

Medium Speed, Medium Pressure (2 Hz, 5 atm)

Converged results for a two space run at 2 Hz, 5 atm mean pressure are shown in Table 7.1. The results are for various initial guesses for the h's; all the k guesses were 5.0. For most of the cases k_2 was constrained by a minimum value of 2.0, while for one case it was constrained by a minimum value of 0.1. Several facts are evident from the table:

- The converged values of the coefficients are dependent on the initial guesses.

Table 7.1 Converged Coefficients, Experimental Data: 2 Hz, 5 atm
(h's in kW/m²K. Initial guess for k's=5. k_2 constrained $\geq$ 2 , $\geq$ 0.1 in case f)

Case	h's guess	Pressure Resid, %	hrv	hiv	hrf	hif	k1	k2
a	.5	.24810	.0026	.84	.18	.000032	3.6	2.00
b	.3	.20210	.056	.67	.17	.000002	5.0	4.98
c	.1	.07311	.055	.18	.15	.000005	4.85	2.99
d	.05	.07209	.00041	.17	.17	.000034	4.50	2.00
e	.05	.07176	.000073	.17	.17	.000026	4.33	0.10
f	.03	.07214	.000011	.16	.17	.000029	4.16	2.00

Figure 7.1 Measured and Predicted Differential Pressure and Pressure Residual vs. Crank Angle from Mid-Expansion (2 Hz, 5 atm)

- In the varying volume space the imaginary part of the heat transfer coefficient is considerably larger than the real part; in the fixed space the reverse is true. If these results are correct, they indicate that the heat transfer leads the temperature difference by 90° in the varying space and by 0° in the fixed space.

- The values of k_1 are quite large, larger than would be expected based on typical values of steady orifice discharge coefficients.

- The value of k_2 often goes to the minimum value allowed by the imposed constraints.

Figure 7.1 shows the differential pressures and the pressure residuals from some of the optimized simulations listed in Table 7.1. It may be noted that

- The simulated differential pressure matches the experimental data well in magnitude, but leads it slightly.

- The pressure residuals in both cases shown do not consist merely of noise, but have considerable content.

High Speed, Medium Pressure (5 Hz, 5 atm)

Converged results for a two space run at 5 Hz, 5 atm mean pressure are shown in Table 7.2. The results are for various initial guesses for the h's; all the k guesses were 5.0. In all cases k_2 was constrained by a minimum value of 0.1. The same comments made about Table 7.1 apply to 7.2.

Figure 7.2 shows the differential pressures and the pressure residuals from some of the optimized simulations listed in Table 7.2. The differential pressure appears to be a better fit than in the 2 Hz, 5 atm data, but the residuals still have content.

High Speed, Low Pressure (10 Hz, 1 atm)

Converged results for a two space run at 10 Hz, 1 atm mean pressure are shown in Table 7.3. The results are for various initial guesses for the h's; all the k guesses were 5.0. In all cases k_2 was constrained by a minimum value of 0.1. The same comments made about Table 7.1 apply to 7.2.

Figure 7.3 shows the differential pressures and the pressure residuals from some of the optimized simulations listed in Table 7.3. The differential pressure appears to be a good fit and the residuals have no obvious content.

Table 7.2 Converged Coefficients, Experimental Data: 5 Hz, 5 atm
(h's in kW/m^{2}K. Initial guess for k's=5. k_2 constrained $\geq$ 0.1)

Case	h's guess	Pressure Resid,%	hrv	hiv	hrf	hif	k1	k2
a	.3	.100400	.0302	.703	.312	.000050	2.72	.1
b	.15	.054447	.0843	.328	.294	.000025	2.73	.1
c	.08	.058460	.0941	.148	.292	.0340	2.73	.1
d	.04	.054091	.000328	.301	.312	.000387	2 .70	.1
e	.02	.055715	.000017	.248	.317	.0150	2.68	.1

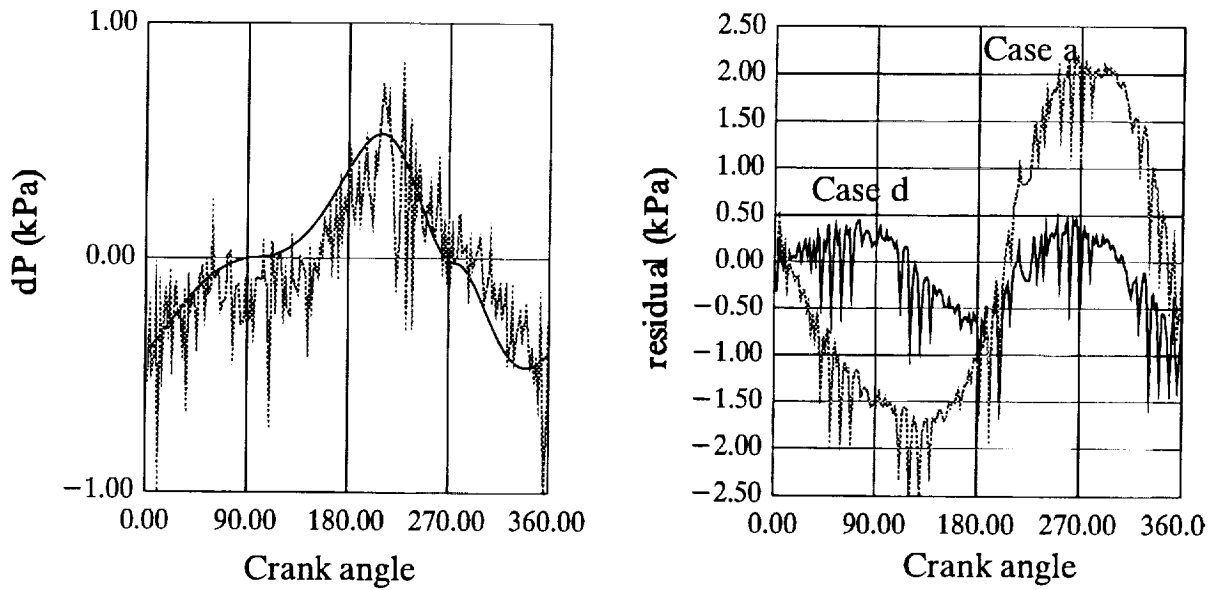
Figure 7.2 Measured and Predicted Differential Pressure and Pressure Residual vs. Crank Angle from Mid-Expansion (5 Hz, 5 atm)

Table 7.3 Converged Coefficients, Experimental Data: 10 Hz, 1 atm
(h's in kW/m²K. Initial guess for k's=5. k_2 constrained ≥ 0.1)

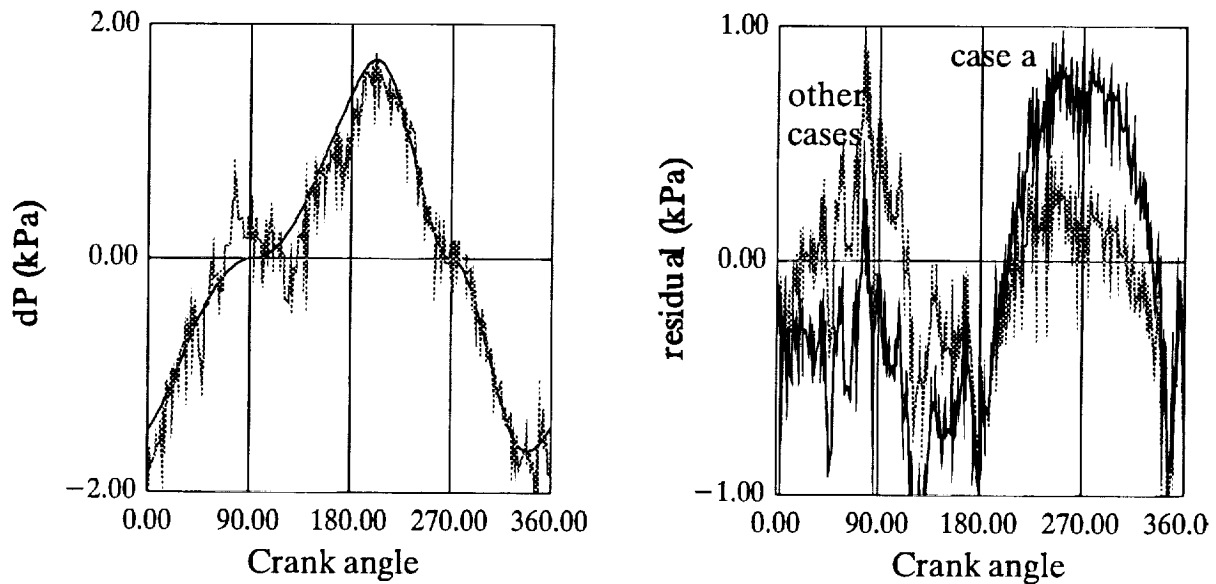| Case	h's	Resid,%	hr1	hi1	hr2	hi2	k1	k2
a	.2	.15917	.000045	.224	.186	.0369	2.46	.1
b	.15	.15975	.000906	.202	.189	.0449	2.45	.1
c	.1	.15971	.000086	.134	.190	.0554	2.43	.1
d	.04	.16049	.00111	.0826	.190	.0709	2.43	.1
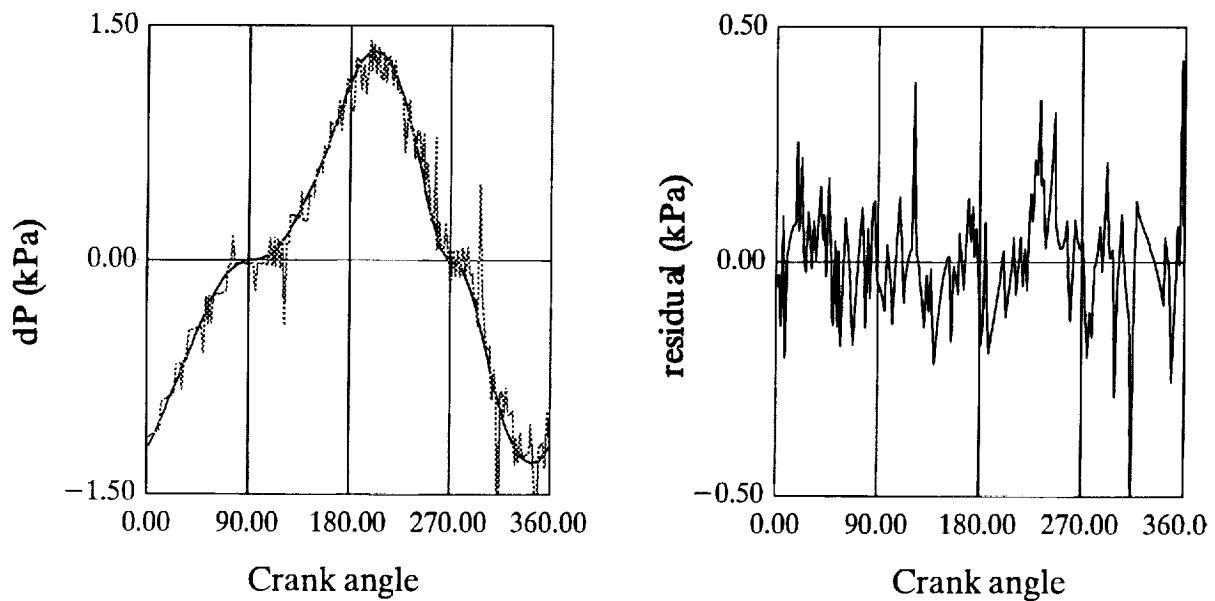
Figure 7.3 Measured and Predicted Differential Pressure and Pressure Residual vs. Crank Angle from Mid-Expansion (10 Hz, 1 atm)

7.3 Discussion of Results with Experimental Data

There is clearly a problem with the coefficient optimization procedure, since the converged results are dependent on the initial guesses. Furthermore, many of those converged results do not make sense:

- The 90° heat transfer phase shift seen in the variable volume space has not been seen in other experimentation, or predicted by any analyses.

- The lack of any phase shift in the fixed volume space appears to contradict the results from the lumped two space data. That data showed phase shifts approaching 45°, and most of the heat transfer area is in the fixed volume space.

- The converged k_1 is in strong disagreement with steady state orifice flow data. $k_1 = 2.5$ corresponds to C_d of only 0.4, a very low value. Some converged k_1's are higher, corresponding to even lower C_d's.

- The converged k_2's seem too low based on typical orifice plate - vena contracta distances and the hypotheses that went into the unsteady orifice model.

Two possible explanations for the observed problems are being investigated:

1) The models that went into the simulation program are correct, but they are converging to a set of results distant from the true result because of poor initial guesses. This implies that both spaces have a heat transfer phase shift in the 45° degree range, and the combination of the 0° and 90° degree phase shifts gives the same net heat transfer. The large values of k_1 and the small values of k_2 emerge to compensate for this misplaced heat transfer.

2) One or more of the models (heat transfer and orifice flow) that go into the simulation are wrong. If a single model is seriously in error, it can offset the convergence of constants in the other model as well.

Explanation 2 seems the most reasonable. The sensor data on Figure 6.10 shows a considerable heat transfer enhancement during the intake period of the varying volume space; other plots, not presented here, show similar enhancement. The heat flux sensor is somewhat protected from turbulence; one might think that the increase in heat flux would be much larger on other surfaces, particularly the piston face. If this is the case, the assumption of complex Nu constant around the cycle is invalid, and the unexpected results may be simply the optimizer's attempt to compensate for an inadequate model by the use of unrealistic coefficient values.

8. Conclusion

This work has led, to date, to the following conclusions:

Conclusions relating to gas springs:

1) Gas spring loss, pressure magnitude, pressure phase shift, and heat transfer results from previous experiments are corroborated by this work.

2) This work extends those results to higher nondimensional speeds (Pe_ω) and lower volume ratios.

3) Lee's (1983) model for gas spring heat transfer and loss is applicable over volume ratios ranging from 1 to 2, thus covering most Stirling machine gas springs.

Conclusions relating to in-cylinder heat transfer with inflow:

4) Inflow-produced turbulence results in increased heat transfer and heat transfer-related loss in cylinder spaces.

5) Based on the lumped two space data analysis, the increase in heat transfer can be predicted by the Pfriem-Kornhauser (Kornhauser, 1992) model with modified coefficients.

6) The inverse, parameter optimization method for calculating heat transfer in each space separately works for simulated data. For real data it does not consistently converge to the same values.

7) The results of attempts at parameter optimization, as well as surface heat flux sensor measurements, indicate that the turbulent enhancement of heat transfer may vary over the cycle. This would invalidate one of the assumptions of the Pfriem-Kornhauser model and of the parameter optimization method.

Although this report closes Grant NAG3-1285, the authors will continue operation of the experimental apparatus. Plans are underway for developing new in-cylinder heat transfer models with provisions for cyclic turbulence variations as well as for modifications to the parameter optimization technique to measure the effects of those variations.

Appendix A. Tabulated Experimental Data

Full sets of pressure-volume-time data are available on magnetic media from through NASA Lewis Research Center or directly from the authors.

ONE SPACE RESULTS

Pew	Omega rad/sec	P_{mean} psia	p*	Plead degrees	LOSSnd
115.4352	2.76	13.74	0.804171	4.405014	0.403974
270.4128	6.47	13.78	0.896638	3.1292	0.268691
530.1744	12.66	13.8	0.9042	2.2508	0.196987
1292.666	30.84	13.87	0.9547	1.5605	0.140575
2754.773	65.56	13.89	0.9497	1.144	0.100658
289.1295	2.8	34.06	0.8842	2.9683	0.263256
693.0841	6.47	35.37	0.9139	2.01791	0.176615
1321.998	12.49	34.95	0.9522	1.5443	0.126581
3408.689	30.45	37.05	0.9565	0.9441	0.082671
7013.426	62.92	37.04	0.9431	0.7693	0.071359
682.4129	3.29	68.53	0.935	2.0153	0.175314
1383.171	6.51	70.16	0.9464	1.4929	0.126498
2674.535	12.64	69.88	0.9609	1.1104	0.092289
7003.225	31.09	74.82	0.9764	0.6535	0.056134
13452	59.64	74.72	0.9654	0.5229	0.04512
1348.905	3.03	146.9	0.9505	1.4825	0.132042
2891.931	6.51	146.67	0.968	1.0707	0.090557
5559.96	12.5	146.82	0.9777	0.8232	0.069329
13624.22	29.91	149.49	0.9812	0.504	0.042491
29188.94	64.05	149.51	0.9618	0.3446	0.031576
2337.214	3.25	237.99	0.9498	1.1713	0.1074
4677.339	6.49	237.68	0.9635	0.8703	0.074842
8950.395	12.45	237.21	0.9765	0.641	0.054204
46098.41	62.63	242.33	0.9508	0.2873	0.024353

Pew	Nu(r)	Nu(i)	Numag	Phase degrees
115.4352	18.87046	15.16644	24.20982	38.7893
270.4128	27.2868	23.16374	35.79285	40.3279
530.1744	38.63025	36.02166	52.81909	42.99871
1292.666	62.28192	59.85096	86.37809	43.85972
2754.773	96.65846	141.6125	171.4554	55.68428
289.1295	27.48314	22.64612	35.61137	39.48854
693.0841	43.12139	40.60786	59.23219	43.28051
1321.998	55.9877	46.89394	73.03194	39.94872
3408.689	94.32844	128.6615	159.5357	53.75292
7013.426	171.2764	292.7975	339.2138	59.67384
682.4129	39.13013	26.09679	47.03413	33.70024
1383.171	58.16803	46.89104	74.71472	38.87336
2674.535	81.12073	66.35855	104.8047	39.28392
7003.225	126.77	119.9314	174.5112	43.41216
13452	197.1048	251.1979	319.2972	51.88016
1348.905	55.58764	39.35189	68.10695	35.29564
2891.931	83.36453	55.84651	100.3418	33.81842
5559.96	123.3796	78.20086	146.075	32.36747
13624.22	184.4441	154.4462	240.5686	39.94148
29188.94	299.8415	542.2306	619.6119	61.05838
2337.214	75.5376	66.64056	100.7318	41.41929
4677.339	110.5402	98.6431	148.154	41.74486
8950.395	156.244	156.1047	220.8639	44.97445
46098.41	370.1814	1169.346	1226.542	72.43371

LUMPED TWO SPACE RESULTS (FIRST SET)

PEw	Pmean psia	Omega rad/sec	Δ P max psia	P* FIX	P* VAR
90.41309	13.84685	3.330919	0.020752	0.7632	0.7663
174.064	13.85748	6.432955	0.027093	0.8296	0.8349
336.8172	13.86635	12.44956	0.029314	0.8876	0.8923
814.7897	13.94613	30.01327	0.089838	0.9238	0.9323
1736.188	13.98256	63.9809	0.386856	0.9261	0.9502
214.9534	33.60924	3.284847	0.035052	0.8063	0.8121
409.3796	33.60522	6.276324	0.033907	0.8563	0.8608
803.0883	33.60025	12.28919	0.047496	0.8959	0.9006
1937.869	33.67795	29.75324	0.212661	0.9148	0.9221
4228.909	33.78011	64.93181	0.986931	0.9186	0.9301
473.4475	73.64415	3.300437	0.047832	0.861	0.8648
919.1058	73.70319	6.403563	0.049639	0.8923	0.8962
1789.183	73.74493	12.48541	0.113585	0.9143	0.9191
4416.643	76.92129	29.89387	0.488417	0.939	0.94
9307.856	76.9613	62.54888	2.081486	0.9405	0.9511
876.1673	147.5092	3.068118	0.105914	0.8826	0.8879
1812.121	147.5302	6.355197	0.122374	0.905	0.9103
3544.999	147.2578	12.43517	0.24353	0.9287	0.9325
1349.491	244.8127	2.859611	0.187533	0.8743	0.8802
2968.304	245.0366	6.278666	0.203104	0.8966	0.9021
5890.824	244.8971	12.47497	0.339038	0.914	0.9178

PEw	Plead FIX degrees	Plead VAR degrees	LOSSnd	loss corr for del P
90.41309	5.5923	5.641206	0.529967	0.527776
174.064	4.757	4.83942	0.443343	0.435673
336.8172	3.598003	3.763523	0.335738	0.323197
814.7897	3.1609	3.971645	0.348969	0.288805
1736.188	2.353958	6.46085	0.574925	0.253821
214.9534	4.428291	4.457382	0.411334	0.408897
409.3796	3.72818	3.767334	0.339209	0.336166
803.0883	3.076	3.2293	0.283944	0.272172
1937.869	2.399914	3.298023	0.289697	0.219077
4228.909	1.728722	6.063232	0.538367	0.200312
473.4475	3.538348	3.559945	0.329081	0.32692
919.1058	2.944633	3.002689	0.267538	0.262377
1789.183	2.469852	2.632847	0.229863	0.216367
4416.643	1.880207	2.787155	0.243914	0.172611
9307.856	1.176414	5.210182	0.460682	0.145651
876.1673	2.977509	2.995884	0.288805	0.286625
1812.121	2.459221	2.515167	0.225638	0.220528
3544.999	2.001111	2.161141	0.188046	0.175056
1349.491	2.541058	2.561142	0.265787	0.263183
2968.304	2.111343	2.160675	0.198395	0.193564
5890.824	1.692032	1.831921	0.16015	0.149046

PEw	NUr	NUi	NUmag	Phase	Rein/Pew degrees
90.41309	13.33072	13.90403	19.26214	46.20594	55.92592
174.064	20.27937	19.76133	28.31542	44.25876	56.14554
336.8172	26.53971	29.91406	39.99009	48.42061	56.189
814.7897	60.76107	48.17506	77.54189	38.40951	56.31848
1736.188	105.8116	98.79302	144.7624	43.03535	56.48976
214.9534	32.11929	25.10022	40.76358	38.00651	56.30655
409.3796	45.90628	37.82949	59.48493	39.49054	56.48268
803.0883	69.23869	57.03765	89.70669	39.48111	56.3679
1937.869	138.1608	113.0078	178.4914	39.28124	56.68719
4228.909	284.8287	275.0907	395.9827	44.00362	56.86167
473.4475	52.64988	38.17188	65.03155	35.94262	56.28171
919.1058	82.4519	59.50358	101.6808	35.81709	56.29527
1789.183	130.8733	94.07994	161.1796	35.71095	56.41695
4416.643	253.7387	174.0408	307.6906	34.44645	57.07762
9307.856	455.029	434.3748	629.073	43.66969	56.69852
876.1673	80.24416	54.16308	96.81304	34.0185	56.6283
1812.121	135.174	92.08484	163.5592	34.26394	56.72208
3544.999	211.0397	147.0073	257.1943	34.86053	56.62958
1349.491	106.0713	88.55264	138.1763	39.8565	56.87224
2968.304	192.2864	171.6198	257.7352	41.74961	56.82237
5890.824	301.0086	296.4761	422.4976	44.56536	56.85603

LUMPED TWO SPACE RESULTS (SECOND SET)

Pe$_\omega$	Pmean	ω	ΔP Max	P*	P*
	psia	rad/sec	psia	FIX	VAR
162.11	14.372	5.853	0.029	0.7198	0.7332
357.02	14.918	12.491	0.042	0.7686	0.7857
939.72	15.062	32.578	0.112	0.8717	0.8934
1857.03	15.728	62.407	0.405	0.8737	0.9038
370.20	28.899	6.645	0.054	0.8197	0.8335
709.49	29.650	12.503	0.061	0.8483	0.8622
1790.88	29.092	32.387	0.235	0.9173	0.9340
3494.28	30.014	62.061	0.789	0.9182	0.9420
955.81	74.106	6.739	0.120	0.9110	0.9244
1854.19	76.127	12.883	0.148	0.9169	0.9303
4544.60	75.549	31.557	0.566	0.9367	0.9511
8809.40	73.959	62.995	1.963	0.9287	0.9520
1348.21	103.732	6.778	0.183	0.9218	0.9355
2484.72	103.680	12.628	0.200	0.9233	0.9370
6483.00	108.771	31.586	0.797	0.9448	0.9600
12366.17	98.440	67.269	2.991	0.9329	0.9544

Pe_{ω}	Plead FIX degrees	Plead VAR degrees	LOSSnd	LOSSND w/approx PD loss
162.11	4.824	4.837	0.4530	0.4492
357.02	3.894	4.049	0.3721	0.3561
939.72	2.943	4.077	0.3625	0.2704
1857.03	2.300	6.291	0.5594	0.2393
370.20	3.876	3.959	0.3529	0.3442
709.49	3.147	3.334	0.2967	0.2786
1790.88	2.421	3.559	0.3113	0.2195
3494.28	1.597	5.629	0.5007	0.1800
955.81	2.938	3.008	0.2606	0.2510
1854.19	2.387	2.575	0.2228	0.2055
4544.60	1.803	2.829	0.2480	0.1650
8809.40	1.196	5.293	0.4677	0.1442
1348.21	2.629	2.687	0.2360	0.2292
2484.72	2.170	2.346	0.2030	0.1877
6483.00	1.576	2.635	0.2323	0.1466
12366.17	0.974	5.659	0.5006	0.1307

Pe_ω	NUr	NUi	NUmag	Phase degrees
162.11	33.746	29.553	44.857	41.210
357.02	53.095	50.834	73.506	43.754
939.72	90.270	74.062	116.764	39.367
1857.03	157.696	130.686	204.810	39.649
370.20	49.678	36.985	61.934	36.667
709.49	70.651	58.871	91.964	39.803
1790.88	134.538	80.838	156.956	31.000
3494.28	202.048	156.928	255.832	37.836
955.81	86.143	36.022	93.372	22.693
1854.19	121.765	65.591	138.307	28.310
4544.60	240.953	169.231	294.445	35.082
8809.40	376.001	374.822	530.912	44.910
1348.21	109.298	69.753	129.660	32.546
2484.72	148.360	103.230	180.740	34.831

A-8

Appendix B. Nomenclature

A	Area
C	Clearance
C_d	Orifice discharge coefficient
D_h	Cycle mean hydraulic diameter (4 × volume ÷ surface)
h	Heat transfer coefficient
i	$(-1)^{1/2}$
k	Thermal conductivity
k_1, k_2	Orifice discharge coefficients
Loss_{nd}	Non-dimensional lost work (eq. (4))
m	Mass
Nu_c	Complex Nusselt number (eq. (1))
P	Pressure
Pe_ω	Oscillation Pe clet number $= \omega D_h^2/4\alpha_0$
Pr	Prandtl number
Q	Heat transfer
$\dot{q}''$	Heat flux rate
R	Gas constant
r_v	Volume Ratio = maximum volume / minimum volume
Re_{in}	Inlet Reynolds Number $= \bar{v}D_h/\nu_0$
S_{gen}	Entropy generation
T	Temperature
t	Time
U	Internal energy
V	Volume
$\bar{v}$	Velocity
W	Work
α	Thermal diffusivity
γ	Gas specific heat ratio
δ	Laminar boundary sublayer thickness
Φ	Phase angle
ν	Kinematic viscosity
ω	Angular frequency

Subscripts

a	Amplitude
f	Fixed volume space
i	Imaginary part
mm	Mixed mean
r	Real part
t	Transported between spaces
v	Varying volume space
w	Wall
0	Reference conditions (cycle mean conditions)

Appendix C. References

Annand, W.J.D., 1963, "Heat Transfer in the Cylinders of Reciprocating Interal Combustion Engines," Proceedings of the Institution of Mechanical Engineers, Vol 177, No 36. pp 973-996.

Annand, W.J.D. and Pinfold, D., 1980, "Heat Transfer in the Cylinder of a Motored Reciprocating Engine," SAE Paper 800457, Society of Automotive Engineers.

Borman, G. and Nishiwaki, K., 1987, "Internal Combustion Engine Heat Transfer," *Progress in Energy and Combustion Science*, Vol 12, pp 1-46.

Breckenridge, R.W. Jr., Heuchling, T.P., and Moore, R.W. Jr., 1971, Rotary-Reciprocating Cryogenic Refrigeration Studies, Part I, Analysis, AFFDL-TR-71-115, Part I, Air Force Flight Dynamics Laboratory, pp 43-55 and 91-99.

Carslaw, H.S. and Jaeger, J.C., 1959, *Conduction of Heat in Solids*, Oxford University Press, New York, pp 64-70.

Chafe, J.N., 1988, "A Study of Gas Spring Heat Transfer in Reciprocating Cryogenic Machinery," Ph.D. Thesis, Massachusetts Institute of Technology, Cambridge, MA.

Chong, M.S., 1971, "Heat Transfer in a Motored Engine," M.Eng.Sci. Thesis, University of Melbourne, Australia.

Dennis, J.E. Jr., 1977, "Nonlinear Least Squares," *State of the Art in Numerical Analysis*, K. Jacobs ed., Academic Press, pp 269-312.

Gedeon, D., 1989, Memo to R. Tew, NASA Lewis Research Center.

Geng, S., 1991, Private Communication.

Hamming, R.W., 1971, *Digital Filters*, 2nd ed., Prentice-Hall, Englewood Cliffs, NJ, pp 92-100.

Keck, J.C., 1981, "Thermal Boundary Layer in a Gas Subject to a Time Dependent Pressure," *Letters in Heat and Mass Transfer*, Vol 8, pp 313-319.

Kornhauser, A.A., 1989, "Gas-Wall Heat Transfer During Compression and Expansion," Sc.D. Thesis, Massachusetts Institute of Technology, Cambridge, MA.

Kornhauser, A.A., 1992, "A Model of In-Cylinder Heat Transfer with Inflow-Produced Turbulence," *Proceedings of the 27th Intersociety Energy Conversion Engineering Conference*, Vol 5, pp 523-528.

Kornhauser, A.A. and Smith, J.L. Jr., 1988, "Application of a Complex Nusselt Number to Heat Transfer During Compression and Expansion," *On Flows in Internal Combustion Engines -*

IV, American Society of Mechanical Engineers, pp 1-8.

Kornhauser, A.A. and Smith, J.L. Jr., 1993, "The Effects of Heat Transfer on Gas Spring Performance," *Journal of Energy Resources Technolgy*, Vol 115, pp 70-75.

Lee, K.P. and Smith, J.L. Jr., 1978, "Influence of Cyclic Wall-to-Gas Heat Transfer in the Cylinder of the Valved Hot-Gas Engine," *Proceedings of the 13th Intersociety Energy Conversion Engineering Conference*, Paper No 789195.

Lee, K.P., 1983, "A Simplistic Model of Cyclic Heat Transfer Phenomena in Closed Spaces," *Proceedings of the 18th Intersociety Energy Conversion Engineering Conference*, pp 720-723.

Martini, W.R., 1983, *Stirling Engine Design Manual*, NASA CR-168088, National Aeronautics and Space Administration.

Overbye, V.D., Bennethum, J.E., Uyehara, O.A., and Myers, P.S., 1961, "Unsteady Heat Transfer in Engines, *Society of Automotive Engineers Transactions*, Vol 69, pp 461-494.

Pfriem, H., 1943, "Periodic Heat Transfer at Small Pressure Fluctuations," NACA-TM-1048, National Advisory Committee for Aeronautics, (Translated from *Forschung auf dem Gebiete des Ingenierwesens*, Vol 11, 1940, pp 67-75).

Simon, T.W. and Seume, J.R., 1986, *A Survey of Oscillating Flow in Stirling Engine Heat Exchangers*, NASA CR-182108, National Aeronautics and Space Administration.

Skinner, G.T., 1961, "Calibration of Thin Film Gage Backing Materials," *ARS Journal*, Vol 31, pp 671-762.

Sullivan, T.J., 1989, *NASA Lewis Stirling Engine Computer Code Evaluation*, NASA CR-182248, National Aeronautics and Space Administration.

Wendland, D.W., 1968, *The Effect of Periodic Pressure and Temperature Fluctuations on Unsteady Heat Transfer in a Closed System*, NASA CR-72323, National Aeronautics and Space Administration.

Woschni, G., 1967, "A Universally Applicable Equation for the Instantaneous Heat Transfer Coefficient in the Internal Combustion Engine," SAE Paper No 670931, Society of Automotive Engineers.